eman ta zabal zazu

Universidad del País Vasco
Euskal Herriko Unibertsitatea

Ingeniaritza Goi Eskola Teknikoa
Escuela Técnica Superior de Ingeniería
Bilbao

Development of Poly(ε-caprolactone) Based Biodegradable Polymeric Blends with Biologically Active Compounds for Making Drug Eluting Medical Devices

Eva Sánchez Rexach

Supervisors

Jose Ramon Sarasua

Emilio Meaurio Arrate

2018

(c)2018 EVA GLORIA SANCHEZ REXACH

The Thesis has been performed at:

ZIBIO Group, Department of Mining-Metallurgy Engineering and Materials Science
School of Engineering
Bilbao
Spain

Institute of Biophysik
Universität für Bodenkultur Wien
Vienna
Austria

and

Institute of Chemistry
The Hebrew University of Jerusalem
Jerusalem
Israel

“Dabilen harriari ez zaio goroldiorik lotzen”

Acknowledgments/Agradecimientos

La realización de esta tesis no hubiera sido posible sin el apoyo de la gente que me ha hecho llegar a este momento de mi vida. Me gustaría dedicar estas líneas a esas personas que me han ayudado durante el camino.

En primer lugar, quería agradecer a mis directores Jose Ramon Sarasua y Emilio Meaurio, primeramente, por brindarme la oportunidad de dar este giro a mi carrera profesional para dedicarme a la investigación en el campo de la ciencia e ingeniería de biomateriales poliméricos, y segundo, por haberme guiado y ayudado siempre que lo he necesitado. Además, agradezco al MINECO por la beca de investigación que me fue concedida, ya que, sin ella, no hubiera sido posible la realización de este trabajo.

También quería dar las gracias a mis compañeros del día a día, así como a los que me lo han hecho más fácil cuando me ha tocado irme fuera. A Ester, Ainoa, Inger, Jone, Amaia, Naroa, Hegoi, Jorge y Aitor. Al Prof. Jose Toca por haberme acogido con los brazos abiertos en la BOKU de Viena. Mi estancia en esta memorable ciudad no hubiera sido tan enriquecedora, sin la ayuda de Jagoba, Itziar, Alberto, Batirtze, y de mi vecina Eva, quienes me enseñaron todos los rincones y la forma de vida de los vienenses. A la Prof. Meital Reches y a todo su grupo de investigación (Tal Zada, Sivan Nir, Sivan Yuran y Tal Duanias), por enseñarme todo lo que sé de bacterias y hacerme sentir una más en el laboratorio de Jerusalén.

No puedo dejar de mencionar a todas mis “neskis” que me han acompañado durante este trayecto. En especial a Ane, Linnet, Carlos y Lourdes que vinieron a insuflarme energía durante mis estancias, tanto en Viena como en Jerusalén. A Igone y Nerea que siempre han estado allí. Me siento muy orgullosa de todas ellas y afortunada de tenerlas.

Para terminar, doy las gracias a mis padres, Gloria y Juan, que desde pequeña me inculcaron que con trabajo y esfuerzo todo es posible, y a mis hermanos, Jon, Daniel y Asier, que siempre han estado a mi lado interesándose por mis progresos y apoyándome en los malos momentos. Y a Joar, que ha vivido todo el doctorado a mi lado desde que dejé el mundo de la aeronáutica hasta hoy, y es la persona que me escucha cuando llego a casa, me cuida, y sobre todas las cosas, me quiere.

Table of Contents

Acknowledgments/Agradecimientos 1

Summary 13

Introduction 27

1. Drug Eluting Devices 29

2. Orthopedic Drug Eluting Devices 32

3. Drug eluting Stents for Breathing System 37

4. Drug Eluting Gastrointestinal Stents 39

5. Antimicrobial Urinary Stents 40

6. Cardiovascular Disease Treatment 42

7. Neuronal Implants 46

8. Wound Dressing 49

9. Future of Drug Eluting Devices 51

10. Conclusions 52

References 55

Objective and Methodology 65

Chapter 1. Antimicrobial Poly(ε-caprolactone)/Thymol Blends: Phase Behavior, Interactions and Drug Release Kinetics 69

Summary 71

1.1. Introduction 71

1.2. Experimental Section 74

1.2.1. Starting Materials 74
1.2.2. Blend Preparation 74
1.2.3. Differential Scanning Calorimetry 74
1.2.4. Melting Point Depression 75
1.2.5. Fourier Transform Infrared Spectroscopy 75
1.2.6. In Vitro Drug Release Kinetics 76
1.3. Results and Discussion 77
1.3.1. DSC Analysis 77
1.3.2. Melting Point Depression Analysis. 79
1.3.3. FTIR Analysis 88
1.3.4. In Vitro Drug Release 93
1.4. Conclusions 95
References 97
Chapter 2. Physicochemical Characterization and Drug Release Kinetics in Poly(ε-caprolactone)/Chloramphenicol Blends 103
Chapter 2.1. The Conformation of Chloramphenicol in the Ordered and Disordered Phases 105
Summary 107
2.1.1. Introduction 107
2.1.2. Experimental Section 110
2.1.2.1. Starting Materials 110
2.1.2.2. Differential Scanning Calorimetry 110
2.1.2.3. Fourier Transform Infrared Spectroscopy 111

2.1.2.4. Conformational Analysis 111

2.1.3. Results and Discussion 112

2.1.3.1. DSC Analysis 112

2.1.3.2. FTIR Analysis of Crystalline CAM 112

2.1.3.3. FTIR Analysis of Molten CAM and Free CAM in Solution 117

2.1.3.4. Ab Initio Quantum Mechanical Calculations 120

2.1.4. Conclusions 129

References 131

Chapter 2.2. Miscibility, Interactions and Antimicrobial Activity of Poly(ε-caprolactone)/Chloramphenicol Blends 139

Summary 141

2.2.1. Introduction 141

2.2.2. Experimental Section 144

2.2.2.1. Starting Materials 144

2.2.2.2 Blend Preparation 144

2.2.2.3. Differential Scanning Calorimetry 144

2.2.2.4. Melting Point Depression 144

2.2.2.5. Fourier Transform Infrared Spectroscopy 145

2.2.2.6. X-ray Diffraction 145

2.2.2.7. Atomic Force Spectroscopy 145

2.2.2.8. In Vitro Release Studies and Release Kinetics 146

2.2.2.9. Agar Diffusion Test (*E. coli*) 146

2.2.3. Results and Discussion 147

2.2.3.1. PCL/CAM Blend Characterization 147
2.2.3.2. Drug Release Behavior 159
2.2.3.3. Bacterial inhibition assay 161
2.2.4. Conclusions 163
References 165

Chapter 3. Miscibility, Interactions and Drug Release Kinetics Investigation in Poly(ε-caprolactone)/Quercetin Blends 169

Summary 171
3.1. Introduction 172
3.2. Experimental Section 175
3.2.1. Starting Materials 175
3.2.2. Blend Preparation 175
3.2.3. Field Emission Scanning Electron Microscopy 177
3.2.5. Differential Scanning Calorimetry 178
3.2.6. Attenuated Total Reflection Fourier Transform Infrared Spectroscopy 178
3.2.7. Atomic Force Spectroscopy 178
3.2.8. In Vitro Release Studies and Release Kinetics 178
3.3. Results and discussion 180
3.3.1. DSC Analysis 180
3.3.3. ATR-FTIR Analysis 183
3.3.4. AFM Analysis 185
3.3.5. Drug Release Behavior 186
3.4. Conclusions 192

References 195

Chapter 4. Antifouling Poly(ε-caprolactone) Surfaces for Medical Devices 201

Summary 203

4.1. Introduction 203

4.2. Results and discussion 205

4.2.1. Coating of PCL films with antifouling peptide 205

4.2.2. Surface characterization 206

4.2.3 Biofilm Formation on PCL Surfaces Coated with Antifouling Peptide 210

4.3. Conclusions 211

References 213

General Conclusions 215

Appendix 219

A1. List of Figures 221

A2. List of Tables 226

A3. Symbols and Abbreviations 229

A4. List of Publications and Congresses 233

A5. Curriculum Vitae 235

Summary

Summary

According to the World Health Organization (WHO), infections acquired in a hospital are among the major causes of death. Invasive devices such as catheters or implants are associated to these infections. Furthermore, the primary cause of implant-associated infections is the formation of a well-defined bacterial network on the surface of medical devices, termed biofilm, which is extremely resistant to antibiotics. In this work, two different strategies to avoid infections related to medical devices have been adopted by combining biomaterials with biologically active molecules: the creation of amorphous solid dispersions (ASDs) formed by miscible polymer-drug blends for making drug eluting devices, and an antifouling coating which will limit the biofilm formation on surfaces.

In medicine, biodegradable polymers offer great potential for controlled drug delivery and wound management (e.g., adhesives, sutures, and surgical meshes), for orthopedic devices (screws, pins, and rods), as well as for dental applications (filler after a tooth extraction) and tissue engineering, just to name the most important. The use of biopolymers is a major advance, since, in addition to being materials prepared to act with biological systems, they have a great versatility in terms of mechanical properties and biodegradation. The combination of these materials with biologically active molecules enables the production of biomedical devices with the ability of preventing infections, which can be absorbed by the body after they have served their purpose. The material selected for making biomedical devices in this work is the biodegradable poly(ε-caprolactone) (PCL). PCL is a semicrystalline polymer widely used in the production of biomedical devices, whose degradation can last from several months to years, making it suitable for long-term biomedical applications such as implants.

In the last few years, medical devices have evolved from being a mere support to being intelligent devices that help with the healing process. Biomedical engineering is now focusing on the production of bioactive implants that assist patient recovery. In the case of biodegradable drug eluting devices, the challenge is to design the drug release profile, the mechanical properties and the rate of degradation, adapted for each problem. Where, when and how much drug is necessary in each case must be clarified for an effective

design. Polymeric materials offer a broad range of possibilities and contribute to substantially improving the effectiveness of the bioactive molecules, directing them towards the objective, as well as reducing the side effects of an overdose. The combination of biodegradable polymers with biologically active molecules is clearly interesting both clinically and commercially.

In Chapter 1 of this thesis (*Chapter 1. Antimicrobial Poly(ε-caprolactone)/Thymol Blends: Phase Behavior, Interactions and Drug Release Kinetics*) blends of PCL and Thymol, which is an effective antimicrobial, have been prepared by melt-mixing. When two polymeric materials are miscible, macroscopic properties of single-phase materials are expected for the blend, such as a single glass transition temperature intermediate between those of the pure components. In this system, the analysis of the glass transition (T_g) did not provide clarifying data and, thus, the melting point (T_m) depression study was conducted for both PCL-rich and Thymol-rich blends, adapting the Flory-Huggins theory in each case, whereby miscibility in the blend was found. Moreover, the specific interactions were analyzed by infrared spectroscopy, and strong hydrogen bonding interactions were confirmed between the carbonyl groups of the polymer and the hydroxyl group of the Thymol (-C=O···O-H-).

Finally, the analysis of the release kinetics of Thymol was performed. It was concluded that the drug is released by diffusion through the swelled polymeric chains, and that it does slowly due to the strong molecular interactions established between the two species. Hence, the PCL-Thymol system is suitable for building long-lasting antimicrobial devices.

In Chapter 2 (*Chapter 2. Physicochemical Characterization and Drug Release Kinetics in Poly(ε-caprolactone)/Chloramphenicol Blends*) mixtures of PCL with the broad-spectrum antibiotic Chloramphenicol (CAM) were studied. Since it is a drug sparingly water-soluble, it can remain undissolved in the gastrointestinal tract when administered orally, thus, the body does not absorb it but it is excreted. Hence, the combination of this antibiotic with the PCL would allow to keep it in an amorphous form, obtaining a greater solubility and bioavailability. In order to determine the miscibility in this system, PCL/CAM blends prepared by casting were analyzed by differential scanning calorimetry (analysis of T_g, T_m, as well as interaction parameter χ). Then, specific interactions between the polymer and the antibiotic were studied using infrared spectroscopy, and through the analysis of the spherulitic morphology of the blends by means of atomic force microscopy (AFM), it was found that the mobility of the polymer chains during the crystallization process is reduced due to the -C=O···H-O- interactions in miscible blends. Therefore, the hexagonal structure characteristic of the spherulites of the PCL shows a less compact morphology due to the presence of the drug.

In addition, the conformation of Chloramphenicol was exhaustively studied in the order and disordered phases by means of FTIR spectroscopy and molecular modelization methods.

After the physicochemical characterization, the study of the release behavior showed that when the entire antibiotic is in an amorphous state, about half of the drug is released in the first 10 minutes, followed by a constant release rate. This mechanism responds to an ideal drug delivery from biomedical devices, since the initial burst serves to deal with the risk of infection during implantation and the subsequent constant release at an effective therapeutic concentration, to counteract a possible latent infection. In addition, the antibacterial activity of the polymer-drug system was analyzed by agar diffusion test against *Escherichia Coli* (bacteria frequent in implant-associated infections), and the results confirmed that Chloramphenicol can be released in a controlled way without losing antibacterial activity.

In Chapter 3 (*Chapter 3. Miscibility, Interactions and Drug Release Kinetics Investigation in Poly(ε-caprolactone)/Quercetin Blends*), PCL was blended with a flavonoid which has antioxidant and anti-inflammatory properties. Despite the beneficial properties of Quercetin, the main downside of this molecule is a high crystallinity that results in low bioavailability, as well as the easy oxidation in aqueous environments such as body fluids. In fact, prior performing the release experiments, the oxygen was removed from the medium using a nitrogen recirculation system. Quercetin was blended with PCL, to tackle its high crystallinity through the specific interactions created with the functional groups of the polymeric chains. Once again, the miscibility was studied using the single intermediate glass transition criterion (considering the T_g of the Quercetin two-thirds of its melting temperature), and hydrogen bonds were confirmed by means of infrared spectroscopy.

The novelty of this chapter resides in the comparative study of the release behavior of the Quercetin from different supports: micrometric films obtained via casting, nanometric films obtained by spin coating, and scaffolds composed of micro and nanofibers manufactured by the electrospinning technique. The release of Quercetin from nanometric films was tested using a quartz crystal microbalance (QCM) that calculates the mass variation by measuring the change in frequency of a quartz crystal resonator when disturbed by the loss of a small mass. It was examined the dependence on the composition, and in turn on the crystallinity, in the release process. Moreover, it was assessed the influence of the pore size in mats obtained by electrospinning: the larger the pores, the greater the release. Over again, it is confirmed that when the drug is in an amorphous form, there is an initial burst good for responding to the high risk of infection during an intervention, followed by a sustained release within the desired therapeutic margin, to prevent infections in the implant during the healing phase.

Biofouling is an undesirable process that results in the accumulation of organisms and their by-products on surfaces. In the case of bacteria, this process leads to the formation of biofilm, which provides bacteria with superior survival properties upon exposure to antibiotics. The formation of biofilm in biomedical devices can generate serious infections, especially frequent during the hospital stay. Since within the biofilm bacteria are 1,000 times more resistant to antibiotics, it is often necessary to replace the implant. Antifouling materials alter the properties of surfaces in order to prevent the accumulation of microorganisms on the substrates.

It is in Chapter 4 of the present thesis (*Chapter 4. Antifouling Poly(ε-caprolactone) Surfaces for Medical Devices*) where films of PCL are superficially modified with an antifouling peptide that prevents the formation of biofilm. The coating is based on a biocompatible tripeptide, which designs allows its spontaneous adsorption onto any kind of substrate due to a DOPA linker (the main constituent of the glue proteins of mussels), as well as the creation of non-sticky surfaces thanks to two fluorinated groups. Hence, surfaces coated with this synthetic peptide would be able to interfere with the biofouling process.

Surfaces of PCL (control) and of PCL modified with the peptide were incubated in inoculums of *E. coli*, and subsequently, the number of colonies adhered in each kind of substrate was compared to verify the antifouling activity.

Taking everything into consideration, this PhD thesis explores different combinations to combat infections in medical devices.

Resumen

Casi la mitad de las infecciones nosocomiales (aquellas contraídas durante la hospitalización) están asociadas a la utilización de dispositivos biomédicos. Son infecciones difíciles de tratar y muchas de ellas, implican la extracción del dispositivo. Un factor esencial es la formación de biofilm alrededor del implante, ya que constituye una fuerte barrera bacteriana frente a los antibióticos. Para prevenir las infecciones en este tipo de dispositivos, en este trabajo se han usado dos estrategias: la formación de dispersiones sólidas amorfas (ASDs) constituidas por mezclas polímero-fármaco miscibles y con fuertes interacciones intermoleculares, para una liberación controlada del fármaco, y la biofuncionalización superficial del implante con un péptido antifouling que evite la adhesión de las bacterias que forman el biofilm.

Los materiales poliméricos han ido desplazando paulatinamente a materiales tan tradicionales como los metales o los cerámicos en el campo de la medicina. El uso de biopolímeros supone un gran avance, ya que, además de ser materiales preparados para actuar con sistemas biológicos, poseen una gran versatilidad en cuanto a propiedades mecánicas y de biodegradación. Combinando estos materiales con moléculas biológicamente activas, se pueden fabricar dispositivos biomédicos capaces de prevenir infecciones, con la ventaja de que pueden degradarse dentro del cuerpo después de cumplir con su cometido, lo que supone una mejora en la calidad de vida de los pacientes. El material que se ha elegido como candidato para la fabricación de dispositivos biomédicos en este trabajo, ha sido el polímero biodegradable poli(ε-caprolactona) (PCL). La PCL es un polímero semicristalino ampliamente usado en la producción de dispositivos biomédicos, cuya degradación puede durar desde varios meses hasta años, haciéndolo adecuado para aplicaciones biomédicas a largo plazo como implantes.

En los últimos años, los dispositivos médicos han pasado de ser un mero soporte, a ser aparatos inteligentes que ayudan con el proceso de curación. La ingeniería biomédica se está enfocando en la fabricación de implantes bioactivos, es decir, con una funcionalidad adicional que ayude a la recuperación del paciente. En el caso de los dispositivos liberadores de fármacos biodegradables, el reto está en diseñar el perfil de liberación del fármaco, las propiedades mecánicas y la velocidad de degradación del dispositivo, para

cada problemática. Hay que saber dónde, cuándo y cuánto fármaco es necesario en cada caso. En este contexto, los materiales poliméricos ofrecen todo un mundo de posibilidades y permiten mejorar sustancialmente la eficacia de los medicamentos, dirigiéndolos hacia el objetivo y reduciendo los efectos secundarios que acarrea una dosis excesiva. La combinación de los polímeros biodegradables con moléculas biológicamente activas, tiene un gran potencial en cuanto a mejorar la efectividad de nuevos fármacos, y ese valor añadido que se le aporta a los dispositivos biomédicos es claramente interesante tanto clínica como comercialmente.

En el Capítulo 1 de esta tesis (*Chapter 1. Antimicrobial Poly(ε-caprolactone)/Thymol Blends: Phase Behavior, Interactions and Drug Release Kinetics*) se han mezclado en fundido la PCL y el Timol, que es un efectivo antimicrobiano. En términos de termodinámica clásica, la miscibilidad se define como el nivel de mezcla molecular que da propiedades esperadas para materiales de una fase, como una temperatura de transición vítrea única e intermedia a las de las sustancias puras de la mezcla. En este caso, el análisis de la transición vítrea (T_g) no aportó datos esclarecedores y, por tanto, se recurrió al estudio de la depresión del punto de fusión (T_m), tanto para mezclas ricas en PCL como ricas en Timol, adaptando la teoría de Flory-Huggins en cada caso, de donde se pudo inferir miscibilidad en la mezcla. Asimismo, se analizaron las interacciones específicas mediante espectroscopia infrarroja, hallándose fuertes interacciones de puentes de hidrogeno entre los grupos carbonilo del polímero y el hidroxilo del Timol (-C=O···O-H-).

Una vez comprobada la miscibilidad en el sistema, se estudió la cinética de liberación y se concluyó que el Timol se libera por difusión a través de las cadenas polimérica, y que lo hace con lentitud debido a las fuertes interacciones moleculares establecidas entre las dos especies. De ahí que el sistema PCL-Timol sea un sistema válido para construir dispositivos antimicrobianos de larga duración.

En el Capítulo 2 (*Chapter 2. Physicochemical Characterization and Drug Release Kinetics in Poly(ε-caprolactone)/Chloramphenicol Blends*) se estudiaron las mezclas de PCL con el antibiótico de amplio espectro cloranfenicol (CAM). Se trata de un fármaco poco hidrosoluble que, administrado por vía oral, puede permanecer sin disolver en el tracto gastrointestinal, de manera que no es absorbido por el organismo y termina siendo excretado. Así pues, la interacción entre este antibiótico y la PCL nos permitiría mantenerlo en estado amorfo, para una mayor solubilidad y biodisponibilidad. Con el fin establecer la miscibilidad en este sistema, las mezclas de PCL/CAM obtenidas por solvent-casting fueron analizadas por calorimetría diferencial de barrido (análisis de T_g, T_m y factor de interacción χ). Las interacciones de puentes de hidrógeno existentes entre el polímero y el antibiótico fueron estudiadas mediante espectroscopia infrarroja. Además, a través del análisis de la morfología esferulítica de las mezclas por medio de microscopía de fuerza atómica (AFM) se encontró que, en sistemas miscibles, la movilidad de las cadenas poliméricas durante el proceso de cristalización se ve reducida debido a las interacciones -C=O···H-O-, de forma que la estructura hexagonal característica de las esferulitas de la PCL se hace menos compacta. También se estudió de manera exhaustiva el comportamiento conformacional de la molécula de cloranfenicol.

Tras la caracterización fisicoquímica, el estudio de la cinética de liberación mostró que cuando todo el antibiótico se encuentra en estado amorfo, cerca de la mitad del fármaco se libera en los primeros 10 minutos, seguido de una liberación constante. Este mecanismo responde a un sistema ideal de liberación de fármacos para dispositivos biomédicos, ya que la liberación brusca inicial sirve para hacer frente al riesgo de infección durante la implantación, y la posterior liberación constante a una concentración terapéutica efectiva, para contrarrestar una posible infección latente. Asimismo, la actividad antibacteriana del sistema polímero-fármaco fue analizada mediante el método de difusión en agar inoculando la bacteria *Escherichia Coli* (bacteria causante de infecciones en implantes médicos), y los resultados confirmaron que el Cloranfenicol puede ser liberado de manera controlada sin perder su poder bactericida.

En el Capítulo 3, (*Chapter 3. Miscibility, Interactions and Drug Release Kinetics Investigation in Poly(ε-caprolactone)/Quercetin Blends Blends*), se examinaron las mezclas de PCL con un flavonoide con propiedades antioxidantes y antiinflamatorias. A pesar de las propiedades beneficiosas de la Quercetina, las desventajas de esta molécula residen en su fuerte tendencia a autoasociarse, que deriva en una baja biodisponibilidad, además de ser una sustancia que se oxida fácilmente. De hecho, para hacer los ensayos de liberación se tuvo que quitar el oxígeno del medio mediante un sistema de recirculación de nitrógeno. El objetivo consiste en intentar suprimir la cristalinidad de la Quercetina, gracias a las interacciones específicas con los grupos funcionales de las cadenas poliméricas. En este caso, se vuelve a estudiar la miscibilidad a través del criterio de una transición vítrea intermedia a los componentes puros (suponiendo como T_g de la Quercetina 2/3 de su temperatura de fusión), y se confirman los enlaces de hidrógeno por medio de espectroscopia infrarroja.

Lo novedoso de este capítulo es que se hace una comparativa de la liberación desde distintos soportes: filmes micrométricos obtenidos vía casting, filmes nanométricos obtenidos por spin coating, y scaffolds compuestos por micro y nanofibras fabricados por la técnica de electrohilado. La liberación de Quercetina desde los filmes nanómetricos se ensayó usando una microbalanza de cristal de cuarzo (QCM) que mide la masa mediante los cambios de frecuencia de un cristal de cuarzo piezoeléctrico al ser perturbado por la pérdida de una pequeña cantidad de masa. A través de este estudio, se observó la dependencia de la composición, y a su vez de la cristalinidad, en el proceso de liberación, además de la influencia que tiene el tamaño de poro en los filmes obtenidos por electrohilado: a mayores poros, mayor liberación. Una vez más queda demostrado que cuando el fármaco está en estado amorfo, se da una liberación brusca inicial capaz de responder al elevado riesgo de infección durante la intervención, seguida de una liberación sostenida dentro del intervalo terapéutico deseado, para prevenir las infecciones microbianas en el implante durante la fase de curación.

El biofouling se define como la acumulación de microorganismos indeseables, como bacterias, hongos, diatomeas, algas, plantas o animales, que se adhieren a las superficies. En el caso de bacterias, este proceso deriva en la formación de una red bacteriana llamada biofilm resistente a los antibióticos. La formación de biofilm en dispositivos biomédicos puede generar graves infecciones, especialmente frecuentes durante la estancia hospitalaria. Dado que las bacterias del biofilm pueden ser hasta 1.000 veces más resistentes a los antibióticos, la mayoría de las veces se hace necesario sustituir el implante. Los materiales antifouling alteran las propiedades de las superficies, para prevenir la acumulación de microorganismos sobre los substratos. Es en el Capítulo 4 de la presente tesis (*Chapter 4. Antifouling Poly(ε-caprolactone) Surfaces for Medical Devices*) cuando se lleva a cabo el recubrimiento de superficies de PCL con un péptido antifouling que evita la formación de biofilm. Se trata de un tripéptido biocompatible con carácter antifouling, el cual, cuenta en su estructura con un grupo DOPA (principal componente del pegamento natural que usan los moluscos para agarrarse a las rocas) que le dota de la capacidad de adherirse espontáneamente a las superficies en medio básico, y que cuenta también con grupos fluorados que le proporcionan la cualidad antiadherente. De esta forma, las superficies recubiertas con este péptido sintético son capaces de hacer frente al perjudicial proceso de biofouling.

Las superficies, tanto de PCL (control) como las de PCL modificadas con péptido, fueron incubadas en un medio de cultivo con bacterias de *E. coli*, y posteriormente, se comparó el número de colonias adheridas a las superficies de PCL con las que se habían pegado a las de PCL recubiertas con péptido tras la incubación, para verificar su actividad antifouling.

Teniendo en cuenta todo lo expuesto, en esta tesis se investigan diferentes combinaciones para combatir infecciones en implantes médicos.

Introduction

1. Drug Eluting Devices

Since the beginning of pharmacological therapy, maintaining steady therapeutic drug concentration levels in the bloodstream has been a major problem. In the conventional systems for administration of drugs, the level of the medicine reaches a maximum and then falls to a minimum, so that the application of a new dosage becomes necessary. When using oral drug administration, high plasma concentration of drug may lead to toxicity, but concentration below the minimum effective may also cause subtherapeutic blood levels and drug resistance in some instances.

Combining the abilities of a medical device with the capability of locally releasing a drug in a controlled way is a solution to clinical problems involving complications associated with device implantation. In this way, the dose necessary to be administered is lower since the drug has to overcome fewer biological barriers (many drugs are inactivated or eliminated by the gastrointestinal system, kidney or liver). The improved sustained release action of these delivery systems also offers additional advantages, such as better patient compliance, as the patient does not need to think about taking medication. Other potential benefit of this type of delivery system is the protection of drugs from being too rapidly metabolized. This added value to medical devices is clearly interesting both clinically and commercially.

Historically, implantable drug delivery systems started in 1938 in London, with the implantation of compressed estrogen pellets subcutaneously to treat a young woman afflicted with premature menopause [1]. In the mid-1960s J. Folkman and D.M. Long investigated the use of silicone rubber as a method for prolonged systemic drug administration, after discovering that the introduction of tubes exposed to anesthesic gases in rabbits made them fall asleep [2]. Nowadays, nanotechnology has enabled the development of more efficient and precise drug eluting devices able to, prompted by external stimuli, perform remotely controlled delivery at different parts of the body.

The surface of a medical device is crucial for its integration within the body, since it constitutes the interfacial barrier between the biological environment and the artificial element. The primary cause of implant associated infections is the formation of a well defined bacterial network on the surface of medical devices, termed biofilm, which is extremely resistant to antibiotics [3,4]. Micro and nanotechnology techniques have made possible to modify the surface by using different strategies: coating with different materials such as polymers or inorganic nanoporous coatings which can be loaded with a broad range of drugs, as well as modifying the topography to form an antifouling surface mimicking the defense mechanisms found in nature, like the skin of the shark [5].

The effectiveness of a drug eluting device depends on the way in which the pharmaceutical is released, determined by the interaction with the matrix. If the drug is released very quickly, the infection may not heal; on the contrary, if the release is delayed, the device cannot overcome the microorganism invasion. An ideal drug delivery system should exhibit an initial burst, in order to respond to the elevated risk of infection from bacteria during surgery or implantation, followed by a sustained release at an effective level for inhibiting the occurrence of latent infection. In this regard, research efforts have focused on the investigation of amorphous solid dispersions (ASDs) as an strategy to deliver bioactive agents with poor aqueous solubility and bioavailability [6]. ASDs have to be stable to avoid drug recrystallization and for this purpose the drug should be completely miscible with the matrix. Exploiting the metastable region to increase the amount of amorphous drug loaded in the device involves the risk of drug recrystallization during the useful life of the device [7]. The release mechanisms found in these miscible systems is defined by an initial burst that will prevent infection and kill the microorganisms found in the implant area before they settle and create a biofilm where antibiotics cannot penetrate, followed by a relatively slow release phase to prevent microbial infections at the implant site during healing.

In most drug eluting devices, the drug is incorporated into a polymeric matrix so that it can be released in a controlled way within the therapeutic margin. Polymers for clinical applications can be broadly classified into biodegradable and non-biodegradable; in non-biodegradable polymers, the release is controlled by diffusion or swelling mechanisms, while in biodegradable polymers the erosion mechanism is also involved [8]. Table I summarizes the most relevant polymers used to produce drug eluting devices. The main advantage of using biodegradable materials for making medical devices is that they do not need to be removed after finishing their service, as they are absorbed or excreted by the body, hence the tissue surrounding can return to its original state, and a follow-up surgery is avoided. In addition, biodegradable polymers can release larger quantities of antibiotics, and their degradation and mechanical properties can be tailored for specific applications [9,10].

Table I. Polymers used for producing drug eluting devices.

Non-degradable	Biodegradable
	Poly(lactide) (PLLA, PDLLA)
Poly(dimethylsiloxane) (Silicone)	Poly(glycolic acid) (PGA)
Polyurethanes (PU)	Poly(lactide-co-glycolide) (PLGA)
Polyethylene (PE)	Poly(ε-caprolactone) (PCL)
Poly(methyl methacrylate) (PMMA)	Poly(hydroxybutyrate-co-hydroxyvalerate) (PHBV)
Poly(tetrafluoroethylene) (PTFE)	Polyhydroxyalkanoates (PHA)
Poly(vinylene fluoride) (PVDF)	Polydioxanone (PDS)
Poly(ethylene-co-vinyl acetate) (PEVA)	Polyanhydrides
Poly(ethylene terephthalate) (PET)	Collagen
	Chitosan

It becomes obvious that many factors need to be considered depending upon each clinical context, i.e., design, biomaterial and drug selection, drug release mechanism, and fabrication method. This introduction reviews the most extensively studied controlled drug eluting devices, as well as recent developments on the micro/nanotechnology scales, and their future challenges. For this purpose we divided medical devices into different systems of the body (see Fig. I): orthopedic devices, breathing stents, gastrointestinal and urinary systems, devices for cardiovascular diseases, neuronal implants, and wound dressings.

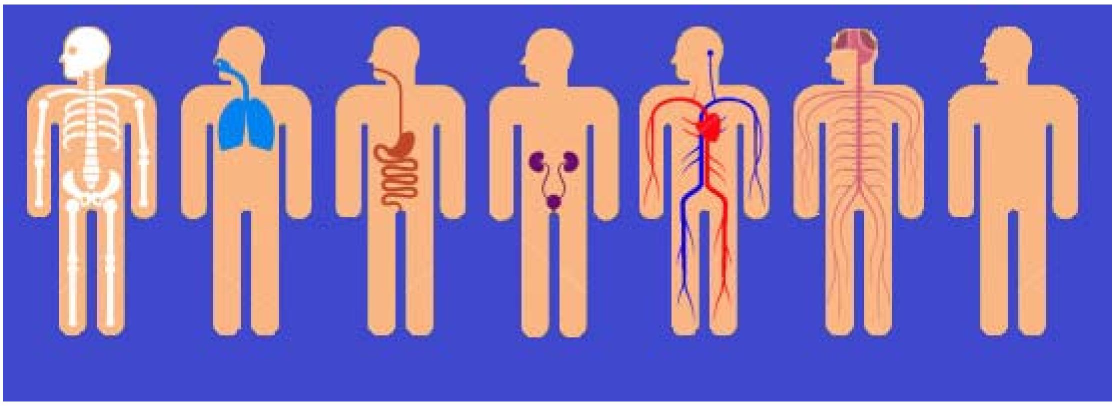

Figure I. Different systems of the body: (a) skeletal system, (b) respiratory system, (c) digestive system, (d) urinary system, (e) circulatory system, (f) nervous system, and (g) integumentary system.

2. Orthopedic Drug Eluting Devices

An orthopedic device is any device that is placed within the body's skeleton to provide stability or to correct problems that currently exist there. This includes orthopedic prostheses, orthopedic fixation devices such as interference screws in the ankle, knee, and hand areas; rods and pins for fracture fixation, screws and plates for craniomaxillo facial repair, bone tissue engineering scaffolds; and, bone cements to anchor artificial joints [11]. A common problem with prosthetic and orthopedic appliances is the infection during the healing process, which often results in the removal of the orthopedic implant and the need for a follow-up operation. Besides, the infection rate after a follow-up surgery is higher (5-40 %) than after the first one [12]. An ideal drug delivery system should be able to release drugs over a period of several months to years in order to prevent "late" infection. Osteomyelitis is the inflammation of the bone caused by an infecting organism introduced from trauma, surgery or implant [13-18]. Conventional therapy with antibiotics is usually unsuccessful in these cases, because there is a poor antimicrobial distribution at the site of infection due to limited blood circulation to infected skeletal tissue, and a high systemic dosage of antibiotics can lead to toxic effects [19]. Therefore, site-specific targeted drug delivery devices would be a good strategy in osteomyelitis treatment [20].

Poly(methyl methacrylate) (PMMA) loaded with an antibacterial agent is commonly used as a non-biodegradable bone cement to prevent osteomyelitis [21-23]. The antibiotics are either premixed by the manufacturer or added by the surgeon in the operating room. Table II shows approved drug eluting bone cements based on PMMA. The release of antibiotic from PMMA begins with an initial burst, followed by a slow release that continues for days to months. Penetration of water in the pore network of the cement, leads to matrix dissolution and outward diffusion of solubilized drug via matrix imperfections; however, less than 10 % of the drug trapped is released [24-30]. PMMA is not biodegradable, which means that with any clinical failure, secondary surgery would be necessary to remove it [31-33]. Besides, this bone cement is limited to antibacterial drugs that are able to withstand the heat generated by polymerization, and both, the heat and residual MMA monomer, can kill healthy bone cells and inactivate the antibiotic [34].

Table II. Commercial PMMA bone cements and beads loaded with antibiotics.

Trade name	Supplier	Matrix	Antibiotic	Treatment	Device
Simplex®	Stryker	PMMA	Tobramycin	Bone infection	Bone cement
Palacos®	Zimmer Biomet		Gentamicin sulphate		
CMW®	DePuy				
Septopal®	Biomet				Bead chains

The main advantage of using biodegradable polymeric cements and implants over PMMA is that they are able to support tissue growt.h and remodeling, and that they are afterwards resorbed, being unnecessary a surgical removal [35]. For example, a fractured bone fixed with a rigid, non-biodegradable stainless steel implant has a tendency for re-fracture upon removal of the implant. The bone does not carry sufficient load during the healing process, because the load is carried by the rigid stainless steel. In contrast, an implant prepared from biodegradable polymer can be engineered to degrade at a rate that will slowly transfer load to the healing bone [36]. PDLLA, PLLA, PLGA, PEG, PLA-PLGA block copolymers and other copolymers are manufactured into biodegradable beads, microspheres, melt-extruded cylinders, and antibiotic loaded implant coatings and films for orthopedic applications [37].

One of the main problems with orthopedic implants is device associated infection caused by bacterial adhesion on the surface and subsequent biofilm formation. The biofilm is a well defined bacterial-network which provides the bacteria with superior survival properties against antibiotics. There is a competition between the integration of the implant into the surrounding tissue and adhesion of bacteria. If bacterial adhesion occurs prior to tissue integration, the implant will be colonized [34]. Therefore, it is critical to prevent the formation of biofilms by inhibiting initial bacterial adhesion or killing bacteria directly. Creation of antifouling surfaces is a good strategy to prevent implant-associated infections [38].

Current antimicrobial strategies in orthopedic devices have focused on coating-based approaches that aim to prevent infection by mitigating biofilm formation on implants. Antibiotic coatings are limited by the duration of drug elution and the risk of developing drug resistance. To overcome these drawbacks, “smart coatings” are being developed. A “smart surface” is designed to be a self-responsive multitask micro-machine that releases antimicrobial (and other) substances after stimulation by microbiological (or other) signals such as bacteria (see Fig. II). Changes in the pH, temperature, as well as mechanical, chemical, and electrical changes in the surroundings of the device, trigger the opening of nanocontainers and the release of a specific substance. As a result, a critical component of a smart micro-device is a sensor unit sensitive enough to detect the stimuli [39].

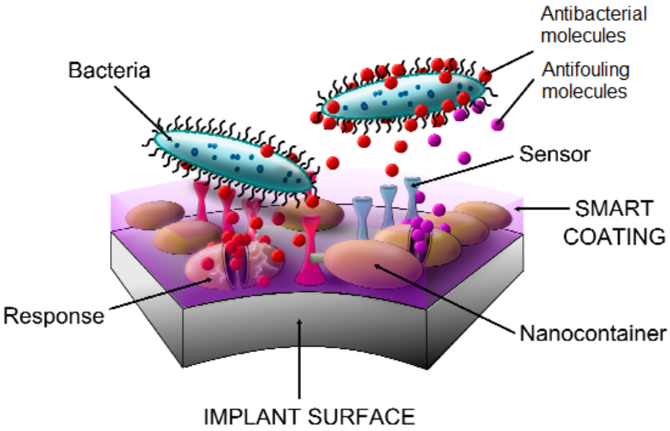
Antibacterial molecules
Bacteria
Antifouling molecules
Sensor
SMART COATING
Response
Nanocontainer
IMPLANT SURFACE

Figure II. Smart coating of an orthopedic device.

Nanotechnology has revolutionized therapeutics, allowing a greater precision of drug delivery, especially beneficial in the field of orthopedics. Though conventional implants like artificial knee, hip joints, plates etc. are still the most implantable commercially, a great amount of research activity has been initiated recently on employing principles of nanotechnology to bone tissue engineering [40]. An example of this is the incorporation of drug-releasing Tunneling Nanotubes (TNT) layers grown on Ti-based implants via anodization, for treating bone related diseases and prevention of post-implantation infections. The process of manufacturing is summarized in Figure III. The nanotubular structure of the TNT coatings enables drug loading, and promotes the adhesion and proliferation of osteoblast cells on the implant surface [8].

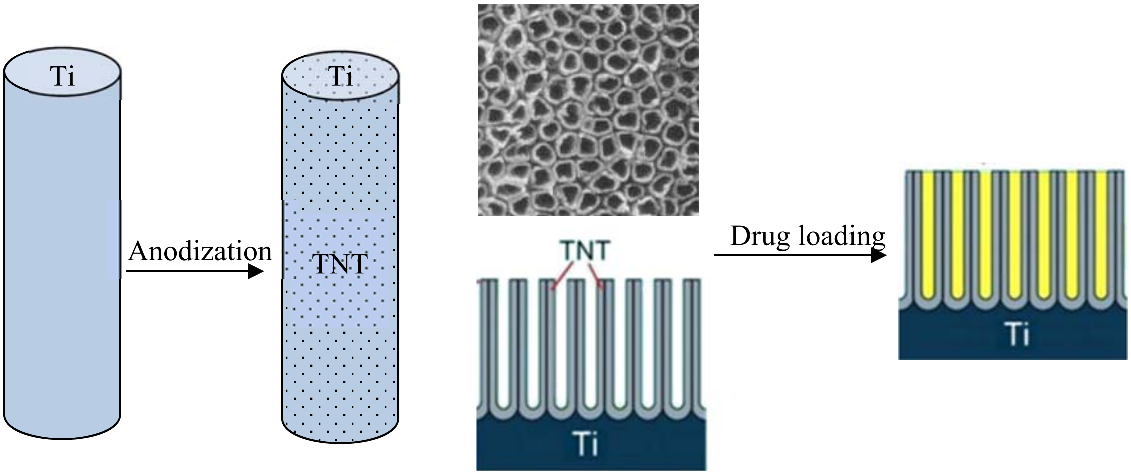

Figure III. Use of TNTs for developing drug-releasing implants.

Bone diseases represent a variety of skeletal-related disorders including defects that cause major mobility hindrance and mortality to human beings. As no effective treatments are available for some of the most common skeleton disorders such as arthritis, osteoarthritis, osteosarcoma, and metastatic bone cancer, there is an urgent need to develop new drugs and drug delivery systems for safe and efficient clinical treatments. In the development of treatments for bone degenerative diseases (osteoarthritis) and bone cancers (osteosarcoma), the balance between medication side effects and treatment efficacy is always an issue. To address these issues and to increase the efficacy of treatment, a targeted delivery using nanotechnology has been widely proposed as a potential strategy. The use of nanoparticles (NPs) for the treatment of bone diseases offers advantages like carrying the drug to its destination while protecting the drug from being dispersed or degraded by body fluids, as well as increasing the solubility of some hydrophobic drugs due to the large surface area of the NPs [41].

3. Drug eluting Stents for Breathing System

A stent is a tube-shaped device that can be inserted into a tubular narrowed passageway or vessel to unblock it and to hold it open. The first bare metal stents displayed short-term functionality, because they became occluded due to malignant ingrowt.h. Immediately after stenting, as a result of the mechanical trauma, the endothelial surface triggered an inflammatory process which led to platelet adhesion, activation, and aggregation, resulting into a fibrin deposition and thrombus formation within the stent [42]. Subsequently, proliferating smooth muscle cells formed a neointimal layer within the stent lumen. Drug-eluting stents (DES) have demonstrated a very high success in preventing in-stent stenosis, since they are able to locally deliver an appropriate concentration of an effective agent to stop this process without systemic toxicity.

Biodegradable polymers that have been used or investigated as a delivery vehicle for stents are PCL, PLGA, and PLA. On the other hand, biodurable polymeric materials used for this purpose are PU, silicone, PEVA and PTFE. Selection of material depends on duration and site of stenting; for example, PLA and PCL have been investigated for tracheal stents (see Fig. IVa), as both are suitable for long term applications due to their slow degradation rate. Silicone stents block mucociliary clearance, i.e., the mechanism that removes mucus and other material from the lungs. On the contrary, biodegradable stents cause minimal interference in the mucociliarity function and reduce stent induced inflammatory reaction, with the advantage of that they can be loaded with bioactive agents to avoid airway stenosis [43]. Bioresorbable external tracheal stents have been investigated for solving the problem of limited tracheal growt.h in children; they are used for supporting the neonatal trachea until the airway matures, and afterwards, they can be totally resorbed with no need of a removal procedure [44-47].

In cases of sinusitis and nasal polyps where sinus surgery is indicated, there is a long period for wound healing after surgical procedure. Sinus stents loaded with anti-inflammatory compounds could be helpful for post-operative use, due to inability of topical application to reach hidden sinus structures, to avoid the side effects of oral steroid therapy [48]. Another use for DES is the palliation of emphysema in patients who cannot undergo lung transplantation. Emphysema causes shortness of breathing, because of the destruction of the alveoli (small sacs) that promote oxygen exchange between the air and the bloodstream. As can be seen in Figure IVb, airway bypass is a technique to create passages between pulmonary parenchyma and bronchial airways. The success of this technique is limited due to tissue ingrowt.h, since most stents become obstructed within a week due to mucus filling or development of tissue layer over the stent ends [49], making therefore preferable the use of biodegradable DES.

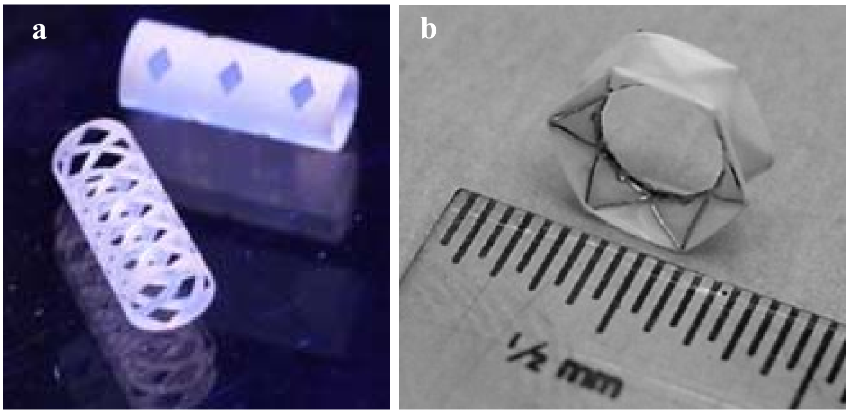

Figure IV. (a) Tracheal stents, and (b) airway bypass stent for emphysema treatment.

Table III. Commercial drug eluting devices for breathing system.

Trade name	Supplier	Matrix	Antibiotic	Treatment	Device
Propel®	Intersect Ent	PLGA	Mometasone furoate (steroid)	Chronic sinusitis	Sinus stent
Relieva Stratus®	Acclarent	PMMA	Triamcinolone acetonide		Catheter with micropore reservoir
Exhale®	Broncus	Silicone	Paclitaxel	Emphysema	Airways bypass stent

4. Drug Eluting Gastrointestinal Stents

Gastrointestinal stents are a tool for relieving obstructive malignancies of gastrointestinal tract. There are biliar, pancreatic, esophageal, colonic, and duodenal stents, in order to face the obstruction caused by cancer where a surgical intervention could be very risky [49].

Boston Scientific has developed the Polyflex® esophageal stent made of silicone for esophageal stenosis (see Fig. V). However, the use of bioresorbable materials for this kind of stents is currently being explored, and there is no drug eluting gastrointestinal device commercially available [50].

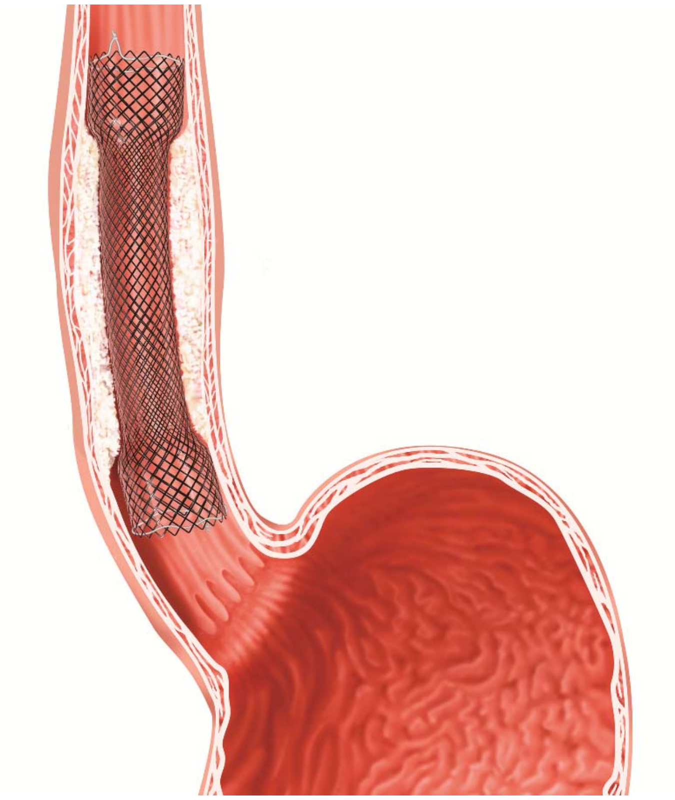

Figure V. Esophageal stent for strictures caused by malignant tumors.

5. Antimicrobial Urinary Stents

Catheter-associated urinary tract infection is the most common hospital acquired (nosocomial) infection; one out of four hospitalized patients receives an indwelling urinary catheter at some point of their stay (see Fig. VIa) [51]. In about 70 % of the long-term stenting cases, when there are intractable urinary problems such as chronic urinary retention or incontinence not treatable by other means, patients require analgesics to overcome stent related pain, and also antibacterial agents to avoid biofilm formation which often leads to infections [49]. In this regard, surface modification of the stents is a suitable strategy to interfere initial adhesion of bacteria and biofilm formation, therefore reducing catheter associated urinary tract infections. One simple method is to immerse the stent into antimicrobial solution prior to its insertion (see Fig. VIc). However, this method provides short-term protection against infection, and is unlikely to load enough drug to allow the prolonged release required to prevent bacterial infection over long periods, since the binding is weak and antimicrobial coatings are depleted rapidly by urine flow. Alternatively, the polymeric matrix can be also loaded with a miscible (amorphous) drug that would be released for longer times. The only clinical drug eluting ureteral stent (see Fig. VIIb) found is Triumph® (Boston Scientific) made of an olefinic block copolymer loaded with triclosan.

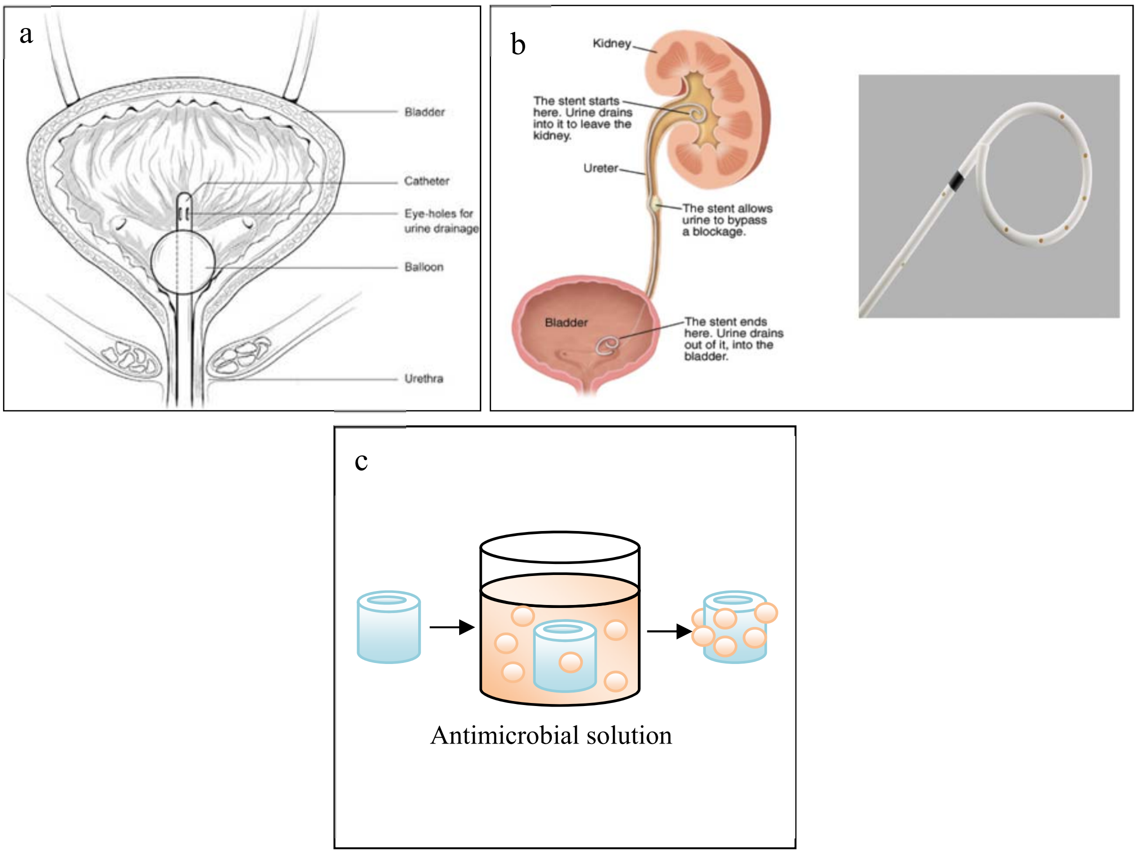
a
Bladder
Catheter
Eye-holes for urine drainage
Balloon
Urethra
b
Kidney
The stent starts here. Urine drains into it to leave the kidney.
Ureter
The stent allows urine to bypass a blockage.
Bladder
The stent ends here. Urine drains out of it, into the bladder.
c
Antimicrobial solution

Figure VI. (a) Catheterized urinary bladder: the catheter is inserted into the bladder through the urethra, and the balloon is then inflated with water to prevent the catheter from slipping out of the bladder, (b) ureteral stent to treat the obstruction of a stone, and (c) impregnation of a urinary stent with antimicrobials.

6. Cardiovascular Disease Treatment

According to the World Health Organization (WHO), heart diseases causing arterial obstruction are the major cause of death accounting 15 million deaths in 2015 (27 % of all the deaths worldwide). Infection of intravascular devices for vascular access and vascular prostheses for the replacement or bypass of damaged arteries is a serious event. In this context, drug eluting cardiovascular devices have revolutionized the treatment of this kind of illnesses. Thus, drug eluting stents for the treatment of coronary artery disease have managed to reduce restenosis by 70 % across all patients when compared to bare metal stents [52]. DESs have demonstrated to overcome restenosis after implantation by releasing anti-inflammatory, immunosuppressive and cytostatic drugs, such as tacrolimus, sirolimus, paclitaxel, etc.

Coronary artery disease is almost synonymous of stent implantation or balloon angioplasty to mechanically recover the vessel dimensions, in order to ensure a smooth blood flow. Both procedures induce trauma to the vessels and the body responds in the form of neointimal hyperplasia and restenosis, with the result of an additional layer in the lumen. Anti-proliferative drugs for this kind of intervention may diminish the adverse events, though systemically administered have shown disappointing results in preventing in-stent restenosis, due to poor drug bioavailability, toxicity and insufficient drug concentration at injury sites. Moreover, the loss of control over the drug release may postpone the regeneration of endothelium and raise the risk of adverse events. That is the reason for using polymeric drug eluting stents.

Furthermore, coronary stents are temporary implants which perform scaffolding during healing period of a vascular injury. Therefore, a biodegradable vascular drug eluting stent will be naturally resorbed and metabolized by the body when no longer needed. As there is no permanent implant, the coronary artery can return to its native state, avoiding late stent thrombosis risk and foreign body reaction. Biodegradable stents can be suitable for children with congenital cardiovascular diseases, because no additional surgery is required to replace the stent, as the patient grows older. The most representative examples of biopolymers used for cardiovascular treatment are self-expanding and shape-memory biocomplatible polymers, such as PLLA or PLGA.

It is crucial to control the drug release rate from the interface of a coronary stent; for this purpose, there are different strategies such as grooving the surface of the stent, using nanoscale carriers, or improving coating technology. Nanostructured surfaces in a stent enhance endothelial cell growt.h, minimizing late stent thrombosis, particularly relevant for cardiovascular stents [51.] By coating stainless steel stents with inorganic nanopores via electrochemical anodization of aluminum, cylindrical nanopores can be obtained for drug loading (see Fig. VIIa) [11]. Another strategy to obtain a controlled drug release is to obtain a microporous surface on the abluminal side of the metallic stents to store the drug and then, to cover these reservoirs with a biodegradable polymer layer (PLA) (see Fig. VIIb). As the reservoirs are embedded on the outer stent surface, the drugs are released directly to the blood vessel wall and not washed away by the blood stream [53]. The progress of micro- and nanotechnology have permitted to produce different nanotopographies, providing more sites for the drug or polymer to adsorb than would be available on flat surfaces.

In the field of the nanotechnology, another strategy is to coat the stents with polymeric nanocarriers bearing anti-restenotic drugs. For example, a catheter balloon coated with nanoparticles would release nanocarriers locally when inflated to expand, providing a burst release of the drug at the beginning, followed by a slow drug release from the polymeric matrix (see Fig. VIIc) [55]. Combining grooves and nanoparticles, the drug release behavior can be further tuned and improved [56].

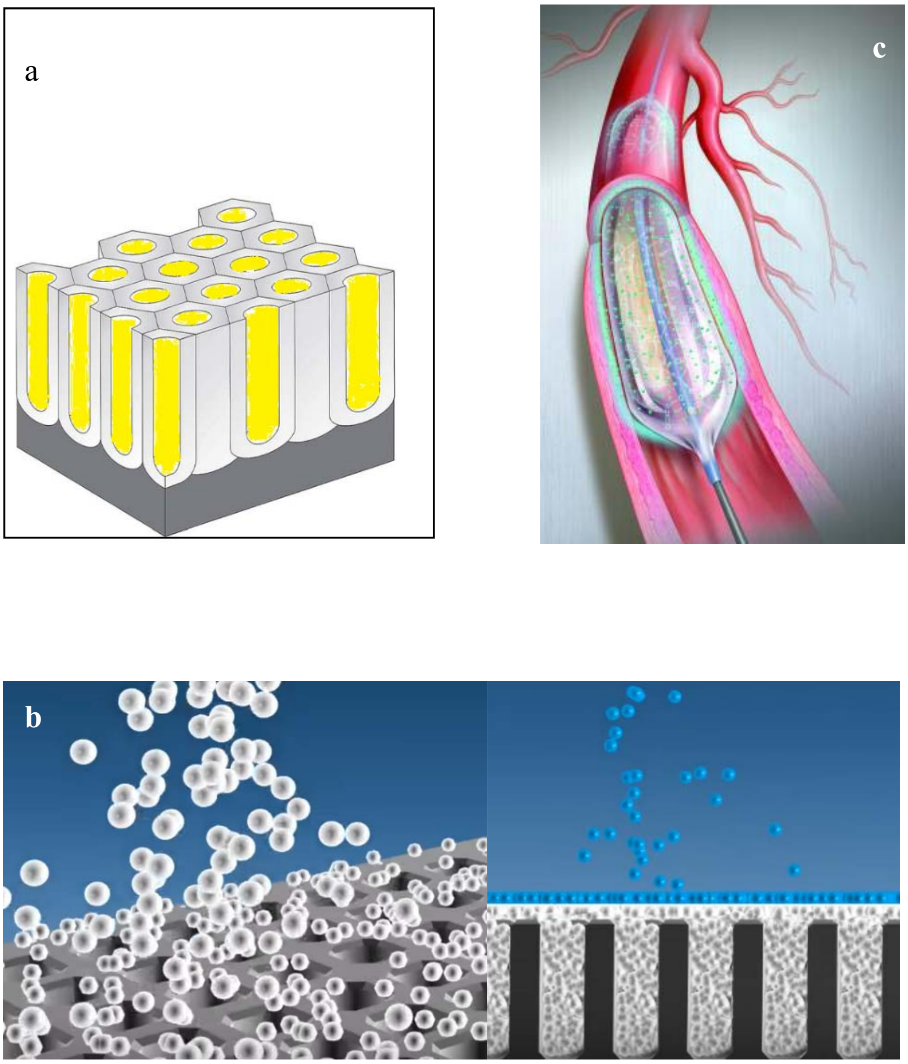

Figure VII. (a) Nanoporous anodic alumina coating for drug-release, (b) drug loading of the micro-pits of a microporous surface followed by a top-coating with a biodegradable polymeric layer, and (c) drug eluting balloon.

Table IV. Commercial drug eluting coronary stents.

Trade name	**Supplier**	**Matrix**	**Drug**	**Treatment**
Cypher®	Johnson& Johnson/Cordis	PEVA blend with PBMA	Sirolimus	In-stent restenosis
Taxus®	Boston Scientific	Poly(styrene-b-isobutylene-b-styrene) (SIBS)	Paclitaxel	
Absorb®	Abbot Vascular	PLLA	Everolimus	
Champion®	Guidant			
Synergy®	Boston Scientific	PLGA		
Yukon®	Traslumina	Microporous stainless steel	Rapamycin	
BioFreedom®	Biosensors international	Micro-structured abluminal surface	Biolimus A9	High bleeding risk

Electrospinning of some polymers with drugs into ultrafine fibers is another way to enhance the coating of a DES. Their high surface to volume ratio can increase drug loading, cell attachment and mass transfer properties [54].

7. Neuronal Implants

Implantation of macro and microdevices into the brain is increasingly used for treatment of neurological disorders, including deafness, paralysis, blindness, epilepsy, and Parkinson's disease. Thus, the interest in the properties of the interfaces between neurons and external devices to restore or supplement the function of the nervous system lost during injury or disease. Since many elements of neurons have nanoscale dimensions, it is required a neural interface with nanoscale components; i.e. biocompatible nanomaterials that mimic neural tissue characteristics, cause minimal inflammation and neuronal cell loss, and are functional for a long period of time [57]. Incorporation of drugs and bioactive molecules into electrically active nanomaterials such as carbon nantotubes and conducting polymer nanotubes, can improve the biocompatibility of neural electrodes, reduce reactive tissue response, and promote neural process outgrowt.h, by a controlled release of the drug (see Fig. VIIIa) [58]. Hydrogels loaded with drugs are a good choice for coating neural electrodes to decrease the mechanical mismatch between stiff electrodes and soft brain tissue, reducing tissue responses at the electrode-tissue interface [59].

In neural diseases the dose is crucial, because the therapeutic window is generally narrow and toxicity results in severe side effects. Systemically, these drugs are required in a higher concentration owing to fencing properties of the blood-brain barrier, resulting in peripheral side effects. Moreover, most of the neural treatments need long term therapy. Hence the relevance of biodegradable polymers as delivery tools in the treatment of neural ailments, owing to their ability for sustained release at the focal site in neuronal tissue, their versatility of design and release time, as well as their biocompatibility.

Among brain related diseases, malignant glioma is the most widespread type of brain tumor with very low survival rate. Therefore, alternative therapies are urgently needed to treat this disease in a more effective way. Malignant gliomas are considered to be most nasty to treat, due to inaccessibility, post-surgical recurrence and associated complications [60]. To deal with tumor recurrence, there are post-surgical implants of anticancer drugs designed to deliver the drug directly into the surgical cavity created after the glioma has been surgically excised (Gliadel®) (see Fig. VIIIb).

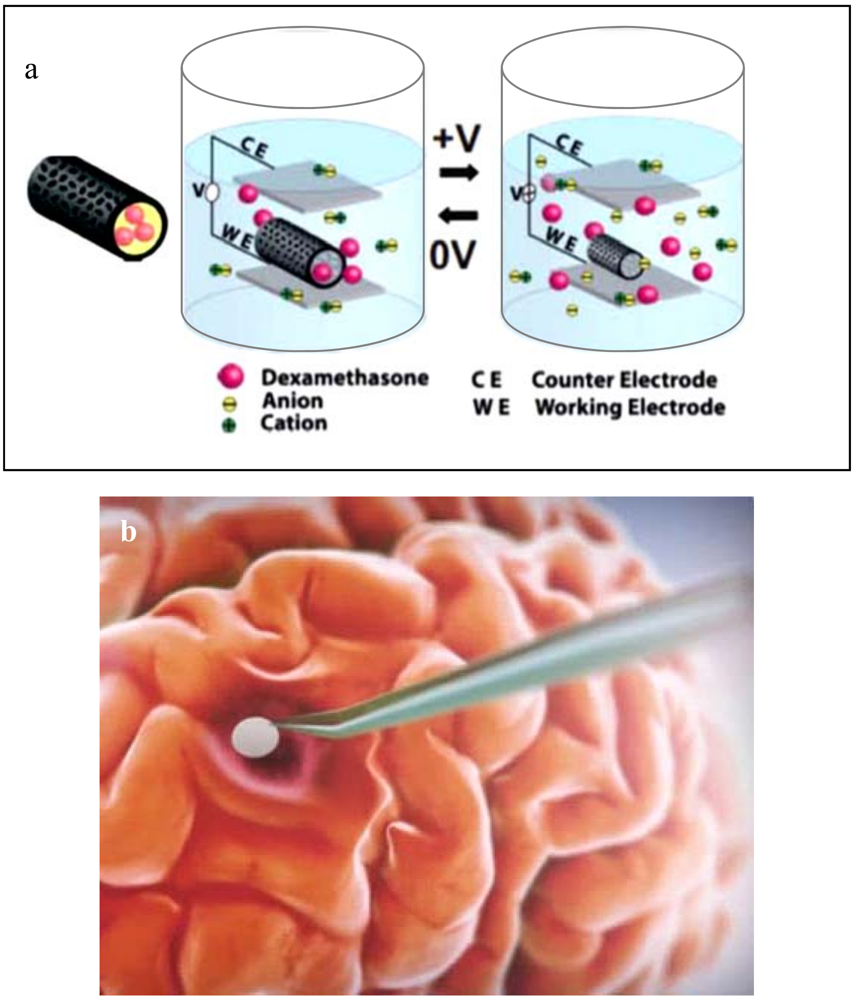

Figure VIII. (a) Controlled release of dexamethasone (an anti-inflammatory drug) from PLGA nanofibers, coated with poly(3,4-ethylenedioxythiophene) (PEDOT) conducting polymer. The PEDOT nanotubes were actuated by applying a bias voltage of +1V. Expansion and contraction of conducting polymer cavities after electrochemical stimulation produced a mechanical force creating pressure within the nanotubes, resulting in a controlled drug release, and (b) local chemotherapeutic agent Gliadel® Wafer**.**

Epilepsy is a disease characterized by unpredictable seizures which restrict patients' daily activities. Oral anti-epileptic therapy results in systemic and central nervous system side effects, because of a non-localized drug exposure. In this regard, intercranial adenosine releasing biomedical implants can be a good alternative.

Considering that deep brain tissue penetration is needed for therapeutic efficacy of neurological drugs, implants based on nanotechnology are a promising avenue for sustained delivery of bioactive agents towards management of lifelong neurodegenerative disorders, e.g., nanoparticles of dopamine entrapped in alginate crosslinked scaffolds for site specific delivery in Parkinson treatment [62]. A further example are intracranially injectable gel-based implants loaded with nanodrugs for treating central nervous system diseases [63].

Biomedical engineering is developing devices that can substitute a motor, sensory or cognitive process, damaged as a result of an injury or a disease, named neural prostheses. Recently, a new area of nanoprosthetics is emerging with the use of carbon nanomaterials (graphene, carbon nanotubes (CNT), and carbon nanofibers (CNF)). Their biocompatibility, mechanical stability and high electrical conductivity make these carbon nanomaterials good candidates for deep brain stimulation to restore neuronal activity. CNTs and CNFs are employed in the form of 3-D polymeric nanoscaffolds for nerve tissue regeneration [64], and also nanocoatings based on CNTs and polymers are being researched for improving conventional microelectrodes [65].

Table V. Commercial drug eluting devices for brain disorders.

Trade name	**Supplier**	**Matrix**	**Drug**	**Treatment**	**Device**
Gliadel®	Eisai	Polifeprosan 20	Carmustine	Tumor ihibition	Post-glioma surgery wafers
DepoCyt®	Sigma-Tau	Liposome	Cytarabine	Lymphomatous meningitis treatment	Intrathecal injection

8. Wound Dressing

A wound is a damaged area of the body, such as a cut or a hole in the skin that includes tissue lost, and the regeneration of damaged skin includes complex tissue interactions between cells. Furthermore, a wound provides an ideal environment for bacterial growt.h; in burns, infection is the major complication after the initial period of shock. A wound dressing is a sterile pad or compress applied to a wound to promote healing and protect the wound from further harm [34]. It is designed to be in direct contact with the wound, while a bandage is most often used to hold a dressing in place (many modern dressings are self-adhesive). Aside from the major function of reducing the risk of infection, dressings are also important to stop bleeding and start clotting so that the wound can heal. There is a big variety of dressings depending on the type, severity and position of the wound. To give an example, hydrocolloid dressings are used on draining wounds, whereas hydrogels are used to provide hydration to the wound (see Fig.IX).

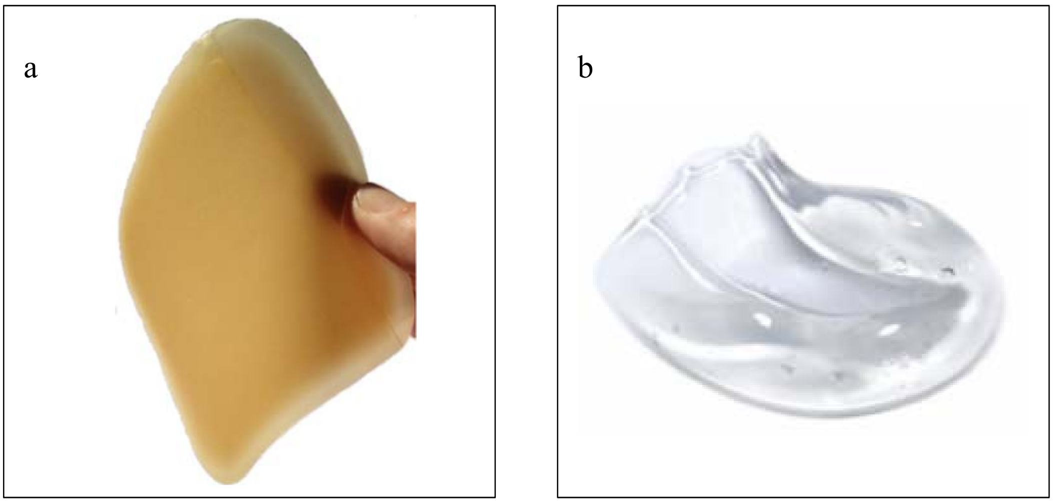

Figure IX. (a) Hydrocolloid wound dressing, and (b) AFAR™ hydrogel wound dressing.

Historically, the use of herbal plants has always had benefits in the wound-closure process. A new generation of drug eluting wound dressings with antimicrobial effect, provides obvious advantages over traditional wound dressings in preventing bacterial infection. Additionally, bioresorbable dressings can deal with the painful and risky process of changing a temporary dressinng. A good example to illustrate this are the antimicrobial PCL/thymol blends, with potential use as biodegradable wound dressings accelerating wound healing due to the anti-inflammatory and antibacterial properties of thymol [7].

Table VI. Commercial drug eluting wound dressings.

Trade name	Supplier	Matrix	Drug	Treatment	Device
Contreet®	Coloplast	Polyurethane Foam	Silver	Moderate to highly exuding wounds	Pad
Silvercel®	Acelity	Nylon fibers	Silver	Chronic wounds	
Acticoat®	Smith&Nephew	Polyester	Silver	Burns	Gauze
Collatamp®	Eusa Pharma	Collagen	Gentamicin	Surgeries with high risk of infection	Sponge
Septocoll®	Biomet	Collagen	Gentamicin	Hemostasis in surgeries	Fleece

9. Future of Drug Eluting Devices

Most new chemical entities have poor aqueous solubility and consequently poor oral bioavailability, thus, drugs administered orally can remain undissolved in the gastrointestinal tract instead of being absorbed by the organism [66]. Moreover, in conventional drug release systems as the concentration of the medicine falls down, a new dosage is required. The challenge of drug eluting devices is focused on the control of the releasing rate to keep the concentration within the therapeutic window, personalized for each patient and therapy. This on demand drug delivery requires drug-releasing devices that can decide the suitable dosage at convenient time, in other words, intelligent drug releasing devices. Microchips Biotech has developed a technology of microchip-based implant that can store hundreds of therapeutic doses over months and years, and release each dose at precise times. Each implant contains micro-reservoirs etched into a silicon wafer (see Fig. X) which store up to 1 mg of drug. The implant is activated by a wireless signal that applies a voltage to the gold foil, which is hermetically sealing the small compartments, with resulting electrochemical dissolution of the cover and release of the drug on a pre-programmed dosing schedule. In addition, the implant can be built with sensors that release drug in response to physiological or metabolic changes in the patient.

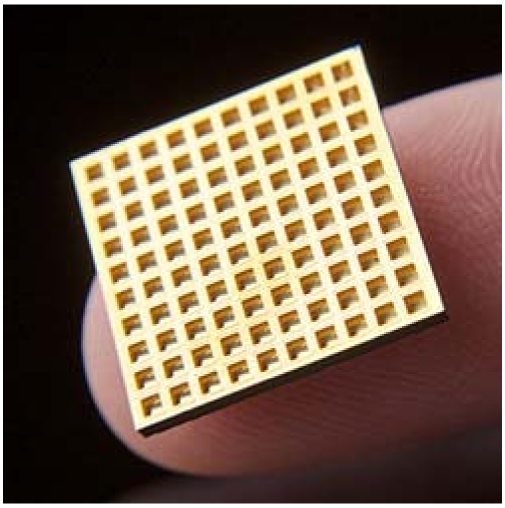

Figure X. Implants developed by Microchips Biotech, Inc.

Over the years, medical devices have changed from mere support to smart appliances aiding the healing process. Another groundbreaking advance in the field of biomedical engineering is the advent of micro/nanorobots. Medical micro/nanorobots may be capable of carrying a bioactive compound accurately to any part of the body (even to regions like eyes and nervous system which are otherwise difficult to reach) through external wireless steering. Some researchers fabricated artificial flagella to create entirely autonomous robots [67]. Furthermore, as our understanding continues to increase of which DNA sequences encode for which diseases, we are able to identify which sequences in the same individual DNA may be used to predict precise therapeutic regimes for optimum treatment of those diseases in each individual. Such “personalized medicine” will place demands on the drug delivery scientist to be more biologically precise and accurate with our “controlled” delivery systems [68].

Many technical and commercial challenges should be tackled to improve the current drug eluting device technology, but the tight health care regulations make the future uncertain.

10. Conclusions

Drug eluting devices for treating different diseases affecting different functions of the human body have been reviewed. In most cases, drug-releasing devices provide greater therapeutic efficacy than conventional oral or intravenous formulations, offering alternative ways to deliver therapeutics to any part of the body and reducing the side effects associated with excessive dosages of highly toxic drugs [69-81].

This review makes clear that the development of drug delivery devices needs a combination of knowledge, involving material scientists, engineers, medical scientists, biologists and clinicians. Significant advances will only be made through multidisciplinary teams that utilize the latest advances in the biological, chemical, physical, and engineering sciences [82-87]. Studies to discover the ideal material, shape, size and dosage for a tailored drug eluting medical device are still needed.

The surface of medical devices provides an excellent platform fort the formation of bacterial colonies or biofilms, producing life-threatening infections across most types of implanted devices. This problem could be overcome through the development of novel antifouling materials based on nature.

Drug release profiles of bioactive agents, mechanical and physical properties of the device, degradation rate and bacterial inhibition must be elucidated in order to achieve the desired properties for each application. Pharmaceutical companies and device manufactures are actively seeking development opportunities for new drug/device combination products based on the existing raw materials and drugs. The future is a drug eluting device that “knows” where, when and how much drug is needed for treating a specific illness.

References

[1] A. Mitra, C.H. Lee, K. Cheng, “Advanced Drug Delivery”, *John Wiley & Sons*, 2013.

[2] A.K. Dash, G.C. Cudworth, “Therapeutic applications of implantable drug delivery systems”, *Journal of Pharmacological and Toxicological* Methods, 1998, **40**, 1–12.

[3] E.M. Hetrick, M.H. Schoenfisch, “Reducing implant-related infections: active release strategies”, *Chem. Soc. Rev.*, 2006, **35(9)**, 780–789.

[4] P. Wu, D.W. Grainger, “Drug/device combinations for local drug therapies and infection prophylaxis”, *Biomaterials*, 2006, **27**, 2450-2467.

[5] N. Zhao, Z. Wang, C. Cai, H. Shen, F. Liang, D. Wang, C. Wang, T. Zhu, J. Guo, “Bioinspired materials: from low to high dimensional structure”, *Adv. Mater.*, 2014, **26**, 6994-7017.

[6] S.B. Teja, S.P. Patil, G. Shete, S. Patel, A.K. Bansal, “Drug-excipient behavior in polymeric amorphous solid dispersions”, *J. Excipients and Food Chem.*, 2013, **4(3)**,70-94.

[7] E. Sanchez-Rexach, I. Martínez de Arenaza, J.R. Sarasua, E. Meaurio, “Antimicrobial poly(ε-caprolactone)/thymol blends: Phase behavior, interactions and drug release kinetics”, *European Polymer Journal*, 2016, **83** ,288–299.

[8] A. Santos, M.S. Aw, M. Bariana, T. Kumeria, Y. Wang, D. Losic, “Drug-releasing implants: current progress, challenges and perspectives”, *J. Mater. Chem.* B, 2014, **2**, 6157–6182.

[9] J. Fernández, A. Etxeberria, J.R. Sarasua, “In vitro degradation studies and mechanical behavior of poly ε-caprolactone-co-δ-valerolactone and poly ε-caprolactoneco-L-lactide with random and semi-alternating chain microstructures”, *European Polymer* Journal, 2015, **71**, 585-595.

[10] J. Fernández, A. Larranaga, A. Etxeberria, J. R. Sarasua, "Ethylene brassylate-co-δ-hexalactone biobased polymers for application in the medical field: synthesis, characterization and cell culture studies", *RSC Advances*, 2016, **6**, 22121-22136.

[11] J.C. Middleton, A.J. Tipton,"Synthetic biodegradable polymers as orthopedic devices", Biomaterials, 2000, **21**, 2335-2346.

[12] A. Trampuz, A.F. Widmer, "Infections associated with orthopedic implants", *Curr. Opin. Infect. Dis.*, 2006, **19**, 349−356.

[13] W.T. Bourque, M. Gross, B.K. Hall, "A reproducible method for producing and quantifying the stages of fracture repair", *Lab. Anim. Sci.*, 1992, **42**, 369–374.

[14] G. Cox, T.A. Einhorn, C. Tzioupis, P.V. Giannoudis, "Bone-turnover markers in fracture healing", *J. Bone Joint Surg. Br.*, 2010, **92**, 329–334.

[15] J.E. Schroeder, R. Mosheiff, Tissue engineering approaches for bone repair: concepts and evidence, *Injury*, 2011, **42**, 609–613.

[16] T. Einhorn, "Mechanisms of fracture healing", *Hosp. Pract. Off. Ed.*, 1991, **26**, 41–45.

[17] T.A. Einhorn, "The cell and molecular biology of fracture healing", *Clin. Orthop. Relat. Res.*, 1998, **355**, S7–S27.

[18] C.P. Frutos, P.E. Diez, J.M. Barrales-Rienda, G. Frutos, "Validation and in vitro characterization of antibiotic-loaded bone cement release", *Int. J. Pharm.*, 2000, **209(1-2)**, 15–26.

[19] J.D. Smilack, W.H. Flittie, T.W. Williams Jr., "Bone concentrations of antimicrobial agents after parenteral administration", *Antimicrob. Agents Chemother.* , 1976, **9(1)**, 169–171.

[20] S.B. Trippel, "Antibiotic-impregnated cement in total joint arthroplasty", *J. Bone Joint Surg. Am.*, 1986, **68(8)**, 1297–302.

[21] Y.Y. Huang, T.W. Chung, “Microencapsulation of gentamicin in biodegradable PLA and/or PLA/PEG copolymer”, *J. Microencapsul.*, 2001, **18(4)**, 457–65.

[22] D. Yu, J. Wong, Y. Matsuda, J.L. Fox, W.I. Higuchi, M. Otsuka, “Selfsetting hydroxyapatite cement: a novel skeletal drug delivery system for antibiotics”, *J. Pharm. Sci.*, 1992, **81(6)**, 529–31.

[23] D.A. Winnger, R.J. Fass, “Antibiotic-impregnated cement and beads for orthopedic infections”, *Antimicrob Agents Chemother*, 1996, **40(12)**, 2675–9.

[24] M. Baro, E. Sanchez, A. Delgado, A. Perera, C. Evora, “In vitro–in vivo characterization of gentamicin bone implants”, *J. Controlled* Release, 2002, **83(3)**, 353–64.

[25] E.J. Harper, “Bioactive bone cements”, *Proc Inst Mech Eng [H]*, 1998, **212(2)**, 113–20.

[26] D. Stengel, K. Bauwens, J. Sehouli, A. Ekkernkamp, F. Porzsolt, “Systematic review and meta-analysis of antibiotic therapy for bone and joint infections”, *Lancet Infect* Dis, 2001, **1(3)**, 175–88.

[27] C.E. Edmiston Jr, M.P. Goheen, “Studying bacterial adhesion to antibiotic impregnated polymethyl methacrylate” *In Handbook of bacterial adhesion, Y. H. An, R. J. Friedman Eds., Totowa, NJ: Humana Press Inc.*, 2000, 599–608.

[28] K. Kanellakopoulou, E.J. Giamarellos-Bourboulis, “Carrier systems for the local delivery of antibiotics in bone infections”, *Drugs*, 2000, **59(6)**, 1223–32.

[29] F.Y. Chiu, C.M. Chen, J. Lin Chien-Fu, W.H. Lo, “Cefuroximeimpregnated cement in primary total knee arthroplasty: a prospective, randomized study of three hundred and forty knees”, *J Bone Joint Surg Am*, 2002, **84-A(5)**, 759–62.

[30] P.D. Levin, “The effectiveness of various antibiotics in methyl methacrylate*”, J. Bone Jt. Surg. Br.*, 1975, **57 (2)**, 234–237.

[31] A.S. Baker, L.W. Greenham, “Release of gentamicin from acrylic bone cement. Elution and diffusion studies”, *J. Bone Joint Surg. Am.*, 1988, **70(10)**, 1551–7.

[32] F.R. DiMaio, J.J. O'Halloran, J.M. Quale, “In vitro elution of ciprofloxacin from polymethylmethacrylate cement beads”, *J.* Orthop. Res., 1994, **12(1)**, 79–82.

[33] T. Miclau, L.E. Dahners, R.W. Lindsey, “In vitro pharmacokinetics of antibiotic release from locally implantable materials”, *J. Orthop. Res.*, 1993, **11(5)**, 627–632.

[34] M. Zilberman, J.J. Elsner, “Antibiotic-eluting medical devices for various applications”, *Journal of Controlled* Release, 2008, **130**, 202–215.

[35] B. Rutledge, D. Huyette, D. Day, J. Anglen, “Treatment of osteomyelitis with local antibiotics delivered via bioabsorbable polymer”, *Clin. Orthop. Relat. Res.*, 2003, **411**, 280–287.

[36] K.A. Athanasiou, C.E. Agrawal, F.A. Barber, S.S. Burkhart, “Orthopaedic applications for PLA/PGA biodegradable polymers”, *J. Arthrosc. Relat. Surg.*, 1998, **14(7)**, 726-37.

[37] K. Gulati, M. Sinn Aw, D. Losic, “Drug-eluting Ti wires with titania nanotube arrays for bone fixation and reduced bone infection”, *Nanoscale Res. Lett.*, 2011, **6**, 571.

[38] S. Nir, M. Reches, “Bio-inspired antifouling approaches: the quest towards non-toxic and non-biocidal materials”, *Current Opinion in Biotechnology*, 2016, **39**, 39:48–55.

[39] J. Gallo, M. Holinka, C.S. Moucha, “Antibacterial surface treatment for orthopaedic implants”, *Int. J. Mol. Sci.*, 2014, **15**, 13849-13880.

[40] A. Arsiwala, P. Desai, V. Patravale, “Recent advances in micro/nanoscale biomedical implants", *Journal of Controlled* Release, 2014, **189**, 25-45.

[41] W. Gu, C. Wu, J. Chen, Y. Xiao, “Nanotechnology in the targeted drug delivery for bone diseases and bone regeneration”, *Int. J. Nanomedicine*, 2013, **8**, 2305–2317.

[42] T. Htay, M.W. Liu, “Drug-Eluting Stent: A Review and Update”, *Vasc Health Risk Manag.*, 2005, **1(4)**, 263–276.

[43] Y.K. Chao, K.S. Liu, Y.C.Wang, Y.L. Huang, S.J. Liu, “Biodegradable Cisplatin-eluting tracheal stent for malignant airway obstruction: in vivo and in vitro studies*, Chest*, 2013, **144**, 193–199.

[44] A.L. Rafanan, A.C. Mehta, “Stenting of the tracheobronchial tree”, *Radiol. Clin. North Am.*, 2000, **38**, 395–408.

[45] T.C. Robey, P.M. Eiselt, H.S. Murphy, D.J. Mooney, R.A. Weatherly, “Biodegradable external tracheal stents and their use in a rabbit tracheal reconstruction model”, Laryngoscope, 2000, **110**, 1936–42.

[46] H. Lochbihler, J. Hoelzi, H. Dietz, “Tissue compatibility and biodegradation of new absorbable stents for tracheal stabilization: an experimental study”, *J. Pediatr. Surg.*, 1997, **32**, 717–20.

[47] M. Zilberman, R.C. Eberhart, “Drug-eluting bioresorbable stents for various applications”, *Annu. Rev. Biomed. Eng.*, 2006, **8**, 153-180.

[48] W. Hosemann, M.E. Wigand, U. Gode, F. Langer, I. Dunker, “Normal wound healing of the paranasal sinuses: clinical and experimental investigations”, *Eur. Arch. Otorhinolaryngol*, 1991, **248**, 390–394.

[49] M. Shaikh, G. Kichenadasse, N.R. Choudhury, R. Butler, S. Garg, “Non-vascular drug eluting stents as localized controlled drug delivery platform: Preclinical and clinical experience”, *Journal of Controlled Release*, 2013, **172**, 105–117.

[50] P. Hindy, J. Hong, Y. Lam-Tsai, F. Gress, “A Comprehensive Review of Esophageal Stents”, *Gastroenterol Hepatol*, 2012, **8(8)**, 526–534.

[51] K.S. Brammer, S. Oh, J.O. Gallagher, S. Jin, “Enhanced cellularmobility guided by TiO_2 nanotube surfaces”, *Nano Lett.*, 2008, **8**, 786–793.

[52] N. Kukreja, Y. Onuma, P.W. Serruys, “Future directions of drug-eluting stents”, *J. Interv. Cardiol.*, 2009, **22**, 96–105.

[53] C. Tamburino, M.E. Di Salvo, D. Capodanno, P. Capranzano, R. Parisi, F. Mirabella, F. Scardaci, G. Ussia, A.R. Galassi, D. Fiscella, R. Mehran, G. Dangas, “Real world safety and efficacy of the janus tacrolimus-eluting stent: long-term clinical outcome and angiographic findings from the tacrolimus-eluting stent TEST registry”, *Catheter. Cardiovasc. Interv.*, 2009, **73**, 243−248.

[54] T. Hu, J. Yang, K. Cui, Q. Rao, T. Yin, L. Tan, Y. Zhang, Z. Li, G. Wang, “Controlled slow-release drug-eluting stents for the prevention of coronary restenosis: recent progress and future prospects”, *Appl.* Mater. Interfaces, 2015, **7**, 11695−11712.

[55] U. Westedt, L. Barbu-Tudoran, A.K. Schaper, M. Kalinowski, H. Alfke, T. Kissel, “Effects of different application parameters on penetration characteristics and arterial vessel wall integrity after local nanoparticle delivery using a porous balloon catheter”, *Eur. J. Pharm. Biopharm.*, 2004, **58,** 161–168.

[56] J. Yang, Y. Zeng, C. Zhang, Y.X. Chen, Z. Yang, Y. Li, X. Leng, D. Kong, X.Q. Wei, H.F. Sun, C.X. Song, “The prevention of restenosis in vivo with a VEGF gene and paclitaxel co-eluting stent”, *Biomaterials*, 2013, **34**, 1635−1643.

[57] P. Fattahi, G. Yang, G. Kim, M.R. Abidian, “A Review of organic and inorganic biomaterials for neural interfaces”, *Adv Mater*, 2014, **26(12)**, 1846–1885.

[58] Z. Yue, S.E. Moulton, M. Cook, S. O’Leary, G.G. Wallace,”Controlled delivery for neuro-bionic devices”, *Adv Drug Delivery Rev.*, 2013, **65(4)**, 559-569.

[59] R.A. Green, R.T. Hassarati, J.A. Goding, S. Baek, N.H. Lovell, P.J. Martens, L.A. Poole-Warren, ”Conductive hydrogels: mechanically robust hybrids for use as biomaterials“, *Macromol Biosci.*, 2012, **12(4)**, 494-501.

[60] S.H. Ranganath, C.H. Wang, “Biodegradable microfiber implants delivering paclitaxel for post-surgical chemotherapy against malignant glioma”, *Biomaterials* 2008, **29**, 2996–3003.

[61] M.R. Abidian, D.H. Kim, D.C. Martin, "Conducting-polymer nanotubes for controlled drug release", *Adv Mater.*, 2006, **18(4)**, 405-409.

[62] S. Pillay, V. Pillay, Y.E. Choonara, D. Naidoo, R.A. Khan, L.C. du Toit, V.M. Ndesendo, G. Modi, M.P. Danckwerts, S.E. Iyuke, "Design, biometric simulation and optimization of a nano-enabled scaffold device for enhanced delivery of dopamine to the brain", *Int. J. Pharm.*, 2009, **382**, 277–290.

[63] N. Qi, X. Tang, X. Lin, P. Gu, C. Cai, H. Xu, H. He, Y. Zhang, "Sterilization stability of vesicular phospholipid gels loaded with cytarabine for brain implant*", Int. J. Pharm.*, 2012, **427**, 234–241.

[64] G.Z. Jin, M. Kim, U.S. Shin, H.W. Kim, "Neurite outgrowt.h of dorsal root ganglia neurons is enhanced on aligned nanofibrous biopolymer scaffold with carbon nanotube Coating", *Neurosci. Lett.*, 2011, **501**, 10–14.

[65] H. Zhou, X. Cheng, L. Rao, T. Li, Y.Y. Duan, "Poly 3,4 ethylenedioxythiophene/ multiwall carbon nanotube composite coatings for improving the stability of microelectrodes in neural prostheses applications, *Acta Biomater.* , 2013, **9**, 6439–6449.

[66] E. Che, X. Zheng, C. Sun, D. Chang, T. Jiang, S. Wang, "Drug nanocrystals: a state of art formulation strategy for preparing the poorly water-soluble drugs", *Asian J. Pharm. Sci.*, 2012, **7(2)**, 85-95.

[67] L. Zhang, J.J. Abbott, L. Dong, B.E. Kratochvil, D. Bell, B.J. Nelson, "Artificial bacterial flagella: fabrication and magnetic control", *Appl. Phys. Lett.*, 2009, **94**, 064107.

[68] A.S. Hoffman, "The origins and evolution of "controlled" drug delivery systems*", J. Control. Release*, 2008, **132**, 153–163.

[69] K.J. Hendricks, D. Lane, T.A. Burd, K.J. Lowry, D. Day, J.G. Phaup, J. Anglen, "Elution characteristics of tobramycin from polycaprolactone in a rabbit model", *Clin. Orthop. Relat. Res.*, 2001, **392**, 418–426.

[70] S. Rossi, A.O. Azghani, A. Omri, “Antimicrobial efficacy of a new antibiotic-loaded poly hydroxybutyric-co-hydroxyvaleric acid controlled release system*”, J. Antimicrob. Chemother.*, 2004, **54 (6)**, 1013–1018.

[71] P. Prabu, N. Dharmaraj, S. Aryal, B.M. Lee, V. Ramesh, H.Y. Kim, “Preparation and drug release activity of scaffolds containing collagen and poly caprolactone*”, J. Biomed. Mater. Res. A*, 2006, **79(1)**, 153–158.

[72] S. Aoyagi, H. Onishi, Y. Machida, “Novel chitosan wound dressing loaded with minocycline for the treatment of severe burn wounds”, *Int. J. Pharm.*, 2007, **330(1–2)**, 138–145.

[73] F.Y. Chiu, C.M. Chen, J. Lin Chien-Fu, W.H. Lo, “Cefuroxime impregnated cement in primary total knee arthroplasty: a prospective, randomized study of three hundred and forty knees”, *J Bone Joint Surg Am.*, 2002, **84-A(5)**, 759–62.

[74] R.C. Eberhart, S.H. Su, T.N. Kytai, M. Zilberman, T. Liping, “Bioresorbable polymeric stents: current status and future promise”, *J. Biomater. Sci. Polym. Ed.*, 2003, **14(4)**, 299–312.

[75] J.A. Planell, S.M. Best, D. Lacroix, A. Merolli, “Bone Repair Biomaterials”, *Woodhead Publishing Limited, CRC Press LLC., Cambridge, UK*, 2009.

[76] B.J. Nelson, L. Dong, F. Arai, “Micro/nanorobots”, *Springer Handbook of Robotics*, 2008, 411–450.

[77] S. Kim, F. Qiu, S. Kim, A. Ghanbari, C. Moon, L. Zhang, B.J. Nelson, H. Choi, “Fabrication and characterization of magnetic microrobots for three-dimensional cell culture and targeted transportation”, *Adv. Mater.*, 2013, **25**, 5863–5868.

[78] B.J. Nelson, I.K. Kaliakatsos, J.J. Abbott, “Microrobots for minimally invasivemedicine”, *Annu. Rev. Biomed. Eng.*, 2010, **12**, 55–85.

[79] J.H. Shin, H.Y. Song, T.S. Seo, S.H. Yuk, Y.H. Kim, Y.M. Cho, G.B. Choi, T.H. Kim, J.Y. Suh, “Influence of a dexamethasone-eluting covered stent on tissue reaction: an experimental study in a canine bronchial model”, *Eur. Radiol.*, 2005, **15**, 1241–1249.

[80] C. Indolfi, A. Mongiardo, A. Curcio, D. Torella, “Molecular mechanisms of in-stent restenosis and approach to therapy with eluting stents”, *Trends Cardiovasc Med ,*2003, **13(4)**, 142–8.

[81] M. Yaszemski, D. Trantolo, K.U. Lewandrowski, V. Hasirci, D. Altobelli, D. Wise, “Tissue engineering and novel delivery systems”, *New York: Marcel Dekker,* 2004.

[82] J. Kohn, R. Langer, “Bioresorbable and bioerodible materials. In Biomaterials Science—An Introduction to Materials in Medicine”, *New York*, 2000, 64–73.

[83] E.W. Keefer, B.R. Botterman, M.I. Romero, A.F. Rossi, G.W. Gross, “Carbon nanotube coating improves neuronal recordings”, *Nat. Nanotechnol.*, 2008, **3**, 434–439.

[84] K. Wang, H.A. Fishman, H.J. Dai, J.S. Harris, “Neural stimulation with a carbon nanotube microelectrode array”, *Nano Lett.*, 2006, **6**, 2043–2048.

[85] M.H. Bolin, K. Svennersten, X. Wang, I.S. Chronakis, A. Richter-Dahlfors, E.W.H. Jager, M. Berggren, “Nano-fiber scaffold electrodes based on PEDOT for cell stimulation”, *Sensors Actuators B Chem.*, 2009, **142**, 451–456

[86] R. Garimella, A.E. Eltorai, “Nanotechnology in orthopedics”, *Journal of Orthopaedics*, 2016, **14(1)**, 30–33.

[87] J. Ricci, H. Alexander, P. Nadkarni, M. Hawkins, J. Turner, “Biological mechanisms of calcium sulfate replacement by bone”, *Davies JE, editor. Bone engineering. Toronto, Canada: EM Squared Incorporated*, 2000, 332–44.

[88] Y. Huang, H. C. A. Ng, X. W. Ng, V. Subbu, “Drug-eluting biostable and erodible stents”, *J. Control. Release,* 2014, **193**, 188–201.

[89] P.F.G. Cardoso, G.I. Snell, P. Hopkins, G.W. Sybrecht, G. Stamatis, A.W. Ng, P. Eng, "Clinical application of airway bypass with paclitaxel-eluting stents: Early results", *J. Thorac. Cardiovasc. Surg.*, 2007, **134**, 974-981.

[90] L.E. Fisher, A. L. Hook, W. Ashraf, A. Yousef, D.A. Barrett, D.J. Scurr, X. Chen, E.F. Smith, M. Fay, C.D.J. Parmenter, R. Parkinson, R. Bayston, "Biomaterial modification of urinary catheters with antimicrobials to give long-term broadspectrum antibiofilm activity", *J. Control. Release*, 2015, **202**, 57–64.

Objective and Methodology

The main objective of this doctoral thesis is to study biodegradable polymers loaded with biologically active molecules for potential applications in biomedicine. Bearing this in mind, the materials required to create drug eluting devices must present a stable phase behavior that can only be achieved by forming consistent amorphous solid dispersions, i.e., miscible blends with strong intermolecular interactions. Moreover, when a drug is dispersed in amorphous form within a polymeric matrix its solubility increases and in turn, the bioavailability.

It is known that when two materials are miscible, macroscopic properties of single-phase materials are expected for the blend, such a single glass transition temperature intermediate between those of the pure components. In this context, they were mixed by solvent-casting, on one hand, an amorphous biopolymer (poly(D,L)-lactide, PDLLA), and on the other, a semicrystalline one (poly(ε-caprolactone), PCL), with a selection of molecules that kill or inhibit the growth of microbes, attending to their pharmacological application, solubility and affinity with the biodegradable polymers used in this work (see Table 1). At this point, thermal analyses were conducted on a Differential Scanning Calorimetry (DSC) in order to study the glass transition temperatures, and therefore, predict the miscibility between the two species. Once this preliminary study was completed, a few polymer-drug systems were selected for further analysis. In fact, miscibility was only investigated in blends with the biodegradable polymer PCL.

With the aim of inferring the release behavior, as well as the antibacterial efficacy of these materials based on the union of a biodegradable polymer with a biologically active molecule, physicochemical characterization and drug release studies were performed. For this purpose, in this thesis it will be necessary to study the:

- Miscibility and interactions between the PCL and the drug.
- Influence of the composition in the miscibility through the analysis of interaction parameters, as well as the crystallinity.
- Release profiles in PBS medium (in-vitro) for different compositions of the blend.
- Antibacterial activity of the PCL-drug system against *E.coli*.
- Biofilm formation of PCL coated with a fluorinated tripeptide with non-sticky feature.

Table 1. Miscibility prediction of the different polymer-drug systems.

Biologically active molecules	**Poly(ε-caprolactone) PCL**	**Poly(DL-lactide) PDLLA**
ERYTHROMYCIN	✗	✗
THIAMPHENICOL	✗	✗
TETRACYCLINE	✗	✗
SULFANILAMIDE	✗	✗
SULFACETAMIDE	✗	✗
SULFACHLOROPYRIDAZINE	✗	✗
SULFAMETHAZINE	✗	✗
TRIMETHOPRIM	✗	✗
LEVOFLOXACINE	✗	✗
BRONIDOX	✗	✓
THYMOL	✓	✗
CICLOHEXIMIDE	✗	✗
CHLORAMPHENICOL	✓	✗
NARINGIN	✗	✗
QUERCITIN	✓	✗
MYCOPHENOLIC ACID	✓	✗
HYGROMYCIN	✗	✗
TOBRAMYCIN	✗	✗
RAMOPLANIN	✗	✗

Chapter 1

Antimicrobial Poly(ε-caprolactone)/Thymol Blends: Phase Behavior, Interactions and Drug Release Kinetics

Summary

Blends of poly(ε-caprolactone) (PCL) and thymol (THY) have been prepared by melt-mixing to obtain biodegradable materials with antibacterial properties. Miscibility and specific interactions have been investigated by means of DSC and FTIR, and the drug release kinetics of the PCL/THY blends have been analyzed using UV spectroscopy at 274 nm. The melting points of PCL and THY have been analyzed using melting point depression analysis, and the interaction energy density has been found to vary from B = -30 J/cm^3 in THY-rich blends to B = 9 J/cm^3 in PCL-rich blends. The former value indicates a thermodynamically miscible blend, but the latter is close to critical conditions, and the dependence of B on composition has been discussed. The study of the carbonyl and hydroxyl stretching regions of the FTIR spectra for different compositions of the blend reveals strong -C=O···H-O- hydrogen bonding interactions, supporting the miscibility of the PCL/THY blends. Finally, the analysis of the release kinetics of THY from the PCL/THY blends in phosphate buffered saline (PBS) solution at 37 ºC (pH 7.4) shows that diffusion through the swelled polymeric chains is the leading mechanism for drug release.

1.1. Introduction

The use of biopolymers for biomedical applications makes feasible smart therapies, designed for the need of each patient. In most of the conventional drug release systems, the level of the pharmaceutical compound reaches a maximum and then falls down, requiring another dose of drug. Besides, the concentration of the drug could be above the toxicity level, or below the minimum effective concentration, causing periods of toxicity and inefficiency. However, if the drug is incorporated into a polymeric matrix, it can be released in a controlled way within the therapeutic margins [1]. Furthermore, if it is a biodegradable polymer, it can be reabsorbed or excreted by the body. Consequently, medical devices loaded with drugs made of biopolymers do not need to be taken off after finishing their service.

When formulating new drug molecules, low aqueous solubility is a common problem. In fact, more than 50 % of new molecules have delivery problems [1,2]. If a poorly water-soluble drug is orally administered, it can remain undissolved in the gastrointestinal tract until excretion, instead of being absorbed by the organism. The formulation of amorphous solid dispersions (ASDs) is a strategy to increase the solubility [3]. Amorphous polymers form a network like structure, due to molecular entanglement. When an amorphous drug is incorporated into this network, drug molecules can interact with polymer chains by weak physical bonds such as hydrogen bonding, Van de Waals force and/or ionic interactions. Consequently, there is a reduction of the molecular mobility since polymer chains act as crystallization inhibitors preserving the drug in its amorphous form [4,5]. The amorphous drug shows enhanced miscibility in any medium (including the physiological medium) since molecular miscibility is not constrained by the strong auto-association interactions commonly encountered in drugs in their crystalline forms.

ASDs can be formulated both inside the miscible and the metastable regions of the polymer/drug phase diagrams, but the miscible region is safer for the long term stability of the formulation. For miscibility to occur in a polymer/drug system, the free energy of mixing must be negative ($\Delta G_M \leq 0$). According to the classical Flory-Huggins theory ΔG_M can be calculated from Eq. 1 [6-8]:

$$\frac{\Delta G_M}{kT} = \underbrace{n_{drug}\, ln\phi_{drug} + n_{polymer}\, ln\phi_{polymer}}_{\substack{entropic \\ contributbn}} + \underbrace{n_{drug}\phi_{polymer}\chi}_{\substack{enthalpic \\ contributbn}} \tag{1}$$

where n is the number of molecules, ϕ is the volume fraction, χ is the Flory-Huggins interaction parameter, k is the Boltzmann constant, and T is the absolute temperature. The quantity χkT represents the difference in energy of a "solvent" molecule (i.e., the drug) immersed in the pure polymer ($\phi_{pol} \approx 1$) compared with one surrounded by molecules of its own kind, i.e., in the pure solvent [6]. Similarly, χkT can also be defined inverting the roles of solvent and polymer, where a different χkT value would indicate the dependence of χ on composition (instead of being a constant parameter). In a polymer-drug system the *entropic contribution* to the free energy of mixing of the blend is negative (favorable to miscibility) but small [6-8]. As a result, the *enthalpic contribution* $(n_{drug}\phi_{polymer}\chi)$ determines the miscibility of the system in most cases. In this way, a negative interaction parameter ($\chi < 0$) implies favorable interactions between the two species, yielding miscible systems, whereas a positive χ entails stronger cohesive interactions in the pure components than in the blend. According to the Flory-Huggins theory, the miscibility limit is given by the critical value of the interaction parameter ($\chi_c \sim 0.5$, for typical blends of high molecular weight polymers with low molecular weight species) [6-8]. In systems with slightly unfavorable interactions (those in which $0 < \chi < \chi_c$), miscibility is driven by the small but favorable entropic contribution.

Poly(ε-caprolactone) (PCL) is a semicrystalline polyester widely used in biomedical applications. Its degradation can last from several months to years, depending on the molecular weight, crystallinity and degradation conditions, making it suitable for long-term biomedical applications [9]. Thymol (THY) is a major component of thyme oil, an essential oil with antimicrobial properties. For example, it has antimicrobial activity against natural spoilage bacteria and food borne pathogens such as *Salmonella typhimurium*, *Escherichia coli*, *Listeria monocytogenes*, *Bacillus cereus*, and *Staphylococcus aureus* [10]. The chemical structures of the studied species support the possibility of hydrogen bonding between hydroxyl groups of thymol and carbonyl groups of PCL (see Fig. 1.1). Thymol can act as proton donor that forms hydrogen bonds with proton acceptor PCL [11,12].

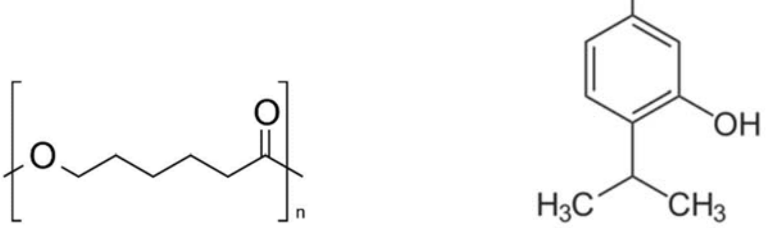

Poly ε-caprolactone)

Thymol

Figure 1.1. Schematic illustration of the chemical structures of PCL and Thymol.

The aim of this work is to study the miscibility and interactions between PCL and thymol, as well as to investigate the release mechanisms of the drug from the polymeric matrix. In a system composed of a swellable polymer, such as PCL, loaded with a drug, the release of the drug dispersed within the polymer matrix will be controlled by diffusion, swelling and erosion [13]. Miscibility of the PCL/THY blends has been studied using Differential Scanning Calorimetry (DSC), and the polymer-drug interaction parameter has been obtained through melting point depression analysis. Specific interactions in the PCL/THY system have been analyzed using Fourier Transform Infrared (FTIR) spectroscopy. Finally, the release kinetics of thymol from the PCL matrix has been investigated by means of Ultraviolet-Visible (UV-Vis) absorption spectroscopy.

1.2. Experimental Section

1.2.1. Starting Materials

Polycaprolactone (PURASORB® PC12 trade name) with an average molecular weight (M_W) of $1.3 \cdot 10^5$ g·mol^{-1} and $M_W/M_n = 1.76$ (as determined by GPC) was kindly supplied by Purac Biochem (The Netherlands). Thymol (purity ≥ 99.5 %) and phosphate buffered saline 0.1 M (pH 7.4) were obtained from Sigma-Aldrich (Spain).

1.2.2. Blend Preparation

Melt mixed blends (total sample amount 1 g) were prepared by melting together PCL and THY into small closed vessels to avoid the volatilization of the drug, immersed into a heated and stirred paraffin bath at 65 ºC during 24 h. Mechanical mixing was not employed because at this temperature THY is liquid and acts as an organic solvent. Afterwards, blends were allowed to cool for 24 h before measurements.

1.2.3. Differential Scanning Calorimetry (DSC)

Thermal analyses were conducted on a Modulated DSC Q200 from TA Instruments. Samples ranging from 5 to 10 mg were placed in aluminum pans, sealed, and scanned under a nitrogen atmosphere.

1.2.4. Melting Point Depression

The melting point depression of THY has been investigated in THY-rich blends containing 0-20 wt.% PCL. Samples were heated in the DSC with a scan rate of 1 ºC/min to obtain the melting temperature of the THY crystals.

The melting point depression of PCL has been investigated in PCL-rich blends containing 0-20 wt.% THY. Samples were first heated at 70 ºC for 3 min. to assure complete melting of the PCL crystals, and were then cooled at 10 ºC/min to the desired crystallization temperatures (T_c) and allowed to crystallize isothermally for 60 min. in the DSC furnace. Then, they were heated with a scan rate of 5 ºC/min to measure the melting temperature (T_m) of the PCL crystals. For a given composition, crystallizations were assumed complete if the melting endotherm deviated less than 10% from the maximum value, obtained usually for certain intermediate T_c.

Finally, no weight loss was observed during the thermal treatments (the DSC crucibles were weighed again after the calorimetric scans), indicating no significant THY evaporation.

1.2.5. Fourier Transform Infrared Spectroscopy (FTIR)

FTIR spectra of the blends were recorded on a Nicolet AVATAR 370 Fourier transform infrared spectrophotometer. Spectra were taken with a resolution of 2 cm^{-1} and were averaged over 64 scans in the range of 400-4000 cm^{-1}. Chloroform solutions containing 0.7 wt.% of blends were cast on KBr pellets by evaporation of the solvent at room temperature. The absorbance of the samples was within the range where the Lambert-Beer law is obeyed. To assure $CHCl_3$ removal without significant evaporation of THY, the presence of the former was followed *in situ* within the FTIR bench using the chloroform bands located at about 670 and 760 cm^{-1}. In most cases, these bands were undetectable after a few hours.

1.2.6. In Vitro Drug Release Kinetics (UV-Vis)

UV–Vis absorption spectra were recorded over wavelengths ranging from 190 to 500 nm using a Perkin Elmer Lambda 265 UV-Visible spectrophotometer. A calibration curve was obtained using THY solutions (in the 10 - 100 ppm range) in 0.1 M phosphate buffered saline (PBS) medium (pH 7.4). Absorbance values were measured at a wavelength of 274 nm (λ_{max} for THY) using a quartz cuvette.

Square samples (2 mm thick and 1 cm side length; approx. weight 145 mg) of the PCL/THY 70/30 blends obtained by melt mixing, were immersed in 100 mL of 0.1 M PBS solution at 37 ºC. At fixed time intervals, 2 mL of the solution were taken and replaced with fresh PBS at 37 ºC. Drug concentration in solution was determined by UV spectroscopy at a wavelength of 274 nm.

The kinetics of THY release from the square plates was determined by finding the best fit of the curves (% release against time) to different kinetic models [14-16]:

1. Zero order kinetics. This model holds in swelling-controlled drug release systems. Release process is controlled by relaxation of polymeric chains and the release rate of drug is constant and independent of its concentration (Eq. 2).

$$C_t/C_\infty = k_0 t \tag{2}$$

2. First order kinetics. Drug release rate depends on its concentration (Eq. 3).

$$\ln (1- C_t/C_\infty) = -k_1 t \tag{3}$$

3. Higuchi model [32]. Release is controlled by Fickian diffusion (Eq. 4).

$$C_t/C_\infty = k_h t^{1/2} \tag{4}$$

4. Korsmeyer-Peppas model. Fickian diffusional release Eq.(4) and non-Fickian relaxational release Eq.(2) are the limits of this model. When both mechanisms contribute additively to the release, the overall behavior can be approximated to Eq. 5:

$$C_t/C_\infty = kt^n \tag{5}$$

where $0.5 < n < 1$. The actual exponent also depends on the geometry of the releasing device. In addition, the case II transport contribution to the release also includes polymer disentanglement and erosion in this model. Finally, the exponent n should be determined using only the portion of the release curve where $C_t/C_\infty < 0.6$.

5. Peppas-Sahlin model. This approach couples the effects of Fickian diffusion ($k_I t^m$) and chain relaxation (k_{II}^{2m}) by means of Eq. 6:

$$C_t/C_\infty = k_I t^m + k_{II} t^{2m} \tag{6}$$

In all these models, C_t is the cumulative amount of drug released at time t, C_∞ represents the starting amount of drug, n and m are release exponents; and k, k_0, k_1, k_h, k_I and k_{II} are constants.

1.3. Results and Discussion

1.3.1. DSC Analysis

Miscibility of polymer-drug systems can be studied trough the depression of the melting point (T_m). Morphologically, in miscible blends, the amorphous drug enters into the interlamellar region of the semicrystalline polymer, hence lamellae become thinner and T_m decreases [17]. Thermodynamically, the chemical potential of the amorphous phase decreases when a miscible drug is added, due to both entropic and enthalpic effects [6-8], whereas the chemical potential of the crystalline part does not vary. As a consequence, the equilibrium between the crystalline and the amorphous part of the polymer is established at lower temperatures. For a system lacking attractive specific interactions, the reduction in chemical potential is related to the stabilization of the system associated to the entropy of mixing [6-8]. Using basic thermodynamics, since the change in free energy at the melting point equals zero ($\Delta G = 0$), the equation $\Delta G = \Delta H - T_m\Delta S = 0$ can be solved to $T_m = \Delta H/\Delta S$. In the case of a blend, the entropic contribution is larger (it is the sum of the entropy of melting plus the entropy of mixing), and consequently the melting temperature decreases relative to that of the pure polymer.

Figure 1.2 shows the first DSC traces (20 ºC/min) obtained for the pure components and for different PCL/THY blends. Pure PCL is a semicrystalline polymer displaying a glass transition temperature located at about -60 ºC and a melting endotherm at about 65 ºC. In turn, pure THY only shows a melting endotherm located at about 55 ºC. The absence of a glass transition temperature jump can be attributed to the lack of amorphous fraction at the temperatures expected for this transition, since the crystallization of this drug at sufficiently low temperatures is hard to avoid. The addition of THY to PCL shifts the melting temperature of PCL to lower temperatures, and when the THY content reaches 40 wt.%, the melting peak of PCL is no longer observed. Both the drop in melting temperature and the suppression of the melting peak suggest the miscibility of the system. Nevertheless, the most widely accepted criterion to establish the miscibility of polymer/drug systems is based on the behavior of the glass transition temperature [18-21]. Miscible blends should show a single glass transition temperature located at intermediate temperatures between those of the pure components. If the drug does not show as a glass transition temperature jump (as in the case of THY), the T_g of the blends should shift from the location corresponding to the pure polymer to the vitrification temperature of the drug, that can be estimated using the empirical Beaman-Boyer rule: $T_g/T_m = 2/3$ [18]. Unfortunately, the T_g estimated for THY according to this rule is about -55 ºC, very close to that of PCL, and hence, no significative T_g-shift can be expected for the PCL/THY system regardless of its phase behavior. As can be seen in Figure 1.2., all the blends investigated in this paper show single T_gs located in a narrow temperature range (about -55 ºC), and the DSC results are not conclusive regarding the miscibility of the system. However, other evidences obtained in this work and discussed throughout this paper indicate that the glass transition temperature jumps observed in Figure 1.2. should be attributed to single miscible phases rather than to PCL-rich phases.

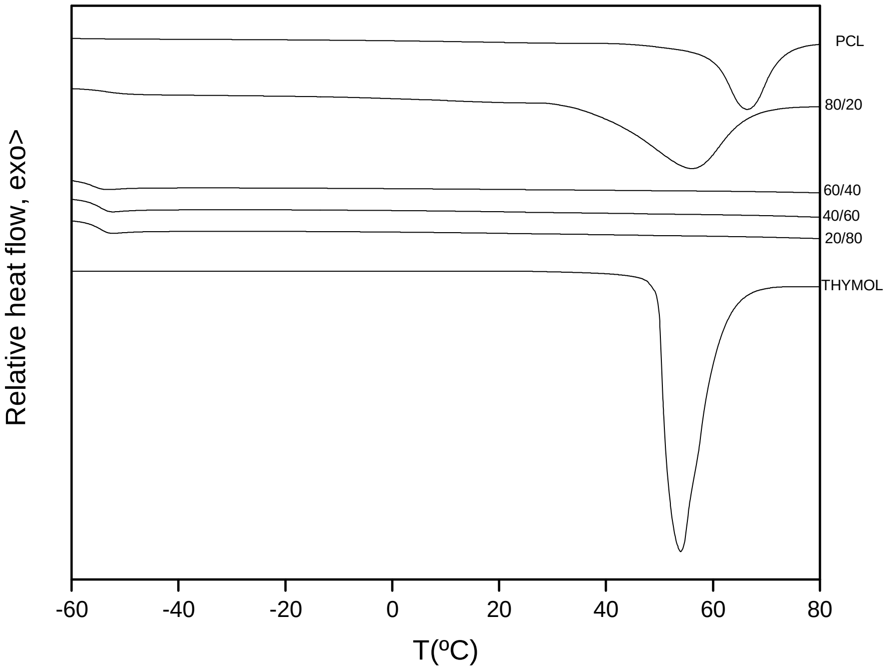

Figure 1.2. First scan DSC curves for PCL, thymol and PCL/THY blends.

1.3.2. Melting Point Depression Analysis.

Melting Point of Thymol.

The depression of the equilibrium melting point can be analyzed using the Flory-Huggins theory [6]. The general expression for blends of two polymeric species is:

$$\frac{1}{T_{me}} - \frac{1}{T_{me}^{0}} = \frac{-R}{\Delta H_{2u}} \frac{V_{2u}}{V_{1u}} \left(\frac{\ln \phi_2}{m_2} + \left(\frac{1}{m_2} - \frac{1}{m_1} \right) \phi_1 + \chi_{12} \phi_1^2 \right) \tag{7}$$

where T_{me}^0 and T_{me} are, respectively, the equilibrium melting points of the pure crystallizable component and of its blends, the subscripts *1* and *2* refer to the amorphous and crystallizable components respectively, *R* is the universal gas constant, ΔH_u is the heat of fusion per mole of crystalline repeat units, V_u is the molar volume of the repeating unit, *m* is the degree of polymerization, ϕ is the volume fraction, and χ_{12} is the polymer-polymer interaction parameter.

To apply Eq. (7) to the analysis of the melting point depression of THY (component 2), the molar volume of the lattice sites can be taken as the molar volume of liquid THY (V_2 = 158 cm^3/mol, according to the density of liquid THY at room temperature, ρ = 0.95 g/cm^3) [22], and consequently, $m_2 = 1$. In addition, the same volume can be adopted as the molar volume of the polymeric repeat unit ($V_2 = V_{1u}$) so that $1/m_1 \approx 0$ (since $m_1 = V_{pol}/V_{1u}$ is large). Therefore, Eq. (7) simplifies to Eq. (8):

$$\frac{1}{T_m} - \frac{1}{T_m^0} = \frac{-R}{\Delta H_2}\left(ln\phi_2 + \phi_1 + \chi\phi_1^2\right) \tag{8}$$

The first two terms in the right hand side of Eq. (8) represent the entropic contribution to ΔT_m, and the third term the enthalpic contribution. Applying the Taylor series expansion, $\ln\phi_2 = \ln(1-\phi_1) = -\phi_1 - \phi_1^2/2 - \phi_1^3/3$.... and assuming dilute conditions (i.e. neglecting cubic and higher order terms), the bracketed term in Eq. 8 simplifies to $(-1/2 + \chi)\phi_1^2$. Thus, both entropic and enthalpic factors contribute to the melting point depression in the whole composition range (none of them can be neglected even in diluted conditions). Substituting typical numbers in Eq. 8, it is easy to show that the entropic term only accounts for a small depression (usually about 1-2 ºC) [23].

The melting point of THY has been measured at low heating rates (1 ºC/min) for the pure component and for different PCL/THY blends (see Table 1.1). The average melting point of pure Thymol is $T_m^o(THY) = 49.6$ ºC, and the addition of 20 wt.% PCL decreases the melting point by about 4 ºC, suggesting the miscibility of the system. Using the melting temperature of pure THY and its melting enthalpy ($\Delta H_{THY} = 116$ J/g) [24], the data in Table 1.1 have been analyzed according to Eq. (8) yielding the plot in Figure 1.3. As can be seen (Fig. 1.3), the experimental data fit a line passing close to the origin, suggesting that the interaction parameter is almost independent of concentration [23]. The negative value obtained for χ (-1.8) confirms a thermodynamically miscible blend. Alternatively, the interaction energy density, B can be calculated at the melting temperature of THY according to Eq. (9):

$$\chi = \frac{BV_r}{RT} \tag{9}$$

where Vr is a reference volume (in this case, $V_r = V_2 = 158$ cm^3/mol), yielding B = - 30 J/cm^3.

Table 1.1. Melting temperature of THY in blends with PCL.

Thymol wt.. %	T_m^{mix} (ºC)		
	Sample 1	Sample 2	Sample 3
100	49.7	49.4	49.6
95.1	49.1	49.3	49.4
90.5	49.1	49.1	49.3
85.5	48.2	47.9	48.3
80.3	45.5	46.3	46.1

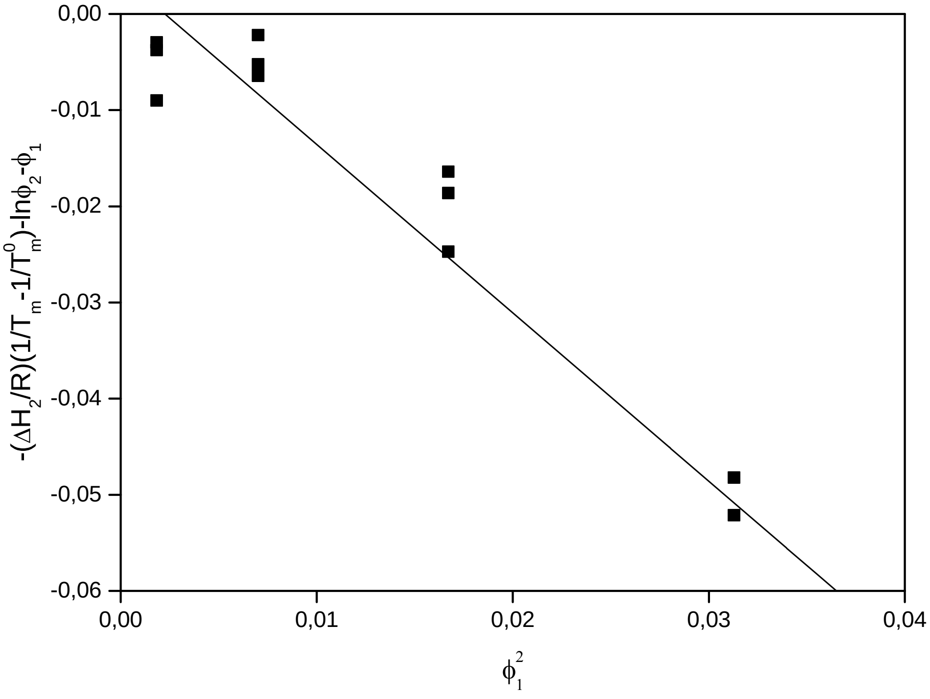

Figure 1.3. Analysis of the melting temperature of THY according to Eq. (8) for the PCL/THY system. The slope of the plot gives the interaction parameter χ = -1.8.

Melting Point of PCL

The depression of the equilibrium melting point of PCL can be analyzed again using the Flory-Huggins theory (Eq. 7). Following the same conventions as before, the subscripts *1* and *2* are assigned to the amorphous and crystallizable components respectively. In addition, the molar volume of the amorphous component (THY) is adopted as the molar volume of the lattice cells, yielding Eq. 10:

$$\frac{1}{T_{me}}-\frac{1}{T_{me}^{0}}=\frac{-R}{\Delta H_{2u}}\frac{V_{2u}}{V_{1}}\left(-\phi_{1}+\chi\phi_{1}^{2}\right) \tag{10}$$

The first and second terms in the right hand side of Eq. (10) represent, respectively, the entropic and enthalpic contributions to ΔT_m. As can be seen, the depression occurring in diluted conditions upon addition of a low molecular weight substance to a polymeric material is now governed by the entropic term. The enthalpic term only gains importance at higher concentrations. The larger relevance of the entropic term in this case (compared to Eq. 8) can be attributed to the larger entropy increase occurring when small molecules are added to big molecules. This can be rationalized from a statistical point of view considering that, if a polymeric chain of length *n* is replaced by *n* solvent molecules in a lattice, the system gains the combinatorial entropy corresponding to those *n* small molecules. In the opposite case, however, if *n* solvent molecules were replaced by a single polymer chain, the system would only gain the combinatorial entropy corresponding to the new chain (actually associated to the locations available for its center of mass) [6,25]. In the classical literature dealing with polymer-diluent systems it is preferred to rewrite Eq. 10 in terms of the interaction energy density, *B*, as follows (Eq. 11) [6,26-29]:

$$\left(\frac{1}{T_{me}}-\frac{1}{T_{me}^{0}}\right)\frac{1}{\phi_1}=\frac{R}{\Delta H_{2u}}\frac{V_{2u}}{V_1}\left(1-\frac{BV_1}{RT_{me}}\phi_1\right) \tag{11}$$

A plot of the left side of Eq. 11 as a function of ϕ_1/T_{me} allows calculating ΔH_{2u} from the intercept and B from the slope and the intercept. Eq. 11 requires, however, the determination of the equilibrium melting points, which is not a straightforward task in polymers, since their melting points decrease by both thermodynamic and morphological reasons [6,30]. The reference method to determine T_{me} is based on the Gibbs-Thomson (G–T) equation, which shows that plotting T_m vs l_c^{-1} (where l_c is the lamellar thickness) should result in straight line termed "melting line" [31,32]. Extrapolation of the melting line to $l_c^{-1} = 0$ eliminates the morphological effects rendering T_{me}. The G–T method is based on a correct thermodynamic relationship, but its application is not simple because requires the measurement of lamellar thicknesses by SAXS. An alternative method to obtain T_{me} is the Hoffman-Weeks (H–W) plot, which is actually based on the G–T equation and the surface nucleation theory [31]. In this procedure, samples are crystallized at different crystallization temperatures (T_c) and the corresponding melting temperatures (T_m) are subsequently measured. The plot of these points is assumed to follow a straight line, and T_{me} is obtained from the intersection of this line with the $T_m = T_c$ line. Recent investigations [31] have shown that the H–W method underestimates the equilibrium melting temperature of polymers. Nevertheless, because of its straightforward nature, the H–W extrapolation is by far the most widely used method in research papers dealing with polymer miscibility [21] and is therefore adopted in this work.

Figure 1.4. shows the melting peaks recorded for a PCL/THY 90/10 blend isothermally crystallized at different temperatures. As can be seen, a single crystallization peak can be observed for the samples crystallized at higher temperatures, but the melting endotherm splits progressively in two peaks with the decrease in crystallization temperature. A similar behavior was also reported for blends of PCL with Poly(vinylphenol) [11]. Double melting peak behavior is usually attributed to melting, recrystallization and subsequent remelting during the DSC scan [11,20]. Nowadays the occurrence of recrystallization or reordering processes during heating scans is widely accepted for both pure polymers and polymer blends. In cases were two melting components can be observed, the lower temperature contribution (LT_m) has been attributed to the initial crystals existing in the sample, while the higher melting point (HT_m), which is almost independent of the isothermal crystallization temperature, has been attributed to the crystals formed during the recrystallization process occurring after melting of the initial crystals[20]. Consequently, the LT_m melting points (obtained from the samples crystallized at lower temperatures) are recommended to perform the H-W extrapolations [20].

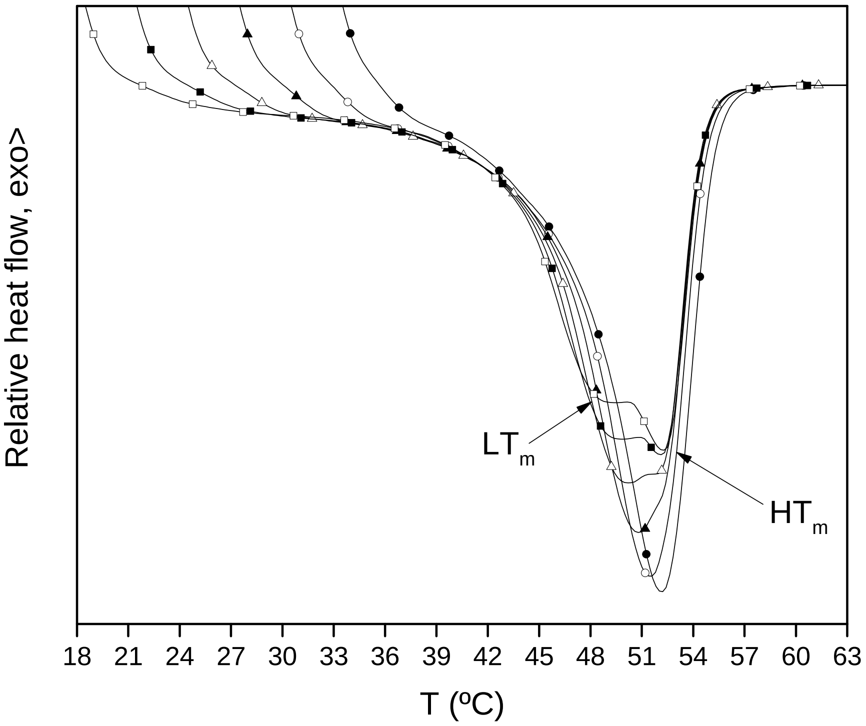

Figure 1.4. Melting endotherms obtained by DSC (5 ºC/min) for the PCL/THY 90/10 system crystallized at (●) 33, (○) 30, (▲) 27, (Δ) 24, (■) 21 and (□) 18 ºC. LT_m stands for Lower melting temperature and HT_m stands for Higher melting temperature (see text).

Unfortunately, the two peaks are strongly overlapped making impossible the H-W extrapolation based on LT_m. Even though the addition of THY seems to improve peak splitting, the two components are hardly distinguishable in pure PCL. The only alternative to perform reliable and consistent H-W extrapolations in this system is therefore using the melting peaks recorded for the samples crystallized at the highest temperatures, since they should be less affected by possible recrystallization processes occurring during the heating step. We have hence constrained the experimental data only to the four melting points obtained for the samples crystallized at the higher crystallization temperatures, covering a T_c range of only 9 ºC. Figure 1.5 shows the H-W extrapolations and Table 1.2 lists the T_{me} data obtained from the extrapolations. As can be seen in Table 1.2, the addition of 20 wt.% THY to PCL depresses the melting temperature of PCL by about 6 ºC, which is a relatively small depression compared to other polymer-diluent systems [6,25-29].

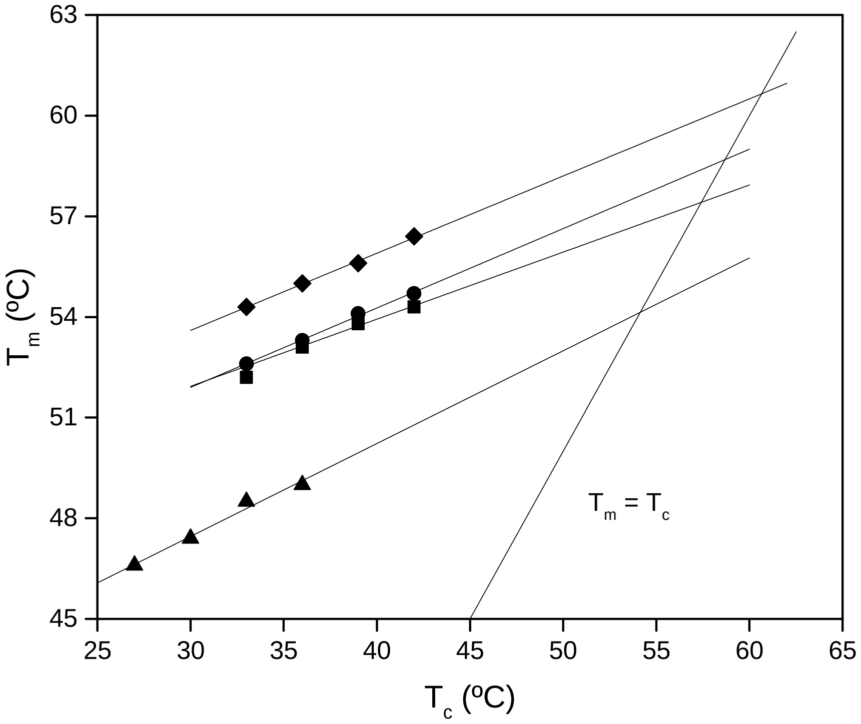

Figure 1.5. Hoffman-Weeks extrapolations for (•) PCL, (●) PCL/THY 95/5, (■) PCL/THY 90/10 and (▲) PCL/THY 80/20.

Table 1.2. Equilibrium melting points (T_{me}) obtained from the H-W extrapolations in Fig. 1.5.

System	T_{me} (ºC)
PCL	60.6
PCL/THY 95/5	58.7
PCL/THY 90/10	57.4
PCL/THY 80/20	54.1

Figure 1.6 shows the plot of $(1/T_m - 1/T_m^o)/\phi_1$ as a function of ϕ_1/T_m. The intercept leads to ΔH_{2u} = 163 J/g, which is located within the values accepted in the literature, ranging from 136 J/g to 167 J/g [33-35]. The slope leads to a positive value for the interaction energy density B ≈ 9 J/cm^3, indicating that autoassociation interactions are stronger than the interassociation contacts. In addition, the critical interaction energy density (B_{crit}) can be calculated from [7]:

$$B_{crit} = \frac{RT}{2}\left(\sqrt{\frac{\rho_1}{M_{w1}}} + \sqrt{\frac{\rho_2}{M_{w2}}}\right)^2 \tag{12}$$

resulting in B_{crit} ≈ 9 J/cm^3. Hence, the miscibility of the PCL-rich PCL/THY blends is close to critical conditions.

In summary, the interaction energy density in the PCL/THY system shows a strong dependence on composition, varying from about -30 J/cm^3 in THY-rich blends (indicating strong favorable interactions) to about 9 J/cm^3 in PCL-rich blends (indicating moderately unfavorable interactions). The dependence on composition resembles qualitatively that observed for blends of different polyesters with poly(vinyl phenol) (PVPh) [19, 36-38], although the interaction parameters obtained here for the PCL/THY system are shifted upward (to more positive values). Since THY is crystalline while PVPh is amorphous, the less favorable interaction parameters obtained for the blends with THY can be attributed to the higher autoassociation expected in pure crystalline THY compared to pure amorphous PVPh. In general, the stronger autoassociation of THY (compared to PVPh) is expected to hinder its miscibility with polyesters.

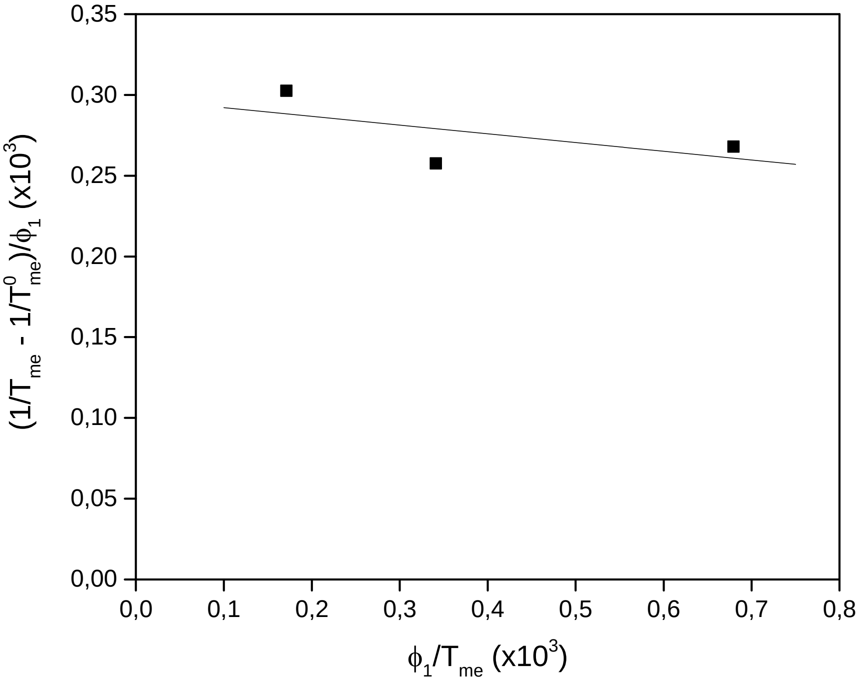

Figure 1.6. Analysis of the equilibrium melting temperature of PCL according to Eq. (11) for the PCL/THY system.

1.3.3. FTIR Analysis

Specific interactions present in PCL/THY blends can be investigated by infrared spectroscopy. The chemical structures of the studied species support the possibility of hydrogen bonding between the hydroxyl groups of thymol and the carbonyl groups of PCL [11,12].

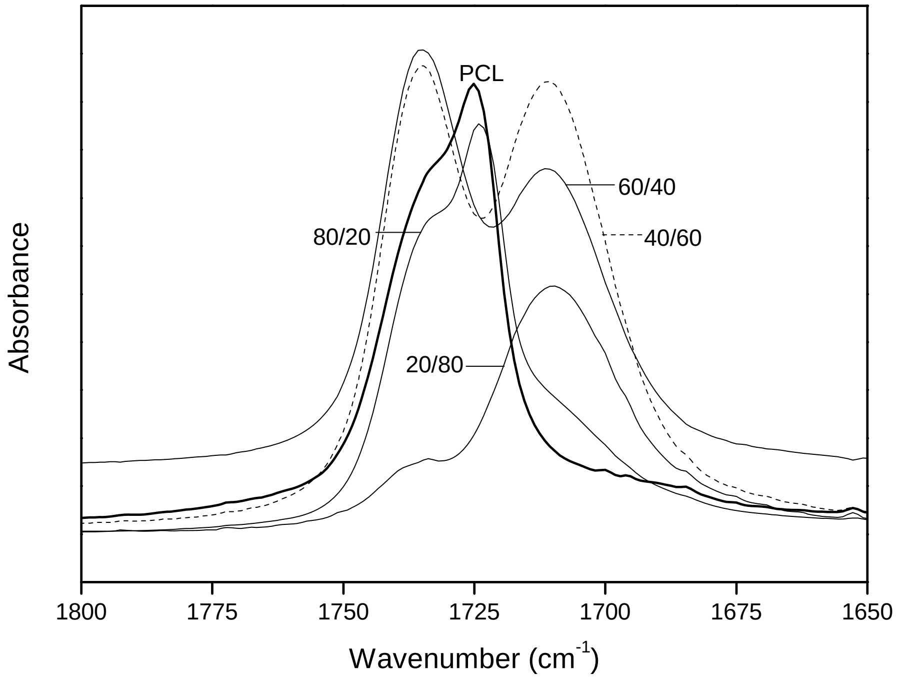

Figure 1.7. Carbonyl stretching region for pure PCL and PCL/THY blends of different composition.

Fig. 1.7 shows the carbonyl stretching region of PCL and PCL/THY blends of different compositions. The spectrum of pure PCL shows a peak at 1725 cm^{-1} attributable to the PCL crystals and a shoulder at 1735 cm^{-1} representing the amorphous phase [11]. The 80/20 composition shows again similar bands to those of pure PCL, but accompanied by a new contribution located at lower wavenumbers, attributable to hydrogen bonded C=O groups in PCL [39]. When 40 wt.% thymol is added to the blend, the band corresponding to crystalline PCL is not observed, and the spectrum only shows two bands located at about 1735 and 1710 cm^{-1}, attributable respectively to free and hydrogen bonded C=O groups in PCL [39]. Further addition of Thymol results in an increase of the relative intensity of the band located at 1710 cm^{-1} relative to the band located at 1735 cm^{-1}.

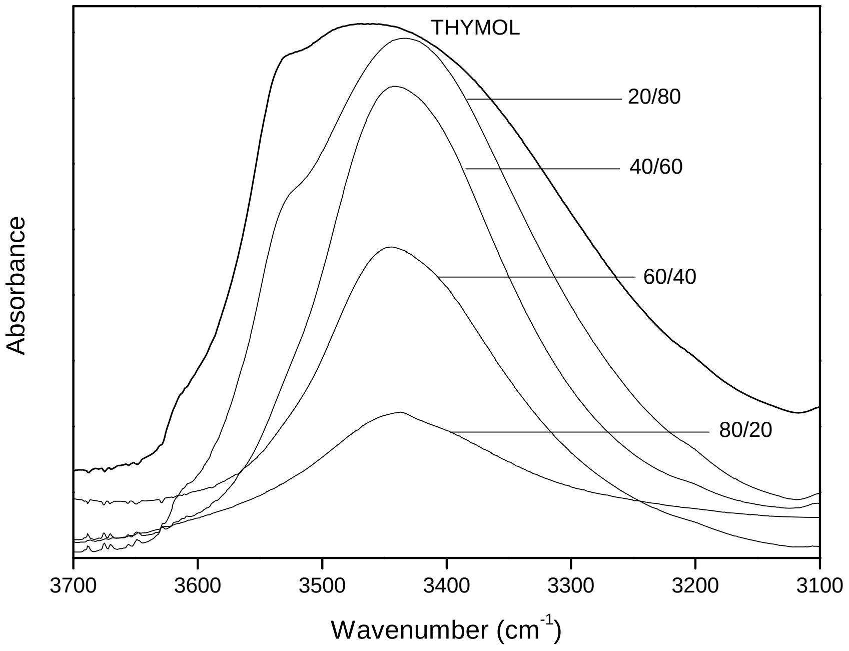

Figure 1.8. Hydroxyl stretching region for pure Thymol and PCL/THY blends of different compositions.

Fig. 1.8. displays the hydroxyl stretching region of PCL and PCL/THY blends. The spectrum of pure thymol shows a broad band centered at 3465 cm^{-1} attributable to a wide distribution of self-associated hydroxyl groups [40,41], as well as a shoulder at about 3525 cm^{-1}. This component has been attribute in the classical literature to free OH groups [40], however, according to recent investigations, it indeed corresponds to hydroxyl groups interacting with aromatic rings (OH···π interactions) [41-43]. Actually, free OH stretching band has been claimed to occur at about 3600 cm^{-1} [41-43], but is undetectable in the spectrum of pure THY. The PCL/THY 20/80 blend shows a peak located at about 3440 cm^{-1}, characteristic of hydroxyl groups associated with carbonyl groups of PCL (-C=O···H-O-) [11,39]. Consequently, the shoulder is weaker, indicating a decrease in the fraction of non-bonded hydroxyl groups. When the amount of thymol reaches 60 wt.%, the spectrum is governed by the sharp peak at 3440 cm^{-1}, while the shoulder at higher wavenumbers is no longer discerned, indicating that -C=O···H-O- interactions increase at the expense of hydroxyl-hydroxyl autoassociation and of OH···π interactions.

Finally, it is interesting to perform a quantitative study of the degree of interassociation and its dependence with composition. For this purpose, a least-squares curve-fitting analysis has been applied to the carbonyl stretching bands. The two bands corresponding to the contributions of free and associated carbonyls fit well to a Gaussian function. Table 1.3 lists the calculated results. The free carbonyl fraction, f_F, has been determined from [44]:

$$f_F = \frac{A_F}{A_F + A_A/a} \tag{13}$$

where A_F and A_A are the areas (absorbances) under the peaks corresponding to the free and associated carbonyl groups respectively, and *a* is the ratio of the molar absorption coefficients ($a = \varepsilon_A/\varepsilon_F$). A value of 1.5 has been taken for this ratio according to preceding studies [44]. Figure 1.9 shows the dependence of the interassociation with composition. As can be seen f_F increases smoothly with the addition of thymol. The calculated data suggest that the interassociation degree reaches a limiting value in THY-rich compositions, a limitation that is mainly attributed to intramolecular screening [45].

Table 1.3. Curve fitting results for the PCL/THY system.

PCL/THY wt.%	free C=O band			HB C=O band			f_F
	$\bar{\upsilon}$ (cm^{-1})	FWHH	Area	$\bar{\upsilon}$ (cm^{-1})	FWHH	Area	
60/40	1735.6	17.2	48.3	1710.7	25.0	51.7	0.58
40/60	1736.0	16.5	38.6	1710.6	25.6	61.4	0.49
20/80	1737.9	16.0	11.9	1709.4	25.8	88.1	0.17

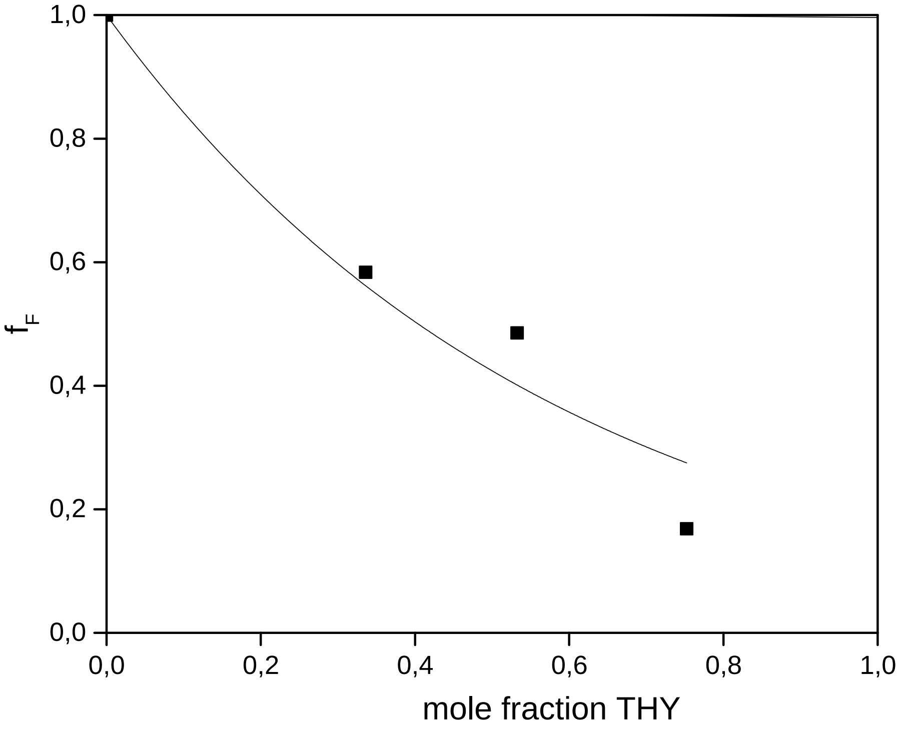

Figure 1.9. Dependence of the fraction of free C=O groups with composition.

1.3.4. In Vitro Drug Release

Figure 1.10. shows the in vitro release profile of THY from a PCL/THY 70/30 sample in 10 days (240 hours). In the first 2 hours no drug release is detected, but then THY release begins and 7 wt.% THY is released after 24 h. The highest release rate is achieved during the first day. Thereafter release rate slows down, and a sustained release of THY is observed during the following days. After a week (168 h), a 23 wt.% of drug is released. Afterwards, the release rate slows down and throughout the last days of the study just an additional 2 wt.% drug is released. Only a 25 wt.% of the THY contained into the polymeric matrix is released in 10 days. Stability of PCL is not affected after that period, since the in vitro degradation rate of PCL is $KM_W = 0.001$ days^{-1} [46]. Thus, the rest of the drug will not be quantitatively released until the beginning of bulk erosion.

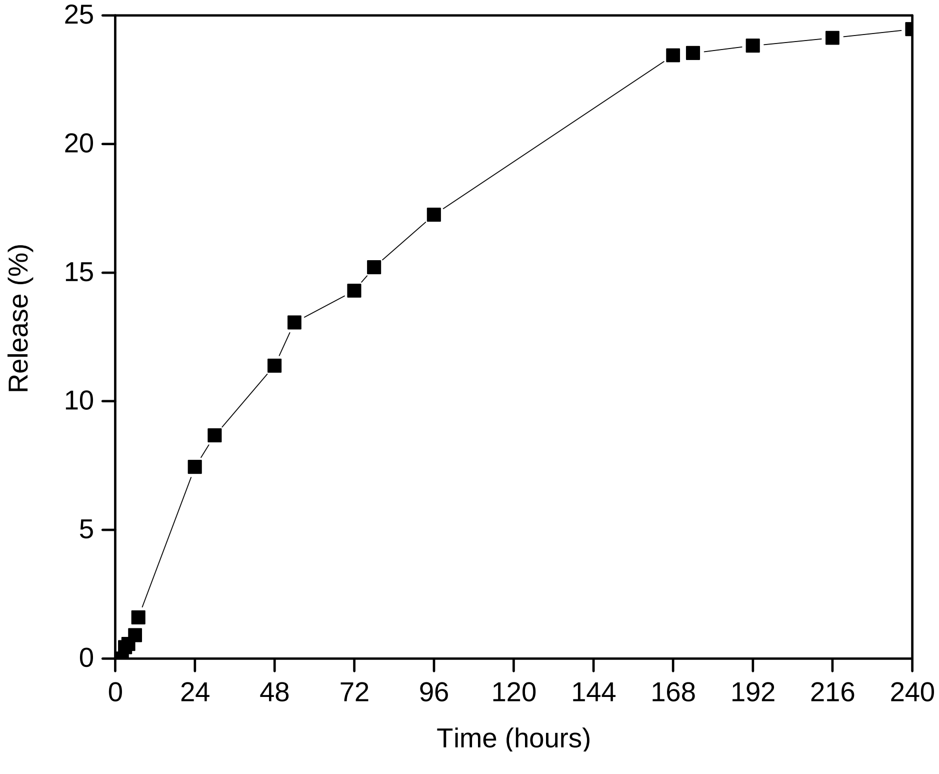

Figure 1.10. Drug release profile for a PCL/THY 70/30 sample (1 cm^2 x 2 mm) obtained by melt mixing and immersed into 100 mL of PBS at 37 ºC during 10 days.

The observed profile indicates that the first step is the penetration of the buffered solution into the matrix, leading to its swelling and, as a result, the free volume of the polymer increases. Temperature in the solution is 37 ºC which is above glass transition of the polymer ($T_{g\ PCL}$ = -60 º C), hence chains have a certain degree of mobility when they are immersed in the solution. The polymeric network becomes wider, and the amorphous THY dissolved in the polymer matrix diffuses throughout it to reach the outer solution. Thymol is only sparingly soluble in water (solubility is about 0.9 g/l) [47], and in our experimental setup, the concentration of THY in the outer solution should come close to 0.1 g/L after 7 days. Thus, considering the much larger solubility of THY in the polymeric matrix compared to the aqueous phase, the concentration plateau observed after a week is probably dictated by the partition coefficient of THY between the organic and the aqueous phases [48]. Entrapped remaining thymol should be released after the degradation of the polymer in several months.

Release data has been fitted to different kinetic equations used to study the mechanism of drug release. Results are shown in Table 1.4. The release exponent obtained from Korrmeyer-Peppas model is n = 0.931 (0.5 < n < 1) which indicates anomalous drug transport consisting on a combination of Fickian diffusion and polymer relaxation. The best fit has been obtained using the Peppas-Sahlin mathematical model. As can be seen in Table 1.4, the value obtained for k_I in the Peppas-Sahlin model is significantly bigger than k_{II}, therefore Fickian diffusion prevails over relaxation of polymeric chains.

Table 1.4. Fitting of the release data to the mathematical models for drug release kinetics. R^2 is the correlation coefficient, n is the release exponent, and k_I and k_{II} indicate the contribution to Fickian and relaxation mechanisms respectively.

Zero order	**First order**	**Higuchi**	**Korsmeyer-Peppas**	**Peppas-Sahlin**	
$R^2 = 0.8951$	$R^2 = 0.9153$	$R^2 = 0.9858$	$R^2 = 0.9492$	$R^2 = 0.9904$	
			n = 0.931	$k_I = 2.5\text{x}10^{-3}$	$k_{II} = -0.006\text{x}10^{-3}$

1.4. Conclusions

Miscibility and interactions have been investigated in the PCL/THY system. The analysis of the glass transition temperature by DSC is not conclusive regarding the miscibility behavior of the blends, but the melting points of both PCL and THY shift to lower temperatures when blended, indicating the miscibility of the system. According to the melting point depression analysis, the interaction energy density varies from B = -30 J/cm^3 in THY-rich blends to B = 9 J/cm^3 in PCL-rich blends. The dependence on composition can be rationalized considering that in the latter case a larger energy cost can be expected for the extraction of a THY molecule (compared to a PCL repeat unit) from the pure component, penalizing therefore the energy balance associated to the process of moving it to the diluted blend. Moreover, even though the chemical structure of THY is similar to that of Poly(vinylphenol) (PVPh), the interaction parameters obtained for THY are higher (more positive), probably due to a larger autoassociation degree in the crystalline molecule than in the amorphous polymer.

The specific interactions have been analyzed using FTIR spectroscopy. The analysis of the C=O stretching band of PCL and of the O-H stretching band of THY indicate strong -C=O···H-O- interactions. The location observed for the interassociated O-H stretching band (3440 cm^{-1}) indicates hydrogen bonds of similar strength to those reported for blends of PCL with other phenolic compounds [12]. The in vitro drug release studies indicate that, during the first stage, THY release from PCL is governed by diffusion through the swelled polymeric matrix. In our experimental setup, about 23 wt.% of the drug was released into the PBS solution during the first 7 days. Afterwards, THY reached equilibrium conditions between the organic and aqueous phases, according to its partition coefficient. In a physiological environment, however, such equilibrium conditions can be hardly expected since THY is metabolized by the organism and its concentration should be small, and consequently, its release should continue without reaching an asymptotic stage. Overall, THY is slowly released and can be used to build antimicrobial devices of long lasting action.

References

[1] S.B. Teja, S.P. Patil, G. Shete, S. Patel, A.K. Bansal, “Drug-excipient behavior in polymeric amorphous solid dispersions”, *J. Excipients Food Chem.*, 2013, **4(3)**, 70-94.

[2] P.J. Marsac, T. Li, L.S. Taylor, “Estimation of drug-polymer miscibility and solubility in amorphous solid dispersions using experimentally determined interaction parameters”, *Pharm. Res.*, 2008, **26(1)**, 139-151.

[3] T. Vasconcelos, B. Sarmento, P. Costa, “Solid dispersions as strategy to improve oral bioavailability of poor water soluble drugs”, *Drug Discovery Today*, 2007, **12(23)**, 1068-1075.

[4] H. Konno, T. Handa, D.E. Alonzo, L.S. Taylor, “Effect of polymer type on the dissolution profile of amorphous solid dispersions containing felodipine”, *Eur. J. Pharm. Biopharm.*, 2008, **70(2)**, 493-499.

[5] F. Meng, V. Dave, H. Chauhan, “Qualitative and quantitative methods to determine miscibility in amorphous drug–polymer systems”, *Eur. J. Pharm. Sci.*, 2015, **77**, 106–111.

[6] P.J. Flory, *Principles of Polymer Chemistry, Cornell University Press: Ithaca, New York*, 1953.

[7] G.D. Merfeld, D.R. Paul, "Polymer-Polymer Interactions Based on Mean-Field Approximations", *Polymer Blends, Vol 1: Formulation, D.R. Paul and C.B. Bucknal, Eds., Wiley, New York*, 2000, Chapter 3, 55-92.

[8] E. Meaurio, N. Hernandez-Montero, E. Zuza, J. R. Sarasua, "Miscible blends based on biodegradable polymers", *Characterization of Polymer Blends: Miscibility, Morphology and Interfaces, S. Thomas, Y. Grohens, P. Jyotishkuma Eds. Wiley: Weinheim*, 2014 , Vol. 1, Chapter 2, 7–92.

[9] M. Labet, W. Thielemans,”Synthesis of polycaprolactone: a review”, *Chem. Soc. Rev.*, 2009, **38**, 3484–3504.

[10] Y. Wu, Y. Qin, M. Yuan, L. Li, H. Chen, J. Cao, J. Yang , "Characterization of an antimicrobial poly(lactic acid) film prepared with poly(ε-caprolactone) and thymol for active packaging", *Polym. Adv. Technol.*, 2014, **25**, 948–954.

[11] E.G. Lezcano, C. Salom Coll, M.G. Prolongo, "Melting behaviour and miscibility of poly(ε-caprolactone) + poly(4-hydroxystyrene) blends", *Polymer*, 1996, **37(16)**, 3603-3609.

[12] S.W. Kuo, C.F. Huang, F.C. Chang. "Study of Hydrogen-Bonding Strength in Poly(ε-caprolactone) Blends by DSC and FTIR", *J. Polym. Sci.* B, 2001, **39**, 1348–1359.

[13] J.S. Boateng, K.H. Matthews, A.D. Auffret, M.J. Humphrey, H.N. Stevens, G.M. Eccleston, "In vitro drug release studies of polymeric freeze-dried wafers and solvent-cast films using paracetamol as a model soluble drug", *Int. J. Pharm.*, 2009, **378**, 66-72.

[14] S. Khan, H. Batchelor, P. Hanson , I.Y. Saleem, Y. Perrie, A.R. Mohammed, "Dissolution rate enhancement, in vitro evaluation and investigation of drug release kinetics of chloramphenicol and sulphamethoxazole solid dispersions", *Drug. Dev. Ind. Pharm.*, 2013, **39(5)**, 704-715.

[15] S. Kalita, B. Devi, R. Kandimalla, K.K. Sharma, A. Sharma, K. Kalita, A.C. Kataki, J. Kotoky, "Chloramphenicol encapsulated in poly-e-caprolactone-pluronic composite: nanoparticles for treatment of MRSA-infected burn wounds", *Int. J. Nanomed.*, 2015, **10**, 2971-2984.

[16] T. Higuchi, "Mechanism of sustained-action medication. Theoretical analysis of rate of release of solid drug dispersed in solid matrices", *J. Pharm. Sci.*, 1963, **52(12)**, 1145-1149.

[17] D. Rohindra, "Miscibility determination in poly(ε-caprolactone)/poly(vinil formal) blend by equilibrium melting temperature and spherulite morphology", *J. Macromol. Sci. B*, 2009, **48**, 1103-1113.

[18] R. Nair, N. Nyamweya, S. Gönen, L.J. Martínez-Miranda, S.W. Hoag, "Influence of various drugs on the glass transition temperature of poly(vinylpyrrolidone): a thermodynamic and spectroscopic investigation", *Int. J. Pharm.*, 2001, **225**, 83-96.

[19] E. Meaurio, E. Zuza, J.R. Sarasua, "Miscibility and specific interactions in blends of poly(L-lactide) with poly(vinylphenol)", *Macromolecules*, 2005, **38(4)**, 1207-1215.

[20] N. Hernandez-Montero, E. Meaurio, K. Elmiloudi, J.R. Sarasua, "Novel miscible blends of poly(p-dioxanone) with poly(vinyl phenol)", *Eur. Polym. J.*, 2012, **48**, 1455–1465.

[21] A. Lejardi, J.R. Sarasua, A. Etxeberria, E. Meaurio, "Miscible Blends of Poly(ethylene oxide) with Brush Copolymers of Poly(vinyl alcohol)-graft-poly(L-lactide)", *J. Polym. Sci. B*, 2016, **54**, 1217–1226.

[22] J. Timmermans, "Physico-chemical constants of pure organic compounds", *Elsevier, New York*, 1950.

[23] P.J. Marsac, S.L. Shamblin, L.S. Taylor, "Theoretical and Practical Approaches for Prediction of Drug-Polymer Miscibility and Solubility", *Pharm. Res.*, 2006, **23(10)**, 2417-2426.

[24] M.S. Manic, D. Villanueva, T. Fornari, A.J. Queimada, E.A. Macedo, V. Najdanovic–Visak, "Solubility of high-value compounds in ethyl lactate: measurements and modelling", *J. Chem. Thermodynamics*, 2012, **48**, 93–100.

[25] P.J. Flory, W.R. Krigbaum, "Thermodynamics of High Polymer Solutions" *Annu. Rev. Phys. Chem.*, 1951, **2**, 383–402.

[26] L. Mandelkern, "Crystallization of Polymers, 2nd ed.", *Cambridge University Press, New York*, 2002, Vol.1, Chapter 3.

[27] P.J. Flory, H.D. Bedon, E.H. Keefer, "Melting points and heats of fusion of some polyamides and polyesters", *J. Polym Sci A*, 1958, **28(116)**, 151–161.

[28] D.E. Roberts, L. Mandelkern, "Thermodynamics of Crystallization in High Polymers: Natural Rubber", *J. Am. Chem. Soc.*, 1955, **77(3)**, 781–786.

[29] G.B. Gechele, L. Crescentini, "Melting temperatures and polymer–solvent interaction for polycaprolactam", *J. Appl. Polym. Sci.*, 1963, **7(4)**, 1349–1357.

[30] T. Nishi, T.T. Wang, "Melting Point Depression and Kinetic Effects of Cooling on Crystallization in Poly(vinylidene fluoride)-Poly(methyl methacrylate) Mixtures", *Macromolecules*, 1975, **8**, 909–915.

[31] M. Al-Hussein, G. Strobl, "The Melting Line, the Crystallization Line, and the Equilibrium Melting Temperature of Isotactic Polystyrene", *Macromolecules*, 2002, **35**, 1672–1676.

[32] K. Yamada, M. Hikosaka, A. Toda, S. Yamazaki, K. Tagashira, "Equilibrium Melting Temperature of Isotactic Polypropylene with High Tacticity: 1. Determination by Differential Scanning Calorimetry", *Macromolecules* 2003, **36**, 4790–4801.

[33] V. Crescenzi, G. Manzini, G. Calzolari, C. Borri, "Thermodynamics of fusion of poly-β-propiolactone and poly-ε-caprolactone. Comparative analysis of the melting of aliphatic polylactone and polyester chains", *Eur. Polym. J.*, 1972, **8(3)**, 449-463.

[34] H.L. Chen, L.J. Li, T.L. Lin, "Formation of Segregation Morphology in Crystalline/Amorphous Polymer Blends: Molecular Weight Effect", *Macromolecules*, 1998, **31**, 2255-2264.

[35] Y. He, Y. Inoue, "Novel FTIR method for determining the crystallinity of poly(ε-caprolactone)", *Polym. Int.*, 2000, **49**, 623–626.

[36] E. Meaurio, E. Zuza, J.R. Sarasua, "Direct Measurement of the Enthalpy of Mixing in Miscible Blends of Poly(DL-lactide) with Poly(vinylphenol)", *Macromolecules*, 2005, **38**, 9221-9228

[37] E. Zuza, E. Meaurio, A. Etxeberria, J.R. Sarasua, "Exothermal Process in Miscible Polylactide/Poly(vinyl phenol) Blends: Mixing Enthalpy or Chemical Reaction?", *Macromol. Rapid Commun.*, 2006, **27**, 2026–2031.

[38] E. Zuza, A. Lejardi, E. Meaurio, J.R. Sarasua, "Phase behavior and interactions in poly(DL-lactide)/poly(styrene-co-vinylphenol) blends", *Eur. Polym. J.*, 2015, **63**, 58–66.

[39] E.J. Moskala, D.F. Varnell, M.M. Coleman, "Concerning the miscibility of poly vinyl phenol) blends – FTi.r. study", *Polymer*, 1985, **26(2)**, 228-234.

[40] D. Li, J. Brisson, "Hydrogen bonds in poly(methyl methacrylate)-poly(4-vinyl phenol) blends", *Polymer*, 1998, **39**, 793-800.

[41] A. Lejardi, E. Meaurio, J. Fernández, J.R. Sarasua, "Miscibility of Poly(vinyl alcohol)-graft-Hydroxy Ester/Poly(vinylpyrrolidone) Blends", *Macromolecules*, 2011, **44**, 7351–7363.

[42] A. Choperena, P. Painter, "Hydrogen Bonding in Polymers: Effect of Temperature on the OH Stretching Bands of Poly(vinylphenol)", *Macromolecules*, 2009, **42**, 6159–6165.

[43] L. Guo, H. Sato, T. Hashimoto, Y. Ozaki, "Thermally Induced Exchanges of Hydrogen Bonding Interactions and Their Effects on Phase Structures of Poly(3-hydroxybutyrate) and Poly(4-vinylphenol) Blends", *Macromolecules*, 2011, **44**, 2229–2239.

[44] M.M. Coleman, J.F. Graf, P.C. Painter, "Specific Interactions and the Miscibility of Polymer Blends", *Technomic Publishing, Lancaster, PA*, 1991.

[45] P.C. Painter, L.P. Berg, B. Veytsman, M.M. Coleman, "Intramolecular Screening in Nondilute Polymer Solutions", *Macromolecules*, 1997, **30**, 7529-7535.

[46] J. Fernández, A. Etxeberria, J.R. Sarasua, "In vitro degradation studies and mechanical behavior of poly(ε-caprolactone-co-δ-valerolactone) and poly(ε-caprolactone-co-L-lactide) with random and semi-alternating chain microstructures", *Eur. Polym J.*, 2015, **71**, 585-595.

[47] "Perry's Chemical Engineers' Handbook 7th Ed." *R.H. Perry, D.W. Green Eds. McGraw-Hill, New York*, 1997.

[48] J. Siepmann, N.A. Peppas , "Modeling of drug release from delivery systems based on hydroxypropyl methylcellulose (HPMC)", *Adv. Drug Delivery Reviews*, 2001, **48**, 139-157.

Chapter 2

Physicochemical Characterization and Drug Release Kinetics in Poly(ε-caprolactone)/Chloramphenicol Blends

Chapter 2.1.

The Conformation of Chloramphenicol in the Ordered and Disordered Phases

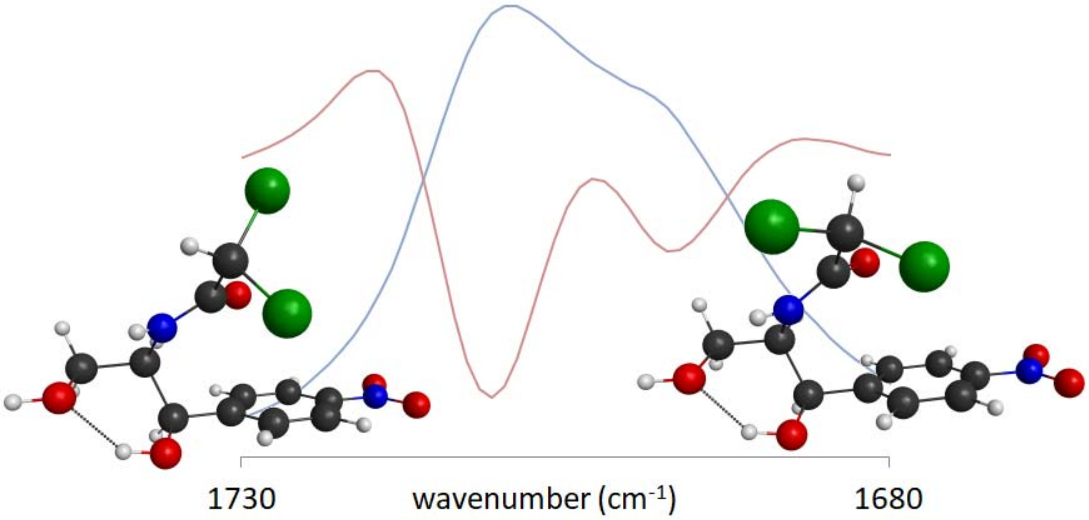

Summary

The conformational behavior of chloramphenicol (CAM) in the solid, liquid and vapor phases is established here by means of FTIR spectroscopy and modern QM methods, combined with reported experimental results. In the crystalline phase, the IR analysis discards the conformer proposed by Acharya et al. (*Acta Cryst.,* 1979, B35:1360-1363) and supports the one proposed by Chatterjee et al. (*J. Cryst. Mol. Struct.,* 1979, 9:295-304), characterised by an intramolecular O-H•••O hydrogen bond in which the primary hydroxyl group acts as hydrogen bond donor. The conformational behavior of CAM in the liquid and gas phases has been analyzed using QM calculations. The Onsager self-consistent reaction field (SCRF) model has been used for the geometry optimizations in solution. Releasing the CAM molecules from the intermolecular interactions occurring in the crystalline phase results in the reversal of the intramolecular O-H•••O hydrogen bond so that the secondary hydroxyl group acts as hydrogen bond donor. In addition, the dichloroacetamide group folds back further over the phenyl ring to form an intramolecular C-Cl•••π halogen bond. Two different halogen bonds are actually observed (each one with a different chlorine atom) resulting in two different stable conformers, that can be detected by FTIR spectroscopy due to the conformational sensitivity of the C=O group to the conformation of the dichloroacetyl group. Finally, the stability of the conformers with the polarity of the medium is also discussed.

2.1.1. Introduction

Chloramphenicol (CAM) is a broad-spectrum antibiotic isolated originally from *Streptomyces venezuelae* in 1947 [1, 2]. Its structure was soon elucidated, and it became the first antibiotic to be synthesized by chemical means [1, 2]. CAM acts essentially as a bacteriostatic agent, inhibiting bacterial synthesis by binding to the 50S subunit of 70S ribosomes [1]. A wide range of microorganisms can be effectively treated by CAM; for example, it is useful in the treatment of staphylococcal brain abscesses, meningitis caused by *Enterococcus faecium* or ocular infections caused by a number of bacteria including *Staphylococcus aureus*, *Streptococcus pneumoniae* and *Escherichia coli* [1, 2, 3]. CAM is currently included in List of Essential Medicines (EML) published by the World Health Organization (WHO) [4].

CAM contains different reactive groups that have been exploited to obtain derivatives (more than 500 compounds have been reported) and to explore structure-activity relationships [1, 2]. The molecule of CAM (Figure 2.1.1) can be divided in three parts: (I) a p-nitrobenzene moiety, (II) a dichloroacetyl moiety and (III) a 2-amino-propanediol moiety [1, 2]. The aromatic part (I) permits considerable variation, resulting in compounds whose bacterial activity is modified rather than suppressed. The acyl side chain (II) is essential for in vivo bacterial growt.h inhibition, where bulkier groups usually reduce antibacterial activity, but is less constraining for in vitro protein synthesis inhibition [2]. Therefore, it was concluded that the acyl side chain is important for the penetration of the antibiotic in the bacterial cell [1, 2]. Finally, the propanediol moiety (III) contains two asymmetric Carbons, and among the four possible stereoisomers, only the D-threo configuration (the one occurring on CAM) presents high antibacterial activity. This stereospecificity suggests that the conformation plays a crucial role on antibacterial activity.

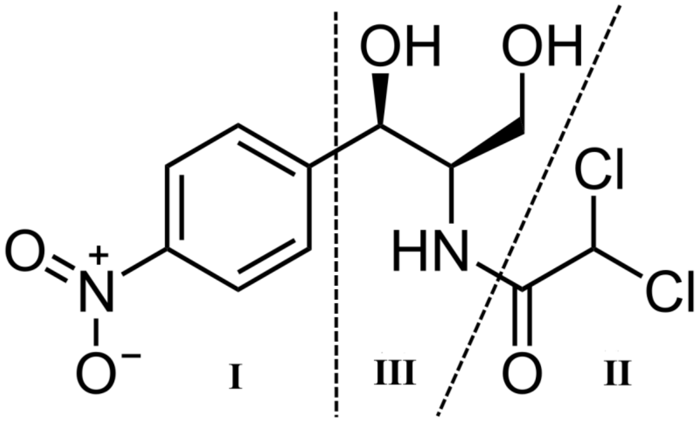

Figure 2.1.1. Chemical structure of CAM.

The conformational analysis of CAM is therefore of great interest both from the fundamental and applied points of view. For example, the binding of CAM to the *Escherichia coli* 70 S ribosome has been investigated by NMR spectroscopy [5], suggesting that it binds in its receptor site in essentially the same conformation that exists free in solution. The recognition is most likely of the classic lock and key type, with the ribosomal site being essentially an open gate for the fitting of the drug [5]. The geometry of the binding site has been recently reexamined using solid state crystallographic analyses [6]. One of the goals of these works is the comparison of the geometry of the ligand in the binding site with its free geometry in solution or with its geometry in the crystals [7]. According to Nicklaus, flexible ligands usually undergo substantial deformations upon binding to receptors [8].

The conformational behavior of pure CAM has been investigated in a number of papers (Dunitz, 1952; Chatterjee, Dattagupta, Saha, Saenger, & Müller, 1979; Acharya, Gowda, & Post, The Structure of Chloramphenicol, 1979; Jardetzky, 1963; Mitscher, Kautz, & Lapidus, 1969; Bustard, Egan, & Perun, 1973; Höltje & Kier, 1974; Fitzhugh, 1991). However, a number of contradictory results have been published, and currently there is no consensus on the actual conformation of CAM. For example, Chatterjee [10] investigated the crystalline structure of CAM using XRD, and proposed a conformer containing an intramolecular O-H···O hydrogen bond in which the primary hydroxyl group acts as hydrogen bond donor and the secondary one as acceptor. The same year, Acharya (Acharya, Gowda, & Post, The Structure of Chloramphenicol, 1979) reported a crystalline conformer in which the intramolecular hydrogen bond is established in the opposite direction (the secondary hydrogen bond acts as donor and the primary one as acceptor). None of these structures has been discarded, and both are considered in the current literature [17, 18, 19, 20, 21, 22].

The situation in solution is even worst. Using NMR spectroscopy, Jardetzky [12] concluded the presence of a unique CAM conformer in solvents of different polarity ranging from acetone to water. The predominant conformer contained an intramolecular O-H···O hydrogen bond in which the secondary hydroxyl acts as hydrogen bond donor.

However, using NMR spectroscopy and molecular modeling calculations Bustard [14] and Höltje [15] concluded the existence of a second conformer devoid of intramolecular hydrogen bonding. Hahn claimed a definitive study in view of these contradictory reports [1]. To mess things up, Fitzhugh [16] obtained the high dilution FTIR spectrum of CAM in $CDCl_3$ and suggested the coexistence of two intramolecularly hydrogen bonded conformers, in which the hydroxyl groups act alternatively as donors and acceptors. These conformational studies were performed some decades ago, and are therefore based mainly on experimental techniques. Bustard [14] also used a very simple molecular force field and Höltje [15] used an old semi empirical QM method (CNDO/2). To our knowledge, no conformational analysis has been reported using modern *ab initio* QM methods.

This paper revisits the conformational of CAM in the crystalline phase, in the melt, in free molecules in solution and in the gas phase. FTIR spectroscopy is used to discriminate between the two crystalline structures currently accepted (Chatterjee, Dattagupta, Saha, Saenger, & Müller, 1979; Acharya, Gowda, & Post, The Structure of Chloramphenicol, 1979). The conformational behavior of free CAM molecules in solution and in the gas phase is analyzed using *ab initio* QM calculations. The Onsager self-consistent reaction field (SCRF) model is used for the geometry optimizations in solution. These analyses provide clear results regarding the conformational behavior of CAM and establish the correct intramolecular hydrogen bonding pattern in each case. Finally, the stability of the conformers with the polarity of the medium is also discussed.

2.1.2. Experimental Section

2.1.2.1. Starting Materials

Chloramphenicol (purity ≥ 98 %) and acetonitrile were supplied by Aldrich Chemical Corp. (Spain) and were used as received.

2.1.2.2. Differential Scanning Calorimetry (DSC)

Thermal analyses were conducted on a Modulated DSC Q200 from TA Instruments. All the scans were carried out in hermetic aluminum pans under nitrogen atmosphere with sample weights between 5 and 10 mg. Two consecutive scans were performed from -80 ºC to 180 ºC with a scan rate of 20 ºC/min.

2.1.2.3. Fourier Transform Infrared Spectroscopy (FTIR)

FTIR spectra were recorded on a Nicolet AVATAR 370 Fourier transform infrared spectrophotometer. Spectra were taken with a resolution of 2 cm^{-1} and were averaged over 64 scans in the 4000-450 cm^{-1} range. Pure CAM FTIR samples were prepared by grinding CAM with KBr and pressing. The absorbance of the samples was within the range where the Lambert-Beer law is obeyed. A controlled high temperature transmission cell mounted in the spectrometer was used to obtain the spectra of molten samples. Second derivative spectra were smoothed using the Norris-Williams Gap Derivatives [23] using maximum gap sizes and segment lengths of 5 points and 5 cm^{-1} respectively in the derivative transformations.

Spectra in solution was recorded from 1 wt.% CAM solutions in acetonitrile using a variable path length cell equipped with IR grade Silicon windows (2 mm thick). To reduce interference fringes, the background was collected with the cell introduced in the FTIR bench. The spectrum of the solvent was then recorded. Finally, the spectrum of CAM in solution was obtained by substraction of the solvent spectrum in the appropriate spectral region.

2.1.2.4. Conformational Analysis

Ab initio calculations were performed using the Firefly QC package [24], which is partially based on the GAMESS (US) [25] source code. Geometry optimizations were carried out using the hybrid DFT method B3LYP-D3/DZP, consisting on the B3LYP functional [26, 27] extended with the D3 version of Grimme's dispersion correction [28]. The DZP basis function is based on the DZ basis function of Dunning [29] plus one set of polarization functions with the exponents recommended by Dunning for correlated calculations: H(p) 0.935; C(d) 0.550; N(d) 0.817; O(d) 1.185; Cl(d) 0.600 [30, 31]. Vibrational mode analyses were carried out at the B3LYP-D3/def2-TZVP(-f) (-f means without f polarization functions) [32]. Final geometries of improved accuracy for the stable conformers were also calculated using the Møller-Plesset perturbation theory, at the MP2/def2-TZVP(-f) level of theory.

2.1.3. Results and Discussion

2.1.3.1. DSC Analysis

Figure 2.1.2 shows the first and second DSC traces obtained for pure CAM. As can be seen, CAM is a crystalline solid melting at about 151 ºC. Cooling in the DSC at about -20 ºC/min results in a supercooled liquid with a glass transition temperature located at about 32 ºC. Considering this thermal behavior, supercooled CAM at room temperature is in the glassy state and is expected to crystallize quite slowly.

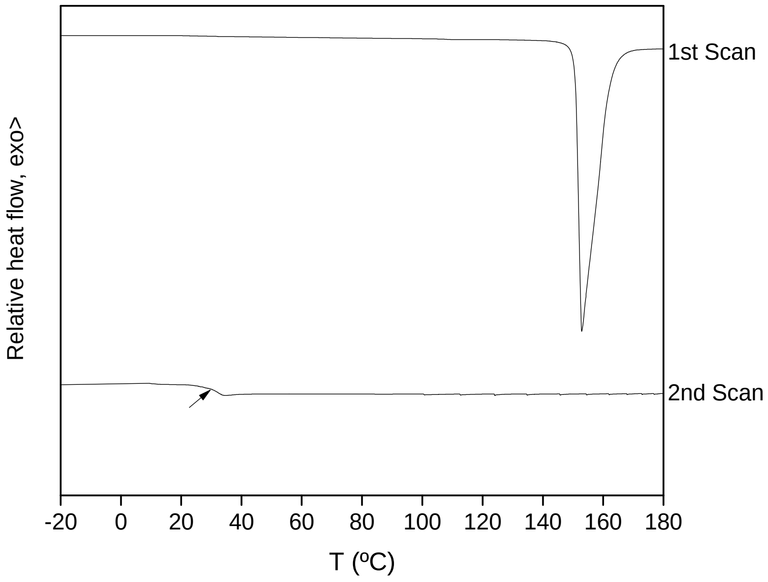

Figure 2.1.2. First scan DSC traces for PCL, CAM and PCL/CAM blends.

2.1.3.2. FTIR Analysis of Crystalline CAM

The hydrogen bonding pattern and consequently the infrared spectrum of crystalline CAM depend on the molecular conformation and on the crystalline packing. The crystalline structure of CAM was first investigated by Dunitz [9], although the atomic coordinates were reported only later by Chatterjee [10] and Acharya (Acharya, Gowda,

& Post, The Structure of Chloramphenicol, 1979). According to Chatterjee, CAM crystallizes in the orthorhombic space group $C222_1$, with a = 17.495 Å, b = 7.321 Å, c = 22.130 Å, and Z = 8 [10], adopting a conformation in which the dichloroacetamide moiety is folded back over the phenyl ring. Following the usual practice, both authors (Chatterjee, Dattagupta, Saha, Saenger, & Müller, 1979; Acharya, Gowda, & Post, The Structure of Chloramphenicol, 1979) determined the location of the heavy atoms by means of the X-Ray diffraction data, but the location of the hydrogen atoms was guessed from the molecular structure. However, since the location of the hydroxyl hydrogens is particularly difficult to assess, they proposed different orientations for the OH groups, resulting in two different conformers with different association patterns in the crystalline structure (Fig. 2.1.3). Both conformers present an intramolecular O-H···O-H hydrogen bond, but in the conformer proposed by Chatterjee the primary hydroxyl acts as donor (Fig. 2.1.3a) [10] while in the conformer proposed by Acharya the primary hydroxyl acts as acceptor (Fig. 2.1.3b) (Acharya, Gowda, & Post, The Structure of Chloramphenicol, 1979). Regarding the intermolecular association in the crystalline structure, both models present an intermolecular –N-H····O-H hydrogen bond (to primary OH, Fig. 2.1.3c and 2.1.3d) (Chatterjee, Dattagupta, Saha, Saenger, & Müller, 1979; Acharya, Gowda, & Post, The Structure of Chloramphenicol, 1979). However, the model of Chatterjee presents an intermolecular –O-H····O=C hydrogen bond in which the secondary OH acts as donor (Fig. 2.1.3c) [10] while the model of Acharya presents an intermolecular –O-H····Cl hydrogen bond in which the primary OH acts as donor (Fig. 2.1.3d) [11]. Both structures have received similar attention in the literature, and none has been discarded yet [17, 18, 19, 20, 21, 22].

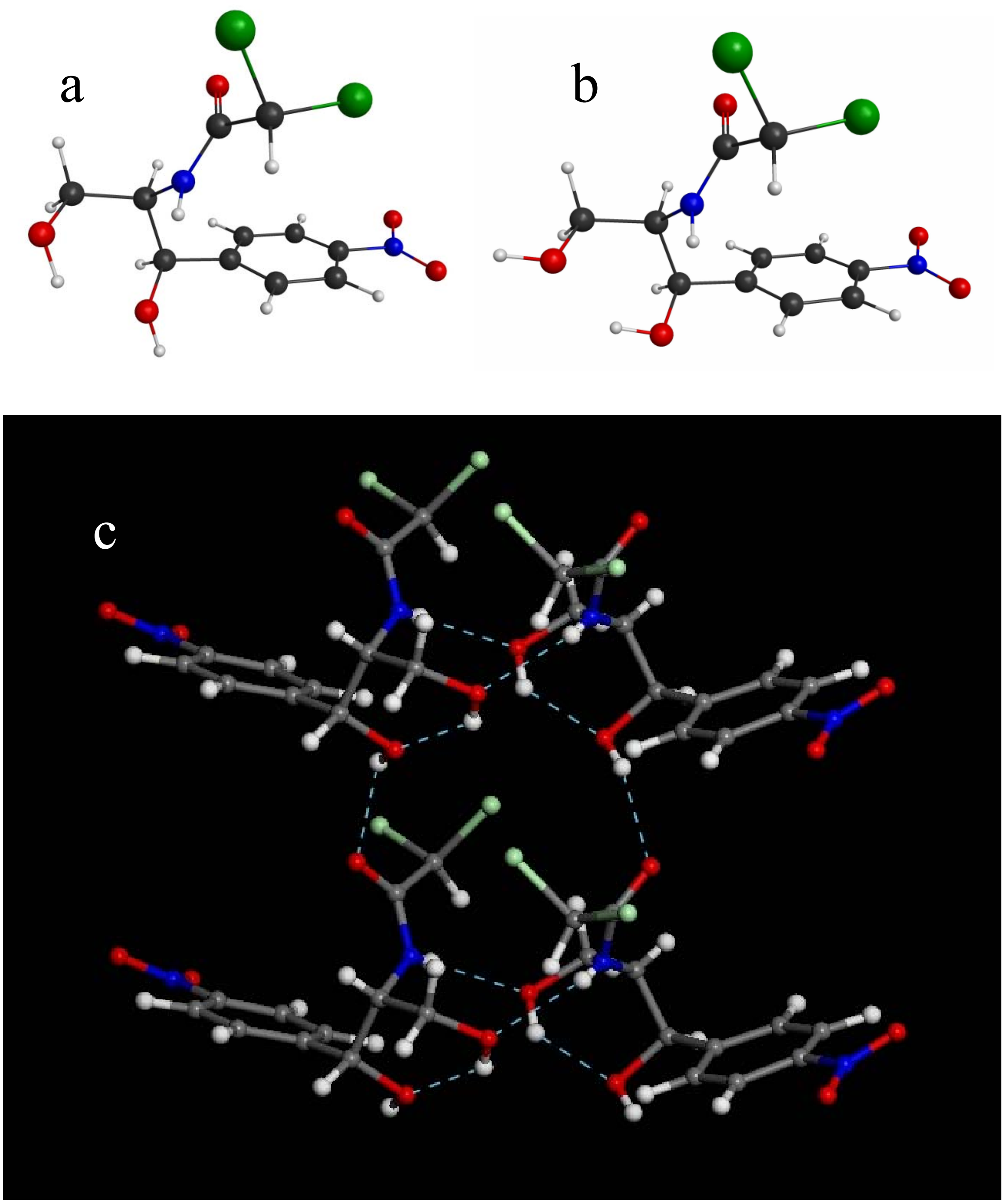
a
b
c

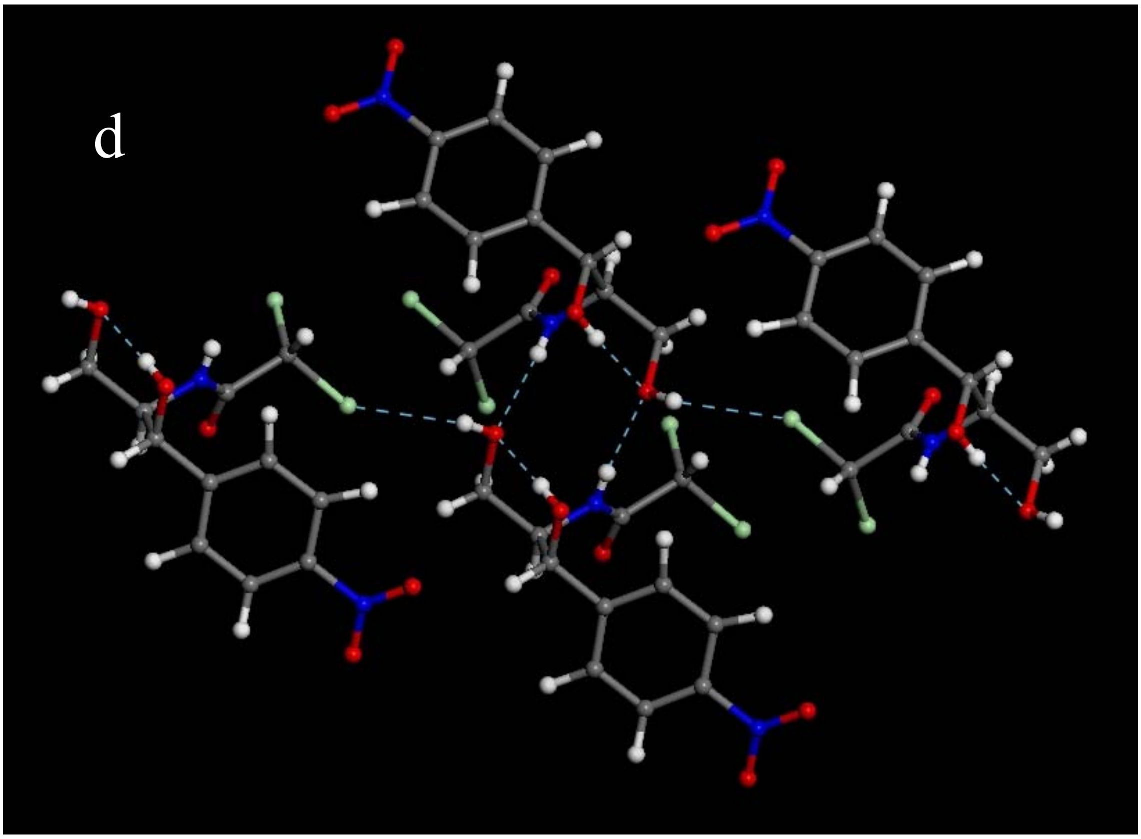

Figure 2.1.3. Conformers proposed by a) Chatterjee and b) Acharya, and molecular models showing the hydrogen bonding patterns in the resulting crystalline structures, c) Chatterjee and d) Acharya.

Figure 2.1.4 shows the X-H stretching region for pure crystalline CAM at room temperature, which can be used to discriminate the correct crystalline structure. As can be seen, pure crystalline CAM shows three bands located at about 3476, 3345 and 3262 cm^{-1}. In the solid or liquid phases, hydrogen bonded secondary amides generally exhibit a strong band at about 3270 cm^{-1} and a weak band at about 3100 cm^{-1} for the overtone of the Amide II band [33]. Hence, the band at 3262 cm^{-1} can be attributed to N-H stretching. This assignment is supported by the Raman spectrum of CAM in the X-H stretching region, where only a single band at about 3620 cm^{-1} [17] has been resolved (the OH bands only display weak broad Raman peaks since they are poor scattered [34]). Therefore, the bands located at 3476 and 3345 cm^{-1} can be attributed to the two OH groups present in CAM. The band at 3345 cm^{-1} is strongly red shifted (free OH stretching occurs in the

3650-3600 cm^{-1} range [33]) and is only attributable to hydroxyl stretching in cooperatively hydrogen bonded O-H···O-H systems. The band at 3476 cm^{-1} can be attributed to O-H···O=C interactions (usually in the range 3600-3450 cm^{-1} [33]) assuming the model of Chatterjee [10], but is too red shifted to be attributable to the weak O-H···Cl interactions proposed by Acharya (Acharya, Gowda, & Post, The Structure of Chloramphenicol, 1979).

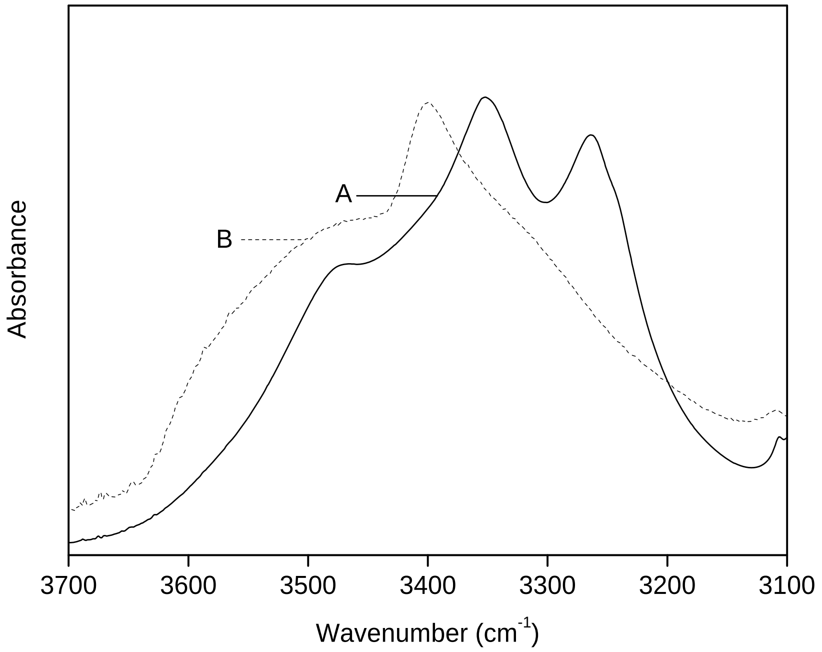

Figure 2.1.4. Hydroxyl stretching region for pure crystalline CAM (A), and molten CAM at 160 ºC (B).

The analysis of the hydrogen bonding cooperativity in the models of Chatterjee and Acharya gives additional support to the former structure. In the model of Chatterjee [10], the interacting groups form linear N-H···O-H···O-H···O=C chains (see Fig. 2.1.3c). Nonetheless, in the model of Acharya (Acharya, Gowda, & Post, The Structure of Chloramphenicol, 1979) the interacting groups form bifurcated (N-H)(O-H)>O-H···Cl-C structures (see Fig. 2.1.3d). Recently, Ohno et al. have proposed a simple method to analyze the degree of cooperativity (or the strength of hydrogen bonding) in O-H···O-H hydrogen bonded chains [35]. Each O-H···O-H couple is considered a donor-acceptor (DA) group, and the interactions established by D or A with surrounding molecules are assumed to strengthen or weaken the hydrogen bonding interaction between D and A. The number of protons accepted by D is termed a_D (in the 0-2 range), the number of protons accepted by A is a_A (0-1), and the number of protons donated by A is d_A (0-1). The hydrogen bonding structure adopted by the DA couple with its surroundings is then characterized by the $a_D DA d_A a_A$ string, and the strength of the DA hydrogen bond is classified according to the cooperativity indicator $M_{OH} = a_D + d_A - a_A$, proportional to the hydrogen bonding energy [35]. Application of this procedure to the O-H···O-H interaction in the crystalline structure proposed by Chatterjee results in the 1DA10 string and $M_{OH} = 2$, but in the Acharya case the string is 0DA11 and the indicator is $M_{OH} = 0$. This analysis indicates strong cooperativity in the structure of Chatterjee, but no cooperativity in the structure of Acharya. For the Structure of Acharya, the intramolecularly hydrogen bonded OH stretching mode should be located above 3500 cm^{-1}, as in other non-cooperative intramolecularly hydrogen bonded 1,3 diols [36, 37]. For the structure of Chatterjee, cooperativity should be similar to that occurring in tetrols [38, 39], in which the cooperativity indicator is also $M_{OH} = 2$. These compounds contain four OH groups in 1,3 relative positions arranged along a linear chain, and have been investigated as model systems for the vibrational spectroscopy of naturally occurring hydrogen bonding networks. In the liquid phase the all-syn tetrol shows a very broad OH-stretching band peaking at 3388 cm^{-1} [38], location comparable to the band at 3345 cm^{-1} observed in crystalline CAM, particularly considering the different states of aggregation (liquid vs. crystalline). In summary, the two OH stretching bands observed in crystalline CAM can be feasibly assigned assuming the conformation assumed by Chatterjee, but neither of them is compatible with the atomic coordinates provided for the OH groups by Acharya.

2.1.3.3. FTIR Analysis of Molten CAM and Free CAM in Solution

Figure 2.1.4 also shows the O-H stretching band of molten CAM at 160 ºC. In the melt, only a broad envelope can be observed for the OH stretching band, indicating molecular disorder and a broad range of interaction strengths. The N-H stretching band shifts to higher wavenumbers (3400 cm^{-1}), indicating the rupture of the N-H···O-H interactions occurring in the crystalline phase, but remains below the typical range for free N-H groups (3460-3440 cm^{-1} [33]), suggesting the occurrence of weak interactions in the amorphous phase such as contacts with the aromatic rings.

The Amide I stretching region of CAM is shown in Figure 2.1.5. Pure crystalline CAM displays a narrow peak at about 1687 cm^{-1}. Upon melting the peak shows an unexpectedly large broadening (its half height width reaches about 40 cm^{-1}), and maintains its location instead of shifting to higher wavenumbers as expected. Moreover, after quenching to room temperature the peak red shifts to about 1679 cm^{-1}, at even lower wavenumbers than the initial crystalline C=O band. These changes suggest the formation upon melting of a new conformer located at lower wavenumbers, since the O-H•••O=C interactions in the amorphous phase can hardly be stronger than in the crystalline phase. Second derivative spectroscopy of quenched CAM at room temperature reveals two components located at about 1690 and 1675 cm^{-1}, where the lower wavenumber band can be attributed to the new conformer formed upon melting.

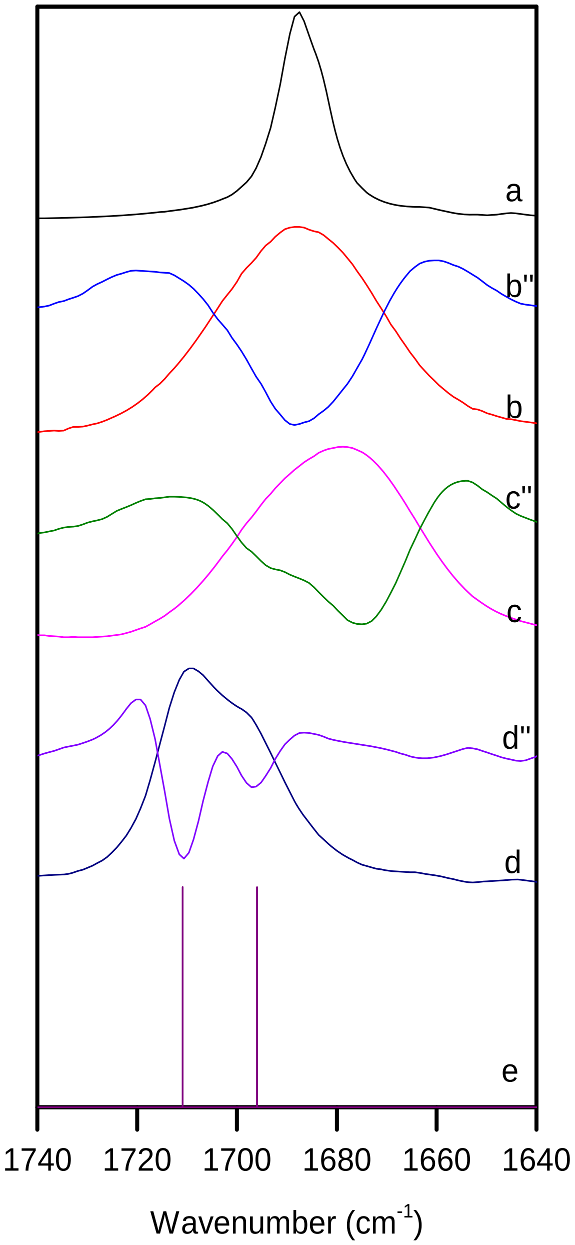

Figure 2.1.5. Carbonyl stretching region of CAM and second derivatives ('') of: a) crystalline CAM at 40 ºC, b) molten CAM at 160 ºC, c) supercooled CAM at 40 ºC, d) CAM in acetonitrile solution (1 wt.%), and e) computed spectrum of CAM in acetonitrile solution at the B3LYP-D3/def2-TZVP(-f) level of theory (scaling factor 0.9834).

Figure 2.1.5 also displays the spectrum of CAM in dilute acetonitrile (ACN) solution (1 wt.%). As can be seen, the C=O stretching band of CAM in dilute solution shows two components located at about 1697 and 1710 cm^{-1}. The occurrence of other split bands in this spectrum supports the presence of different conformers over Fermi resonance as the origin of the splitting. The most probable explanation for the conformational sensitivity of the C=O group is some conformational isomerism involving the electronegative (chlorine) atoms present in the alpha carbon relative to the C=O group [40, 18]. Most studies dealing with these effects have focused however on CO-CH$_2$-X structures (where X is an electronegative atom such as F, O, N, Cl, Br, S, I) [41, 42, 43, 44]. The presence of a single electronegative atom in the alpha Carbon is known to modify the typical threefold rotational isomerism around the CO-Cα bond (*anti, gauche*±) to a twofold one (*anti, syn*) [18, 41, 42], and shift the location of the C=O stretching band [45].

2.1.3.4. Ab Initio Quantum Mechanical Calculations

Assuming that the amide bond prefers the *anti* conformation, CAM contains seven potential rotatable bonds (see scheme 2.1.6). The first four dihedrals determine to a large extent the overall shape of the molecule, while the remaining three have a minor effect. From the analysis of the coupling constants obtained in different solvents by NMR spectroscopy, Jardetzky [12] proposed the existence of a single predominant conformer stabilized by an intramolecular HB. Bustard [14] combined NMR spectroscopy and a molecular mechanics approach to analyze the conformational preferences of CAM and proposed two dominant conformers in solution, one of them unable to establish intramolecular HB since ϕ_3 = 180º. Höltje [15] arrived later at essentially the same geometries using semiempirical QM calculations (see table 2.1.1 for conformational details). These results [14, 15] conflict with the presence of intramolecular HBs reported by other authors using NMR [12] and FTIR [16], and with the prevalence of a single conformer reported by Jardetzky [12], making a definitive study necessary [1].

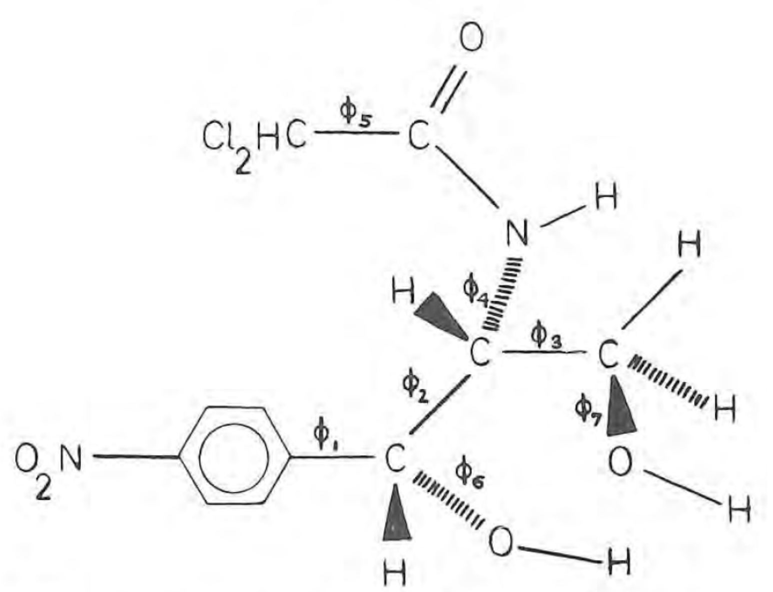

Figure 2.1.6. The seven rotatable bonds in chloramphenicol.

Table 2.1.1. Dihedrals proposed by Höltje for the two most stable conformers of CAM in solution, and dihedrals corresponding to the crystalline conformers proposed by Chatterjee and Acharya.

Dihedral	Reference atoms	Conf. 1	Conf. 2	Chatterjee	Acharya
ϕ_1	C_aC_aCC	90	90	91	95
ϕ_2	C_aCCN	-60	-60	-55	-58
ϕ_3	CCCO	180	60	72	70
ϕ_4	HCNH	180	180	-162	175
ϕ_5	OCCH	60	60	-171	-162
ϕ_6	C_aCOH	-60	180	-18	146
ϕ_7	CCOH	-60	30	-42	-124

Hence, the conformational behavior of CAM in solution has been revisited here. The task has been simplified reconsidering exclusively a few reliable results reported so far. The minimum of ϕ_1 is known to be at about 90º [46, 47]. Bustard [14] concluded using NMR spectroscopy that ϕ_4 adopts the *anti* conformation. In addition, ϕ_5 is known to adopt both the *anti* and *syn* conformations in condensed phases (though it prefers exclusively the *syn* conformation in vacuum) [18]. Hence, ϕ_1 = 90º, ϕ_4 = 180º and ϕ_5 = 0º, 180º have been assumed here. Regarding ϕ_2, ϕ_3, ϕ_6 and ϕ_7 the *anti* and *gauche*± rotamers have been considered. Therefore, 162 molecular models have been built and optimized at the B3LYP-D3/DZP level of theory. To account for the solvent effects, the Kirkwood-Onsager self-consistent reaction field (SCRF) method has been applied in the optimizations [48, 49, 50]. This model locates the dipole moment of the solute in the center of a spherical cavity, and calculates the interaction energy between the dipole moment and the surrounding solvent, characterized by its dielectric constant. In case of nearly spherical molecules, the cavity radius can be determined from the molar volume of the molecule, resulting in R = 4.4 Å according to the density of amorphous CAM (1.47 g/cm^3 [51]). In case of more elongated molecules, it is preferred to take the cavity radius as the half-length of the long-molecular axis without van-der-waals radii [52], leading to R = 4.6 Å according to the V-shaped conformations in table 4. Both values are rather close, suggesting that CAM should work correctly regarding the cavity shape criterion. Another limitation of this model is the lack of higher order multipoles to properly describe the electrostatic potential of the solute [50]. Anyway, this model is very cheap from a computational point of view and has been widely applied with substantial success. In the special case of roundish molecules with large dipole moments, the SCRF model is considered to include sufficient physics to be meaningful [50]. In this paper, the radius has been set to R = 4.4 Å and the dielectric constant of acetonitrile to 37.5.

Table 2.1.2 shows the dihedral angles for the 6 conformers of lower energy obtained in this conformational analysis. According to the computed electronic energies, dilute CAM solutions in acetonitrile should contain mainly conformers **I** and **II** in similar amounts (see Figure 2.1.7 for geometries). These two conformers adopt similar geometries (they only differ in the orientation of the dichloromethyl group, determined by ϕ_5) and show similar energies. Our results discard the prevalence of conformer 1 (the non-autoassociated one of Bustard and Höltje, see table 2.1.1); in fact, the energy of the first conformer with ϕ_3 = 180º (conformer **V** in table 2.1.5) is about 32 kJ/mol larger than that of conformer **I**. In addition, conformer 2 of Höltje is not a true minimum since optimization of this geometry results in a final structure with $\phi_7 \approx 180º$ (corresponding to conformer **I**). Similarly to conformers **I** and **II**, the remaining conformers also follow a pairwise arrangement, in the sense that in spite of differing in ϕ5, show similar energies and geometries. Conformers **I-IV** present an intramolecular hydrogen bond, while this interaction is not possible in conformers **V** and **VI** since ϕ_3 adopts the *anti* conformation. Optimizations have also lead to a Chaterjee-like conformer (not listed in table 2) with ΔE ~ 35 kJ/mol, making evident the importance of the strong cooperative intermolecular interactions in the crystalline structure (the computed ΔE corresponds actually to acetonitrile medium, but should be of about the same order of magnitude for the electrostatic interactions with the crystalline environment).

Table 2.1.2. Dihedral angles and electronic energies for the first six conformers of CAM in acetonitrile solution optimized at the B3LYP-D3/DZP level of theory.

Dihedral	**I**	**II**	**III**	**IV**	**V**	**VI**
ϕ_1 (C_aC_aCC)	103	106	117	101	101	101
ϕ_2 (C_aCCN)	-64	-68	-48	-56	-60	-64
ϕ_3 (CCCO)	63	63	-36	-36	-175	180
ϕ_4 (HCNH)	154	153	167	168	155	144
ϕ_5 (OCCH)	42	154	38	112	44	159
ϕ_6 (C_aCOH)	165	168	-164	-161	-160	-158
ϕ_7 (CCOH)	176	176	-169	-171	180	178
E (kJ/mol)	0	0.4	17.0	20.7	31.8	32.2

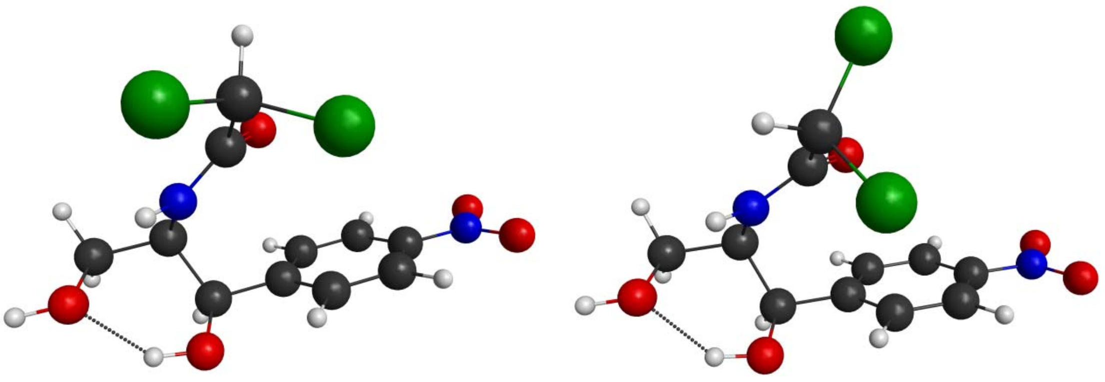

Figure 2.1.7. Equilibrium geometries for conformers I (left) and II (right) in acetonitrile at the B3LYP-D3/DZP level of theory.

Considering that conformers **I** and **II** share the major part of the geometry (they only differ in the rotation of the dichloromethyl group), the results of this conformational analysis are compatible with the work of Jardetzky [12] (who concluded the existence of a single predominant conformer stabilized by an intramolecular HB). However, our analysis is not compatible with the Bailey method used by Bustard [14] to analyze the relative prevalence of ϕ_3(CCCO). In fact, the Bailey method is known to be based on questionable assumptions [53, 54] and has been seldom used in the literature.

Thus, only conformers **I** and **II** must be considered to explain the spectral properties of CAM in solution. The vibrational analysis of CAM in acetonitrile solution has been carried out using the Kirkwood-Onsager SCRF method at the B3LYP1-D3/def2-TZVP(-f) level of theory. The locations computed for the C=O stretching bands of conformers **I** and **II** are 1725 and 1740 cm^{-1} respectively. The computed values are larger than the experimental ones (1697 and 1710 cm^{-1}) due mainly to the neglect of anharmonicity effects, but most importantly the computed shift ($\Delta\nu = 15$ cm^{-1}) is in good agreement with the experimental one ($\Delta\nu = 13$ cm^{-1}), supporting the rotation of the dichloromethyl group as the actual source for the conformational sensitivity of the C=O stretching band (see Fig. 2.1.5). In addition, it is worth to notice that the blue shift relative to the location of aliphatic secondary amides (absorbing at about 1691 cm^{-1} [55, 45]) is larger for conformer **II** (ϕ_5(HCCO) in *anti* conformation) because the chlorine atoms are closer to the C=O group and the electronic interaction between these moieties is stronger.

Conformers **I** and **II** have also been optimized in vacuum in order to extend the analysis of the conformational behavior to different media. Since in vacuum the dichloroacetamide group prefers exclusively the *syn* conformation [18], a single conformer was a priori expected in this medium. However, minimizations lead again to two different conformers, according to the absence of negative frequencies in the vibrational analysis at the B3LYP-D3/def2-TZVP(-f) level. In addition, conformer **I** prevails almost completely over conformer **II** in vacuum since ΔE ≈ 12 kJ/mol. Table 2.1.3 summarizes the most relevant results obtained for conformers **I** and **II** in vacuum and in acetonitrile at the higher levels of theory used in this investigation.

Table 2.1.3. Optimized geometries for conformers I and II in vacuum and acetonitrile at the MP2/def2-TZVP(-f) level of theory. Dipole moments and electronic energies have been obtained from single point computations at the MP2/def2-TZVPP level. Free energies and relative populations (N_I/N) also consider the harmonic vibrational analysis at the B3LYP-D3/def2-TZVP(-f) level of theory.

	Vacuum		**Acetonitrile**	
Dihedral	**I**	**II**	**I**	**II**
ϕ_1 (C_aC_aCC)	96	98	98	101
ϕ_2 (C_aCCN)	-61	-60	-62	-64
ϕ_3 (CCCO)	62	61	65	66
ϕ_4 (HCNH)	-178	-173	152	151
ϕ_5 (OCCH)	-28	-153	51	160
ϕ_6 (C_aCOH)	167	168	164	166
ϕ_7 (CCOH)	174	175	176	177
μ (D)	9.4	10.4	19.5	21.0
ΔE (kJ/mol)	0	12.5	0	0.9
ΔG^o (kJ/mol)	0	14.0	0	0
N_I/N	0.996	0.004	0.5	0.5

In order to rationalize the conformational behavior around ϕ_5, the relaxed potential energy surfaces (PES) have been scanned both in vacuum and in acetonitrile solution (see Figure 2.1.8). In addition, since the stable conformers in both media (see Figure 2.1.7) show chlorine atoms close to the aromatic ring, their geometries have been scrutinized for the occurrence of intramolecular C-Cl···π interactions. These contacts, termed halogen bonds, are widespread among pharmaceutical compounds since about 40% drugs currently on the market or in clinical trials are halogenated [56]. However, they have been usually overlooked because their importance in, for example, crystals and biological systems, has been only recently established [57, 58]. The halogen bond is a highly directional and specific non-covalent interaction, analogous to the hydrogen bond. It is formed between a halogen and a proximal halogen-bond acceptor (such as O, N, S, and aromatic ring) [56, 58]. Figure 2.1.8 also displays the distance between the Cl atoms and the closest aromatic π-bonds for the conformers of CAM in vacuum. As can be seen, the minimum distances occur at about 50º ($d_{Cl\text{-}\pi}$ = 3.86 Å) and 150º ($d_{Cl\text{-}\pi}$ = 3.88 Å), suggesting the formation of two C-Cl···π halogen bonds. The observed distances are in good agreement with those reported for the complexes formed between wild-type enzymes and chlorobenzyl cyanide [56], and support the occurrence of intramolecular C-Cl···π interactions in CAM. The halogen bond occurring at about 50º seems responsible for the asymmetry of the PES surface in vacuum, which is skewed to positive dihedrals. The halogen bond occurring at about 150º seems responsible for the unexpected minimum occurring at about 150º in vacuum, corresponding to conformer **II**.

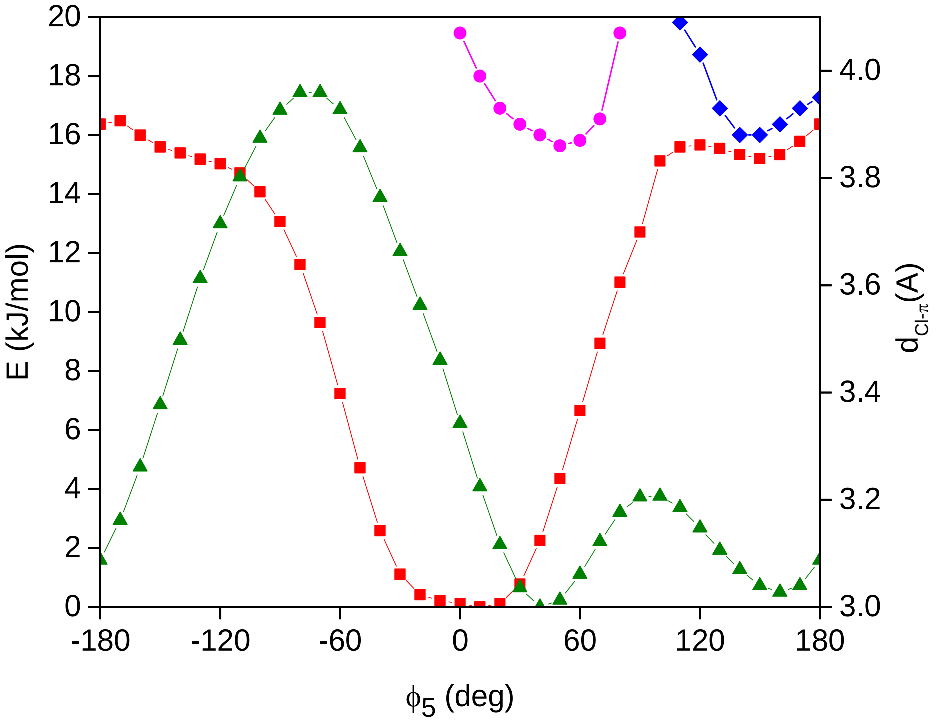

Figure 2.1 8. Relaxed PES scans around ϕ5 (HCCO dihedral) of CAM in vacuum (■) and in acetonitrile solution (▲) together with the distances between the two chlorine atoms and the aromatic ring for the structures obtained in vacuum (● & ♦). Computations at the B3LYP-D3/def2-TZVP(-f) level of theory.

Figure 2.1.8 also displays the PES surface computed in acetonitrile solution. In this case, conformer **II** is strongly stabilized, and its energy becomes similar to that of conformer **I**. This strong stabilization can be accounted for using the classical Onsager model, which attributes the stabilization of polar conformers in solution to favorable electrostatic interactions with the solvent [49, 59]. According to this model, the difference in the free energy of solvation between two conformers of the same size is given by equation 1:

$$\Delta(\Delta G^{o}_{solv}) = \frac{-N_A}{4\pi\varepsilon_0}\frac{\varepsilon_r - 1}{2\varepsilon_r + 1}\frac{\mu_A^2 - \mu_B^2}{a^3} \tag{1}$$

where N_A is the Avogadro number, ε_0 is the permittivity of vacuum, ε_r is the relative permittivity and μ is the dipole moment. The stabilizing contribution arising from electrostatic interactions with the solvent depends on the stabilizing character of the medium, given by the Onsager term, $(\varepsilon_r - 1)/(2\varepsilon_r + 1)$, and on the difference of the square of the dipole moments. In vacuum, the *anti* conformer does not suffer any electrostatic stabilizing effect from the solvent because the Onsager term is zero, and the dichloroacetamide moiety prefers the *syn* conformation. However, in acetonitrile solution, the more polar *anti* conformer (see table 2.1.3) is strongly stabilized by the solvent up to the point where the energies of the *syn* and the *anti* conformers become similar. It must be noticed that the classical Eq. 1 does not account for the distortion of the wave function occurring when the conformer is introduced in the polar medium (which originates the increase in dipole moment observed in table 2.1.3), and does not therefore account for the corresponding variations of electronic energy. It is therefore a less accurate approach to the problem than the SCRF method used in this paper [50], and is introduced here only for a qualitative discussion of the results.

In summary, the PES scans in Figure 2.1.8 indicate that both the *anti* and the *syn* conformers are stable conformers regardless of the medium. In media of high polarity, both are present in similar amounts, but in solvents of lower dielectric constant, conformer **I** is expected to dominate over conformer **II**. This situation is actually observed in molten CAM, though in this case the hydrogen bonding ability of the conformers could also affect the conformational equilibrium.

2.1.4. Conclusions

The conformational behavior of CAM has been has been revisited in order to enlighten the contradictory results reported so far. The analysis of the X-H stretching region indicates that CAM crystallizes in the conformation proposed by Chatterjee [10], and not in the conformation proposed by Acharya (Acharya, Gowda, & Post, The Structure of Chloramphenicol, 1979). The OH stretching band observed at 3345 cm^{-1} is particularly meaningful to discriminate the correct conformer, since it is only attributable to the cooperative O-H···O-H interactions occurring in the structure proposed by Chatterjee. In this crystalline structure, the primary hydroxyl group acts as hydrogen bond donor and the secondary hydroxyl group acts as acceptor. Halogen bonding is not observed in the crystalline phase ($d_{Cl\text{-}\pi} \sim 4.4$ Å).

Upon breaking the crystalline structure, the hydroxyl groups of CAM turn over so that the secondary hydroxyl group acts as hydrogen bond donor and the primary one acts as acceptor in the dominant conformers. This change allows the molecule to fold back further to form an intramolecular C-Cl···π halogen bond, resulting in two different conformers depending on the Chlorine atom participating in the halogen bond. In media of low dielectric constant (vacuum or solvents of low polarity), the ϕ_5 dihedral (HCCO) prefers the *syn* conformation, and conformer **I** is the only dominant conformer. Solvents of increased polarity tend to stabilize conformer **II**, in which the ϕ_5 dihedral (HCCO) adopts the *anti* conformation and the halogen bond is established by the second chlorine atom. Conformer **II** presents a larger dipole moment, and thus, more favorable electrostatic interactions with polar media. The two conformers can be easily distinguished experimentally by means of infrared spectroscopy taking advantage of the conformational sensitivity of the C=O stretching band (the *syn* rotamer absorbs at lower wavenumbers). In acetonitrile solution both conformers present similar stabilities. In vacuum only conformer **I** should be detected. In media of intermediate polarity (such as molten CAM) intermediate situations can be expected.

References

[1] F.E. Hahn, P. Gund, "A Structural Model of the Chloramphenicol Receptor Site", *Drug Receptor Interactions in Antimicrobial Chemotherapy. Topics in Infectious Diseases, J. Drews, E. Hahn, Edits., Vienna, Springer*, 1975, 245-265.

[2] O. Pongs, "Chloramphenicol", *Mechanism of Action of Antibacterial Agents, F. E. Hahn, Ed., Berlin, Springer*, 1979, 26-42.

[3] S. Kalita, B. Devi, R. Kandimalla, K.K. Sharma, A. Sharma, K. Kalita, A.C. Kataki, J. Kotoky, "Chloramphenicol encapsulated in poly-e-caprolactone-pluronic composite: nanoparticles for treatment of MRSA-infected burn wounds", *Int. J. Nanomedicine*, 2015, **10**, 2971-2984.

[4] World Health Organization (WHO), "Essential medicines" 04 2015. Available: http://www.who.int/emLib/.

[5] T.R. Tritton, "Ribosome-chloramphenicol interactions: A Nuclear magnetic resonance study", *Arch. Biochem. Biophys.*, 1979, **197**, 10-17.

[6] G. Dinos, C.M. Athanassopoulos, D.A. Missiri, C. Giannopoulou, I.A. Vlachogiannis, G.E. Papadopoulos, D. Papaioannou, D.M. Kalpaxis, "Chloramphenicol Derivatives as Antibacterial and Anticancer Agents: Historic Problems and Current Solutions", *Antibiotics*, 2016, **5**.

[7] M. Vieth, J.D. Hirst, C.L. Brooks III, "Do active site conformations of small ligands correspond to low free-energy solution structures?", *J. Comput. Aided Mol. Des.*, 1998, **12**, 563-572.

[8] M.C. Nicklaus, S. Wang, J.S. Driscoll, G.W.A. Milne, "Conformational Changes of Small Molecules Binding to Proteins", *Bioorg. Med. Chem.*, 1995, **3**, 411-428.

[9] J.D. Dunitz, "The Crystal Structure of Chloramphenicol and Bromamphenicol", *J. Am. Chem. Soc.*, 1952, **74**, 995–999.

[10] C. Chatterjee, J.K. Dattagupta, N.N. Saha, W. Saenger, K. Müller, "Crystal and molecular structure of chloramphenicol", *J. Cryst. Mol. Struct.*, 1979, **9**, 295–304.

[11] K.R. Acharya, D.S.S. Gowda, M. Post, "The Structure of Chloramphenicol", *Acta Cryst. B*, 1979, **B35**, 1360-1363.

[12] O. Jardetzky, "Studies on the Mechanism of Action of Chloramphenicol. I. The Conformation of Chloramphenicol in Solution", *J. Biol. Chem.*, 1963, **238**, 2498-2508.

[13] L.A. Mitscher, F. Kautz, J. Lapidus, "Optical rotatory dispersion and circular dichroism of of diastereoisomers. I. The ephedrines and chloramphenicols", *Can. J. Chem.*, 1969, **47**, 1957-1963.

[14] T.M. Bustard, R.S. Egan, T.J. Perun, "Conformational studies on chloramphenicol and related molecules", *Tetrahedron*, 1973, **29(14)**, 1961-1967.

[15] H. Höltje, L.B. Kier, "A theoretical Approach to Structure-Activity Relationships of Chloramphenicol and Congeners", *J. Med. Chem.*, 1974, **17(8)**, 814-819.

[16] A.L. Fitzhugh, "Chloramphenicol: High dilution FT-IR evidence for an intramolecular hydrogen bond", *Bioorg. Med. Chem. Lett.*, 1991, **1(5)**, 257-262.

[17] D. Sajan, G.D. Sockalingum, M. Manfait, I. Hubert Joe, V.S. Jayakumar, "NIR-FT Raman, FT-IR and surface-enhanced Raman scattering spectra, with theoretical simulations on chloramphenicol", *J. Raman Spectrosc.*, 2008, **39**, 1772–1783.

[18] S.L. Hinchley, H.E. Robertson, L.J. McLachlan, C.A. Morrison, D.W.H. Rankin, S.J. Simpson, E.W. Thomas, "Conformational Analysis with Both Experimental and Computational Data for Both Gaseous and Crystalline Phases: Unexpected Interactions in N-Methyldichloroacetamide", *J. Phys. Chem. A*, 2004, **108**, 185-193.

[19] A.I. Ramos, T.M. Braga, Silva, J.A. Fernandes, Ribeiro-Claro, M.F. Silva Lopes, F.A. Almeida Paz, S.S. Braga, "Chloramphenicol·cyclodextrin inclusion compounds: co-

dissolution and mechanochemical preparations and antibacterial action", *CrystEngComm*, 2013, **15**, 2822-2834.

[20] G.R. Desiraju, T. Steiner, *The Weak Hydrogen Bond: In Structural Chemistry and Biology, New York: Oxford University Press*, 1999, 217-219.

[21] J.L. Hansen, B. Moore, T.A. Steitz, "Structures of Five Antibiotics Bound at the Peptidyl Transferase Center of the Large Ribosomal Subunit", *J. Mol. Biol.*, 2003, **330**, 1061-1075.

[22] H.D. Höltje, M. Tintelnot, "Theoretical Investigations on Interactions Between Pharmacon Molecules and Receptor Models V: Construction of a Model for the Ribosomal Binding Site of Chloramphenicol", *Quant. Struct.-Act. Relat.*, 1984, **3**, 6-9.

[23] K.H. Norris, C. Williams, "Optimization of Mathematical Treatments of Raw Near-Infrared Signal in the Measurement of Protein in Hard Red Spring Wheat. I. Influence of Particle Size", *Cereal Chem.*, 1984, **61(2)**, 158–165.

[24] A.A. Granovsky, "Firefly version 8". Available: www http://classic.chem.msu.su/gran/firefly/index.htmL.

[25] M.W. Schmidt, K.K. Baldridge, J.A. Boatz, S.T. Elbert, M.S. Gordon, J.H. Jensen, S. Koseki, N. Matsunaga, K.A. Nguyen, S. Su, T.L. Windus, M.M.Dupuis, J.A. Montgomery, "General Atomic and Molecular Electronic Structure System", *J. Comput. Chem.*, 1993, **14**, 1347-1363.

[26] A.D. Becke, "Density-functional thermochemistry. III. The role of exact exchange", *J. Chem. Phys.*, 1993, 98, 5648-5652.

[27] C. Lee, W. Yang, R.G. Parr, "Development of the Colle-Salvetti correlation-energy formula into a functional of the electron density", *Phys. Rev. B*, 1988, **37**, 785-789.

[28] S. Grimme, J. Antony, S. Ehrlich, H. Krieg, "A consistent and accurate ab initio parametrization of density functional dispersion correction (DFT-D) for the 94 elements H-Pu", *J. Chem. Phys.*, 2010, **132**, 154104.

[29] T.H. Dunning, J. Hay, "Gaussian Basis Sets for Molecular Calculations", *Methods of Electronic Structure Theory, H. F. Schaefer, Ed., New York, Springer*, 1977, 1-27.

[30] T.H. Dunning, "Gaussian basis sets for use in correlated molecular calculations. I. The atoms boron through neon and hydrogen", *J. Chem. Phys.*, 1989, **90(2)**, 1007-1023.

[31] D.E. Woon, T.H. Dunning, "Gaussian basis sets for use in correlated molecular calculations. III. The atoms aluminum through argon", *J. Chem. Phys*, 1993, **98(2)**, 1358-1371.

[32] F. Weigend, R. Ahlrichs, "Balanced basis sets of split valence, triple zeta valence and quadruple zeta valence quality for H to Rn: Design and assessment of accuracy", *Phys. Chem. Chem. Phys.*, 2005, **7(18)**, 3297-3305.

[33] G. Socrates, *Infrared and Raman Characteristic Group Frequencies: Tables and Charts, 3 ed., Chichester: John Wiley and Sons*, 2001.

[34] R.M. Silverstein, F.X. Webster, D.J. KiemLe, *Spectrometric Identification of Organic Compounds, 7 ed., Wiley*, 2005.

[35] K. Ohno, T. Shimoaka, N. Akai, Y. Katsumoto, "Relationship between the Broad OH Stretching Band of Methanol and Hydrogen-Bonding Patterns in the Liquid Phase", *J. Phys. Chem. A*, 2008, **112**, 7342–7348.

[36] R. Iwamoto, T. Matsuda, H. Kusanagi, "Contrast effect of hydrogen bonding on the acceptor and donor OH groups of intramolecularly hydrogen-bonded OH pairs in diols", *Spectrochim. Acta Part A*, 2005, 62, 97–104.

[37] J.R. Lane, J. Contreras-García, J. Piquemal, B.J. Miller, H.G. Kjaergaard, “Are Bond Critical Points Really Critical for Hydrogen Bonding?”, *J. Chem. Theory Comput.*, 2013, **9**, 3263-3266.

[38] J. Seehusen, D. Schwarzer, J. Lindner, P. Vöhringer, “Equilibrium and mid-infrared driven vibrational dynamics of artificial hydrogen-bonded networks”, *Phys. Chem. Chem. Phys.*, 2009, **11**, 8484–8495.

[39] K. Kwac, E. Geva, “A Mixed Quantum-Classical Molecular Dynamics Study of anti-Tetrol and syn-Tetrol Dissolved in Liquid Chloroform: Hydrogen-Bond Structure and Its Signature on the Infrared Absorption Spectrum”, *J. Phys. Chem. B*, 2013, **117**, 16493-16505.

[40] M.F. Santos, C.B. Braga, T.C. Rozada, E.A. Basso, B.C. Fiorin, “Rotational isomerism of some chloroacetamides: Theoretical and experimental studies through calculations, infrared and NMR”, *Spectrochim. Acta A Mol. Biomol. Spectrosc.,* 2014, **129**, 148–156.

[41] S.A. Guerrero, J.R.T. Barros, B. Wladislaw, R. Rittner, R. Olivato, “Conformational studies of a-substituted carbonyl compounds. Part 1. Conformation and electronic interaction in hetero-substituted acetones by infrared and ultraviolet spectroscopy”, *J. Chem. Soc. Perkin Trans.*, 1983, **2***,* 1053-1058.

[42] R. Olivato, R. Rittner, “Conformatinal and electronic interaction studies of some a-mono-heterosubstituted carbonyl compounds”, *Rev. Heteroat. Chem.*, 1996, **15**, 115-159.

[43] R. Sahnoun, Y. Fujimura, K. Kabuto, Y. Takeuchi, R. Noyori, “Hyperconjugative electron-delocalization mechanism controlling the conformational preference of fluoroacetaldehyde and methyl fluoroacetate”, *Bull. Chem. Soc. Jpn.*, 2006, **79(4)**, 555-560.

[44] B.C. Fiorin, E.A. Basso, C.F. Tormena, R. Rittner, R.J. Abraham, “Theoretical and Experimental Investigation on the Rotational Isomerism in a-Fluoroacetophenones”, *J. Phys. Chem. A*, 2009, **113(12)**, 2906-2913.

[45] R.A. Nyquist, *Interpreting Infrared, Raman, and Nuclear Magnetic Resonance Spectra, Academic Press*, 2001.

[46] Ö. Farkas, S.J. Salpietro, P. Császár, I.G. Csizmadia, "Conformations of ethylbenzene (CH3--CH2-Ph). An ab initio study", *J. Mol. Structure (Theochem*), 1996, **367**, 25-31.

[47] G. Cinacchi, G. Prampolini, "DFT Study of the Torsional Potential in Ethylbenzene and Ethoxybenzene: The Smallest Prototypes of Alkyl- and Alkoxy-Aryl Mesogens", *J. Phys. Chem. A*, 2003, **107**, 5228-5232.

[48] J.G. Kirkwood, "Theory of Solutions of Molecules Containing Widely Separated Charges with Special Application to Zwitterions", *J. Chem. Phys.*, 1934, **2**, 351-361.

[49] L. Onsager, "Electric Moments of Molecules in Liquids", *J. Am. Chem. Soc.*, 1936, 58**(8)**, 1486–1493.

[50] M.W. Schmidt, T.L. Windus, M.S. Gordon, "Structural Trends in Silicon Atranes", *J. Am. Chem. Soc.*, 1995, **117(28)**, 7480–7486.

[51] M.M. Knopp, L. Tajber, Y. Tian, N.E. Olesen, D.S. Jones, A. Kozyra, K. Löbmann, K. Paluch, C.M. Brennan, R. Holm, A.M. Healy, G. Andrews, T. Rades, "Comparative Study of Different Methods for the Prediction of Drug−Polymer Solubility", *Mol. Pharm.*, 2015, **12**, 3408−3419.

[52] M. Maus, W. Rettig, D. Bonafoux, R. Lapouyade, "Photoinduced Intramolecular Charge Transfer in a Series of Differently Twisted Donor-Acceptor Biphenyls As Revealed by Fluorescence", *J. Phys. Chem. A*, 1999, **103**, 3388-3401.

[53] G. Zapata-Torres, B.K. Cassels, J. Parra-Mouchet, Y. Mascarenhas, J. Ellena, A.S. De Araujo, "Quantum-chemical, NMR and X-ray diffraction studies on (±)-1-[3,4-(methylenedioxy)phenyl]-2-methylaminopropane", *J. Mol. Graph. Model.*, 2008, **26**, 1296–1305.

[54] A. Makriyannis, J. Knittel, “Conformational studies on phenethylamine hallucinogens: The Role of Alpha Alkyl Substitution”, *NIDA Research Monograph 22: QuaSAR. Quantitative Structure Activity Relationships of Analgesics, Narcotic Antagonists, and Hallucinogens, G. Barnett, M. Trsic, R. E. Willette, Edits., New York*, 1978, 464–478.

[55] K.V. Ramiah, V.V. Chalapathi, “Infrared spectroscopic studies of amides and anilides”, *Proc. Indian Acad. Sci.*, 1963, **58(4)**, 233–243.

[56] S. Jiang, L. Zhang, D. Cui, Z. Yao, B. Gao, J. Lin, D. Wei, “The Important Role of Halogen Bond in Substrate Selectivity of Enzymatic Catalysis”, *Sci. Re*, 2016, **6**, 34750.

[57] M. Johansson, M. Swart, “Intramolecular halogen–halogen bonds?”, *Phys. Chem. Chem. Phys.*, 2013, **15**, 11543--11553 .

[58] G. Cavallo, Metrangolo, R. Milani, T. Pilati, A. Priimagi, G. Resnati, G. Terraneo, “The Halogen Bond”, *Chem. Rev.*, 2016, **116**, 2478−2601.

[59] C. Reichardt, T. Welton, *Solvents and Solvent Effects in Organic Chemistry, Weinheim: Wiley*, 2011.

Chapter 2.2.

Miscibility, Interactions and Antimicrobial Activity of Poly(ε-caprolactone)/Chloramphenicol Blends

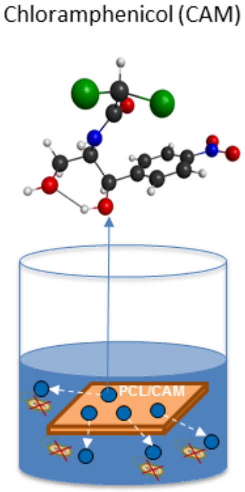
Chloramphenicol (CAM)
PCL/CAM

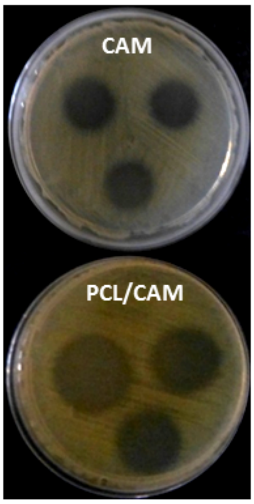

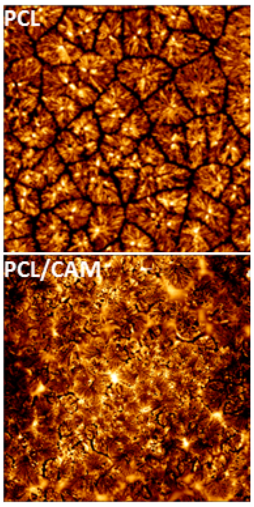

Summary

Poly(ε-caprolactone) (PCL) has been blended with Chloramphenicol (CAM), a well-known bacteriostatic antibiotic, in order to obtain new biomaterials with antibacterial properties. The resulting samples have been thoroughly characterized regarding both their physicochemical behavior and antimicrobial efficacy by means of very diverse techniques. Hence, PCL/CAM blend miscibility has been analyzed by Differential Scanning Calorimetry (DSC) using the single intermediate criterion. In turn, the interaction parameter has been obtained from the analysis of the melting point depression in both PCL rich and CAM rich blends. Fourier-Transform Infra-Red (FTIR) spectroscopy and X-Ray Diffraction (XRD) analysis have been used -in the pure components and in the blends- to analyze both the specific interactions and the crystallization behavior, respectively. The morphology of PCL/CAM blends obtained by spin-coating has been also studied by means of Atomic Force Microscopy (AFM). Finally, drug release kinetics of different PCL/CAM systems as well as their antibacterial efficacy against *Escherichia Coli* have been investigated, indicating that CAM can be released from the PCL/CAM blends in a controlled way while keeping intact the antibacterial efficiency.

2.2.1. Introduction

A controlled drug-delivery device is that able to deliver the drug at the desired release rate and duration, thus maintaining the drug level in the body within the therapeutic window (see Fig. 2.2.1). Upon intake, drug molecules must be dissolved in aqueous-based gastrointestinal fluids in a sufficient quantity as to reach their whatsoever therapeutic effect. Nevertheless, most drugs are in crystalline form, which implies auto-association interactions and low water solubility [1]. A successful strategy to improve the solubility of poorly soluble drugs is to dispense the drug in the form of amorphous solid dispersions (ASDs).

The dispersion of a drug into a polymeric matrix enables the establishment of strong specific interactions with its functional groups. Thus, the chemical potential of the drug in the amorphous phase is reduced, and as a result, its crystallization can be hindered. In other words, miscibility between the two components should favor the formation of ASDs, preventing the crystallization of the drug, and as a result, enhancing its solubility [2]. The drug release mechanism from a polymer depends on parameters such as the nature of the polymer, matrix geometry, drug-related properties, initial drug loading, and drug–matrix interactions. If, in addition, a medical device is made of a biodegradable polymer, it does not have to be removed after finishing its task. Furthermore, in a biopolymer-drug system the control of the degradation rate of the biopolymer enables the control of the drug release from the matrix. Consequently, biopolymer-drug systems are appropriate for drug delivery applications.

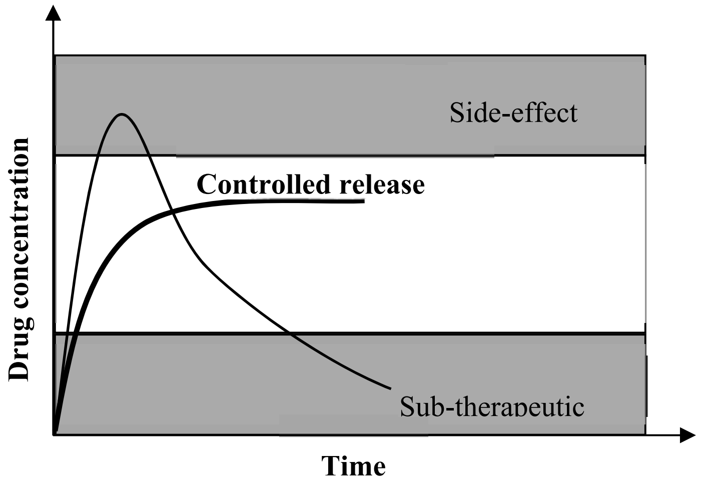

Figure 2.2.1. A comparison of conventional drug delivery profile vs. a controlled drug release profile.

In this regard, Poly(ε-caprolactone) (PCL) is one of the most promising biodegradable polymers and is already widely used in biomedical applications. PCL is suitable for long-term biomedical applications since its degradation can last from several months to years [3]. In turn, Chloramphenicol (CAM) is a broad-spectrum bacteriostatic antibiotic, which diffuses through the bacterial cell and binds to 50S ribosomal subunit. Such interaction induces inhibition of the bacterial protein synthesis as well as the blocking of bacterial cell proliferation. A wide range of microorganisms can be effectively treated by CAM; for example, it is useful in the treatment of staphylococcal brain abscesses due to an excellent blood-barrier penetration or meningitis caused by *Enterococcus faecium*. Its employment has also been shown to be effective in treating ocular infections caused by a number of bacteria including Staphylococcus aureus, *Streptococcus pneumoniae* and *Escherichia coli* [4]. As main disadvantage CAM shows low aqueous solubility.

Considering the respective chemical structures of the two species under study (see Fig. 2.2.2), hydrogen bonding can be expected to be formed between the hydroxyl groups of CAM and the carbonyl groups of PCL. In this paper, the miscibility of the PCL/CAM blends is analyzed using the criterion of the single intermediate glass transition temperature (T_g), while the strength of the resulting intermolecular interactions is evaluated from the interaction parameter. FTIR spectroscopy is then used to analyze the specific interactions responsible for the miscibility of the blends. Moreover, morphological changes in the blends are discussed in terms of PCL/CAM intermolecular interactions through the analysis of the spherulitic growt.h by means of AFM. The suitability of the blends for biomedical applications has been analyzed by investigating the release kinetics of CAM in PBS solution at 37 ºC, as well as by analyzing the antibacterial efficacy of the PCL/CAM blends against *Escherichia Coli* conducting the agar diffusion test. *E. Coli* is a gram-negative etiologic agent associated with biofilm formation on implants and susceptible to chloramphenicol treatment. The results obtained by these techniques show that CAM can be released in a controlled way from the PCL/CAM blends.

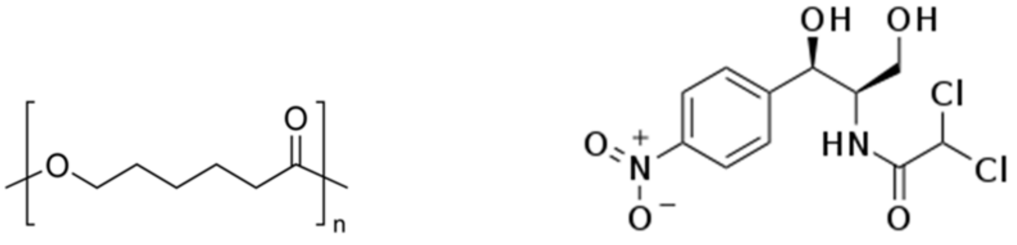

Poly(ε-caprolactone) Chloramphenicol

Figure 2.2.2. Chemical structures of PCL and CAM.

2.2.2. Experimental Section

2.2.2.1. Starting Materials

Poly(ε-caprolactone) (PURASORB® PC12 trade name) with an average molecular weight (M_w) of $1.3 \cdot 10^5$ g mol^{-1} and $M_w/M_n = 1.76$ (as determined by GPC) was obtained from Purac Biochem (The Netherlands). Chloramphenicol (purity ≥ 98 %) and Phosphate Buffered Saline (PBS) solution 1 M (pH 7.4) were supplied by Aldrich Chemical Corp. (Spain). *Escherichia coli* (ATCC 1655) was purchased from ATCC (Virginia, USA).

2.2.2.2 Blend Preparation

Films were prepared by casting from tetrahydrofuran (THF) solutions at room temperature. Films 100 μm thick were prepared by casting from 2.7 wt.% solutions into 60 mm diameter Petri dishes, and films 800 nm thick were obtained by spin-coating onto glass substrates from 10 mg/mL solutions using a spin-coater (Schaefer Tech) operating at 1000 rpm for 60 s.

2.2.2.3. Differential Scanning Calorimetry (DSC)

Thermal analyses were conducted on a Modulated DSC Q200 from TA Instruments. All the scans were carried out in hermetic aluminum pans under nitrogen atmosphere with sample weights between 5 and 10 mg. In order to study the glass transition temperatures, two consecutive scans were performed from -80 ºC to 180 ºC with a scan rate of 20 ºC/min, ensuring complete melting of the sample. Glass transition temperatures (T_g) were measured in the second scan as the midpoint of the specific heat increment.

2.2.2.4. Melting Point Depression

The melting point depression of CAM was investigated from CAM-rich blends containing 100-70 wt.% CAM. Samples were heated in the DSC with a scan rate of 1 ºC/min to obtain the melting temperature of the CAM crystals. No weight loss was observed during the thermal treatments.

The melting point depression of PCL was analyzed from PCL/CAM blends containing 100-80 wt.% PCL. Samples were first heated at 180 ºC for 3 min to assure complete melting of the PCL and CAM crystals, and then cooled at 10 ºC/min to the desired crystallization temperatures (T_c) allowing to crystallize isothermally for 60 min. Then, they were heated to 180ºC to obtain the melting points with a scan rate of 10 ºC/min.

2.2.2.5. Fourier Transform Infrared Spectroscopy (FTIR)

FTIR spectra were recorded on a Nicolet AVATAR 370 Fourier transform infrared spectrophotometer. Spectra were taken with a resolution of 2 cm^{-1} and were averaged over 64 scans in the 4000-450 cm^{-1} range. Tetrahydrofuran solutions (1.1 wt.%) were cast on KBr pellets by evaporation of the solvent at room temperature. Traces of tetrahydrofuran were removed placing the films into a heated vacuum oven for 24 h. The absorbance of the samples was within the range where the Lambert-Beer law is obeyed. A controlled high temperature transmission cell mounted in the spectrometer was used to obtain the spectra of molten samples. Second derivative spectra were smoothed using the Norris-Williams Gap Derivatives [5] using maximum gap sizes and segment lengths of 5 points and 5 cm^{-1} respectively in the derivative transformations.

2.2.2.6. X-ray Diffraction (XRD)

X-ray powder diffraction patterns were collected by using a Philips X'pert PRO automatic diffractometer operating at 40 kV and 40 mA, in theta-theta configuration, secondary monochromator with Cu-Kα radiation ($\lambda = 1.5418$ Å) and a PIXcel solid state detector (active length in 2θ 3.347º). Data were collected from 5 to 50° 2θ (step size 0.026 and time per step = 700 s) at room temperature. A fixed divergence and antiscattering slit giving a constant volume of sample illumination was used.

2.2.2.7. Atomic Force Spectroscopy (AFM)

An AFM instrument Nanowizard I (JPK Instruments, Germany) was operated in air, using contact imaging mode at constant loading forces and rates. Cantilevers were calibrated before each experiment by means of the thermal tune method [6]. Silicon-nitride probes

(DNP-10, Bruker, USA) with a nominal spring constant of 0.12 N/m were used in the experiments. All images were processed using the JPK data analysis software.

2.2.2.8. In Vitro Release Studies and Release Kinetics (UV-Vis)

UV–Vis absorption spectra were recorded over wavelengths ranging from 190 to 500 nm using a Perkin Elmer Lambda 265 UV-Visible spectrophotometer. Before performing the drug release experiments, a calibration curve was obtained measuring the absorbance at a wavelength of 278 nm for solutions of chloramphenicol in 0.1 M PBS (pH 7.4) with concentrations ranging from 10 to 100 ppm. Square samples of PCL/CAM films of 1 cm^2 with a thickness of 100 μm obtained by solvent casting were immersed in 100 mL of 0.1 M PBS buffer at 37 ºC. At fixed time intervals, samples of 2 mL were taken and replaced with fresh PBS at 37 ºC. Drug concentration in solution was determined by UV spectroscopy using the calibration curve.

The release kinetics of chloramphenicol were examined considering three mathematical models [7, 8, 9]:

1. Zero order: $C_t/C_\infty = k_0 t$ (1)
2. First order: $\ln(1 - C_t/C_\infty) = -k_1 t$ (2)
3. Higuchi: $C_t/C_\infty = k_h t^{1/2}$ (3)

C_t is the cumulative amount of drug released at time t, C_∞ represents the starting amount of drug; and k_0, k_1 and k_h are constants.

2.2.2.9. Agar Diffusion Test (*E. coli*)

Square samples (1 cm^2) of PCL/CAM 50/50 and 80/20 blends obtained by solvent casting were tested for antibacterial activity. The films were placed in 3 mL PBS buffer at 37 ºC and 5 μl of the solution were taken at fixed intervals (30 min, 3 h and 24 h), and poured over Luria-Bertani (LB) agar plates containing *E.Coli*. As positive control, drops of pure chloramphenicol (1 mg/mL) were placed in the same manner on the plates. A negative control was also examined in the form of PCL film, in order to demonstrate that the PCL does not have antibacterial traits. Radius of inhibition zones were measured to evaluate the antibacterial efficacy.

2.2.3. Results and Discussion

2.2.3.1. PCL/CAM Blend Characterization

DSC Analysis of Thermal Transitions and Miscibility

When two polymeric materials are miscible, macroscopic properties of single-phase materials are expected for the blend, such as a single glass transition temperature intermediate between those of the pure components [10, 11, 12]. This intermediate T_g usually obeys the Fox equation [13]:

$$\frac{1}{T_{gb}} = \frac{w_1}{T_{g1}} + \frac{w_2}{T_{g2}} \tag{4}$$

where w_1 and w_2 are the weight fractions of components 1 and 2 respectively, T_{g1} and T_{g2} are the glass transition temperatures of the pure components, and T_{gb} is the glass transition temperature of the blend (values in Kelvin).

Figure 2.2.3a shows the first DSC traces obtained for the pure components and for different PCL/CAM blends. It can be observed that PCL is a semicrystalline polymer melting at about 65 ºC, while CAM is a crystalline solid melting at about 151 ºC. In addition, all the PCL/CAM blends display the two melting endotherms corresponding to the pure components of the blend. Furthermore, Figure 2.2.3b shows the second scan DSC curves recorded after cooling from the melt (cooling rate ~20 ºC/min) for PCL, CAM and their blends. As can be seen, fast cooled CAM results in a super cooled liquid which shows the glass transition temperature at about 32 ºC. The glass transition temperature of PCL is located at about -60 ºC. Below the T_g of CAM, molecular mobility is frozen, nucleation points are no longer formed and crystallization of the drug is inhibited [14]. Supercooling also enhances the glass transition temperature jumps observed in the second scan for the PCL/CAM blends, which show single T_gs intermediate between those of the pure components in the whole composition range. Consequently, the two components are completely miscible in the amorphous phase. As shown in Table 2.2.1, the observed T_gs are close to the values predicted by the Fox equation (Eq. 4).

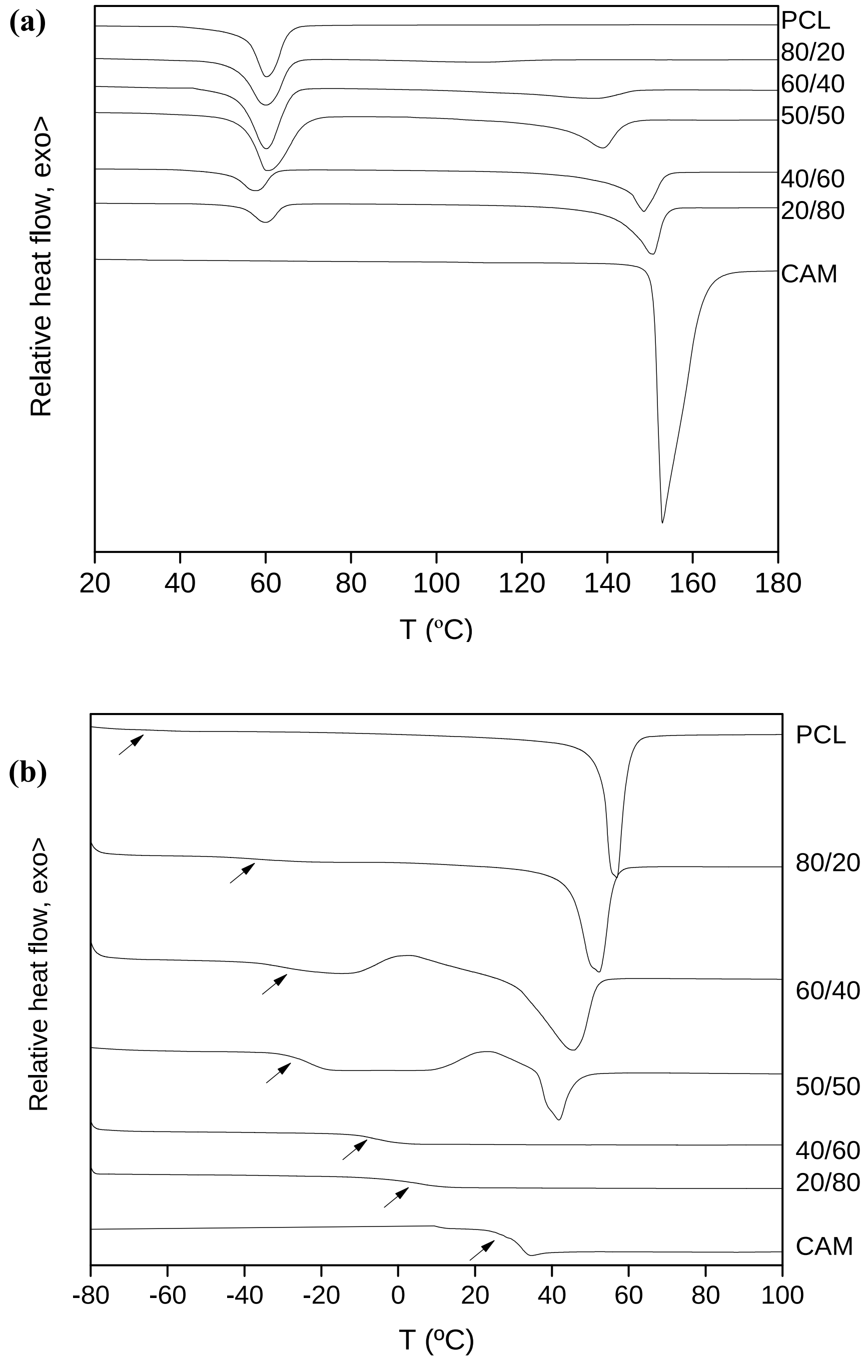

Figure 2.2.3. DSC traces for PCL, CAM and PCL/CAM blends. (a) First scan, and (b) second scan traces.

Table 2.2.1. Thermal properties of PCL/CAM blends in the second scan.

PCL/CAM	T_g experimental °C	T_g (calculated, Fox) °C	T_m PCL °C	ΔH_m PCL J/g
PCL	-60	-	57.2	66.4
80/20	-36	-46	52.3	58.1
60/40	-32	-31	45.7	35.0
50/50	-21	-22	41.5	9.1
40/60	-7	-13	-	-
20/80	6	8	-	-
CAM	32	-	-	-

Melting Point Depression Analysis

The free energy of mixing of a polymer-drug binary system is described by the Flory-Huggins solution theory [15, 16]:

$$\frac{\Delta G_M}{kT} = \underbrace{n_{drug} \ln \phi_{drug} + n_{polymer} \ln \phi_{polymer}}_{entropic} + \underbrace{n_{drug} \phi_{polymer} \chi}_{enthalpic} \qquad (5)$$

where n is the number of molecules, ϕ is the volume fraction, χ is the Flory-Huggins interaction parameter, k is the Boltzmann constant, and T is the absolute temperature. Since the entropic contribution corresponding to the polymer can be neglected in Eq. (5), ΔG_M depends on the entropic contribution corresponding to the drug (always negative and favorable to miscibility), as well as on the enthalpic contribution ($n_{drug}\phi_{polymer}\chi$). The latter is also beneficial to miscibility when $\chi < 0$, indicating favorable interactions between the blend components.

Thermodynamically, the change in free energy at the melting point is zero ($\Delta G = \Delta H - T_m\Delta S = 0$), hence $T_m = \Delta H/\Delta S$, and since the entropy change in a miscible blend (entropy of melting plus entropy of mixing) is larger than in the pure component, the melting temperature decreases [15, 17]. The depression of the equilibrium melting point can be analyzed using Flory's relationship [16]:

$$\frac{1}{T_{me}}-\frac{1}{T_{me}^{0}}=\frac{-R}{\Delta H_{2u}}\frac{V_{2u}}{V_{1u}}\left(\frac{\ln\phi_2}{m_2}+\left(\frac{1}{m_2}-\frac{1}{m_1}\right)\phi_1+\chi_{12}\phi_1^2\right) \tag{6}$$

where T_{me}^{0} and T_{me} are, respectively, the equilibrium melting points of the pure crystallizable component and of its blends, the subscripts *1* and *2* refer to the amorphous and crystallizable components respectively, *R* is the universal gas constant, ΔH_u is the heat of fusion per mole of crystalline repeat units, V_u is the molar volume of the repeating unit, *m* is the degree of polymerization, ϕ is the volume fraction, and χ_{12} is the polymer-polymer interaction parameter.

To apply Eq. (6) to the analysis of the melting point depression of CAM (component 2), the molar volume of liquid CAM (V_2 = 220 cm^3/mol [18]) is taken as the molar volume of the lattice sites, and consequently $m_2 = 1$. In addition, the same volume can be adopted as the molar volume of the polymeric repeat unit ($V_2 = V_{1u}$) so that $1/m_1 \approx 0$ (since $m_1 = V_1/V_{1u}$ is large). Therefore, Eq. (6) simplifies to Eq. (7):

$$\frac{1}{T_m}-\frac{1}{T_m^0}=\frac{-R}{\Delta H_2}\left(ln\phi_2+\phi_1+\chi\phi_1^2\right) \tag{7}$$

The melting point of CAM has been measured at low heating rates (1 ºC/min) for the pure component and for different PCL/CAM blends (see Table 2.2.2). The average melting point of pure Chloramphenicol is T_m^o(CAM) = 150.8 ºC, and the addition of 30 wt.% PCL decreases the melting point by about 6 ºC. Using the average melting enthalpy of pure CAM (ΔH_{CAM} = 119 J/g), the data in Table 2.2.2 have been analyzed according to Eq. (7) yielding the plot in Figure 2.2.4a. The negative value obtained for χ (-0.2) confirms a thermodynamically miscible blend. Alternatively, the interaction energy density, B can be calculated at the melting temperature of CAM according to Eq. (8):

$$\chi=\frac{BV_r}{RT} \tag{8}$$

where V_r is a reference volume (in this case, $V_r = V_2 = 220$ cm^3/mol), yielding B = - 3 J/cm^3.

Table 2.2.2. Melting temperature of CAM in CAM-rich PCL/CAM blends.

CAM wt.%	**T_m (ºC)**		
	Sample 1	**Sample 2**	**Sample 3**
100	150.8	150.8	150.8
90	149.3	149.3	149.3
80	147.9	147.4	147.6
70	145.5	145.2	145.3

When equation 6 is applied to the melting point depression of a polymer ($m_2 >> 1$) in a polymer-drug system, the molar volume of the amorphous drug is usually adopted as the molar volume of the lattice cells ($m_1 = 1$), leading to:

$$\frac{1}{T_{me}} - \frac{1}{T_{me}^{0}} = \frac{-R}{\Delta H_{2u}} \frac{V_{2u}}{V_1}\left(-\phi_1 + \chi\phi_1^{2}\right) \tag{9}$$

Nevertheless, in case of polymers, morphological effects such as lamellae thinning due to the penetration of the amorphous blend partner in the interlamellar region also contribute to the observed melting point depression, and must be accounted for [19]. The usual correction is the Hoffman-Weeks (H-W) method, which allows the determination of the equilibrium melting temperature of PCL in the pure polymer and in the blends [20] (see experimental). This method assumes a linear relation between the crystallization (T_c) and melting temperatures (T_m), and T_{me} is obtained from the intersection of this line with the $T_m = T_c$ line. Figure 2.2.5 displays the H-W plots to obtain the equilibrium melting temperatures for pure PCL (T_{me}^0) and blended PCL (T_{me}), which are summarized in Table 2.2.3. The decrease in the equilibrium melting temperatures suggests the miscibility of the system.

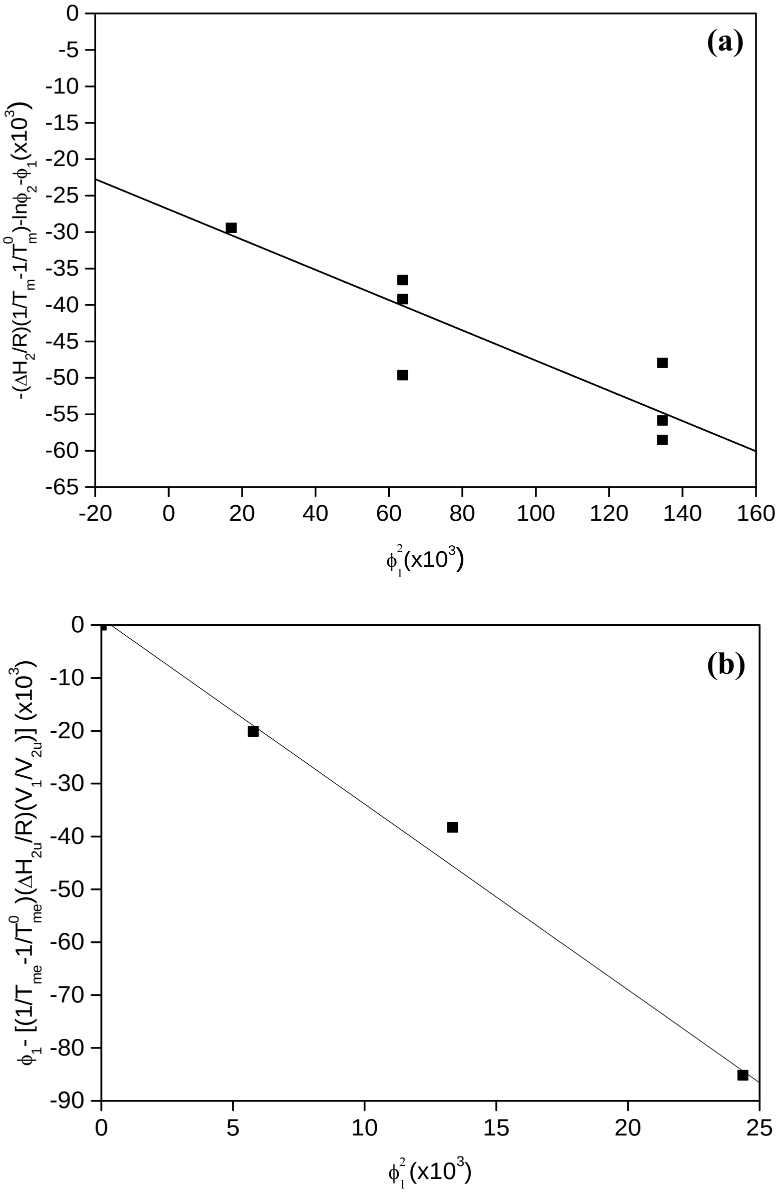

Figure 2.2.4. (a) Analysis of the melting temperature of CAM according to Eq. (7) in the presence of PCL. The slope of the plot gives the interaction parameter χ = -0.2. (b) Plot used to calculate the interaction parameter for the PCL/CAM system according to Eq. (9). The slope of the plot gives the interaction parameter χ = -3.4.

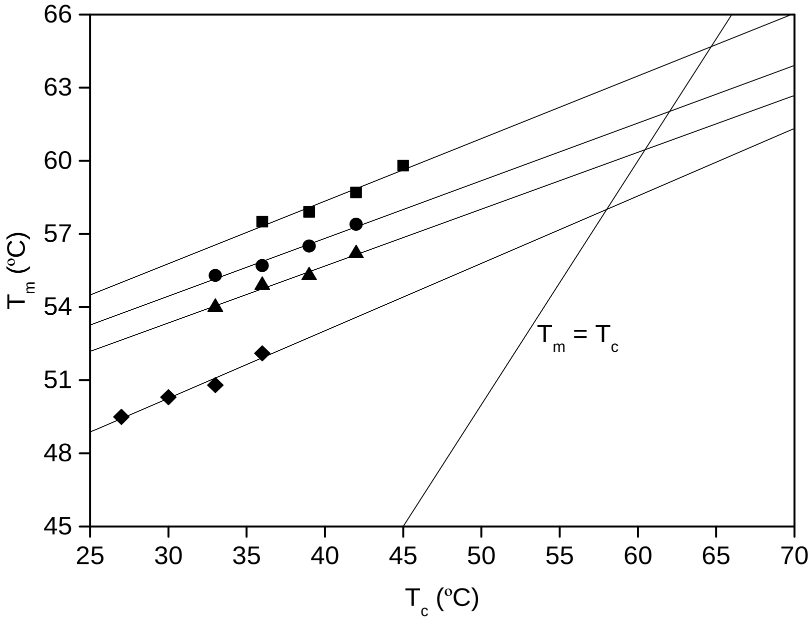

Figure 2.2.5. Hoffman-Weeks extrapolations for (■) PCL, (●) PCL/CAM 90/10, (▲) PCL/CAM 85/15, and (♦) PCL/CAM 80/20.

Table 2.2.3. Equilibrium melting temperatures (T_{me}) obtained from the H-W extrapolations.

System	T_{me} (ºC)
PCL	64.7
PCL/CAM 90/10	62.0
PCL/CAM 85/15	60.4
PCL/CAM 80/20	58.0

Figure 2.2.4b shows the analysis of the equilibrium melting temperatures according to the Flory-Huggins equation (Eq. 9). The parameters used in the calculations are V_1 = 220 cm^3/mol (CAM) [20], V_{2u} = 105 cm^3/mol and ΔH_{2u} = 140 J/g (PCL) [21]. From the slope the value obtained for the interaction parameter is $\chi = -3.4$. The negative value obtained for χ confirms a thermodynamically miscible blend.

FTIR Analysis of PCL/CAM Blends

Figure 2.2.6 shows the X-H stretching region for molten CAM and PCL/CAM blends of different composition at 160 ºC. As discussed in the previous section, pure CAM presents a peak at about 3400 cm^{-1} attributable to the N-H stretching mode of secondary amides participating in weak contacts [22]. The O-H stretching band is the broad envelope from about 3200 to 3650 cm^{-1}, indicating a broad range of interaction strengths resulting from the adoption of the distorted hydrogen bonding geometries allowing interactions with the disordered amorphous environment. In pure CAM, the maximum of the OH stretching band overlaps with the N-H stretching band, and occurs somewhere about 3450 cm^{-1}. Upon the addition of PCL to CAM, the OH stretching band shifts to higher wavenumbers, up to about 3500 cm^{-1} in the PCL rich blends. The shift to higher wavenumbers is typical of systems in which the stronger OH···OH interactions are replaced by weaker C=O···O-H interactions, and suggests the establishment of intermolecular C=O···H-O interactions at the expense of the O-H···O-H autoassociation. Notice that the PCL/CAM 40/60 blend contains approximately equimolecular amounts of PCL repeat units and CAM molecules, and therefore contains approximately equimolecular amounts of C=O and OH groups.

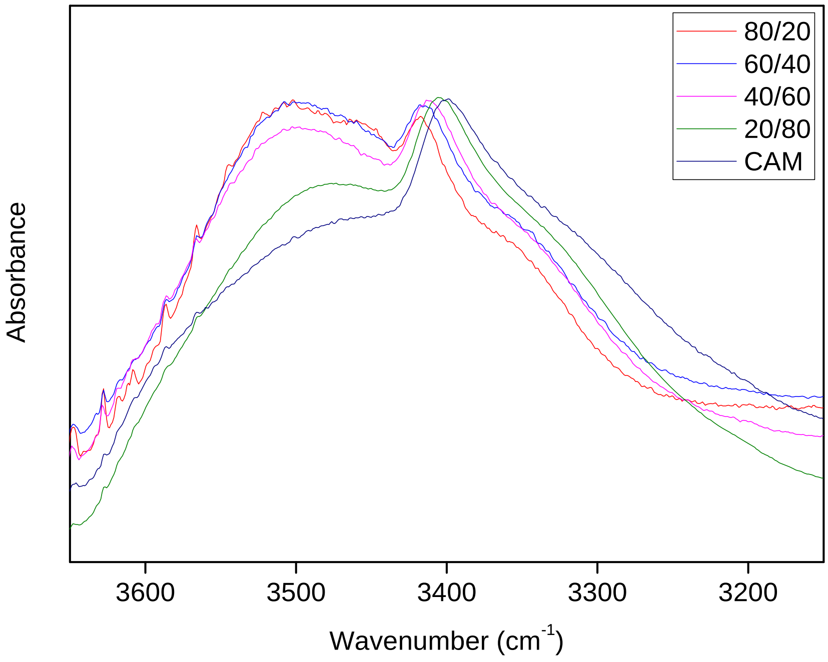

Figure 2.2.6. X-H stretching region for the PCL/CAM system at 160 ºC.

Figure 2.2.7 shows the carbonyl stretching region of the pure components and their blends in the melt (at 160 ºC). Molten PCL shows a peak at 1735 cm^{-1} attributable to free C=O groups in the amorphous phase and molten CAM shows a broad peak located at about 1688 cm^{-1} attributable to C=O groups hydrogen bonded to the hydroxyl groups present in pure CAM. As can be observed, blending increases the relative intensity at wavenumbers located between those of the pure components, suggesting the occurrence of new bands. However, the substantial overlap between the bands corresponding to the pure components makes difficult the identification of new bands in this spectral region. In order to improve spectral resolution, Norris second derivatives have been obtained for CAM and for the PCL/CAM 40/60 blend in both molten (160 ºC) and supercooled samples (40 ºC) (see Fig. 2.2.7b). The second derivative of supercooled CAM shows two components located at about 1690 and 1675 cm^{-1}, attributable to the two main conformers occurring in molten CAM which only differ in the orientation of the terminal dichloromethyl group. At 160 ºC, the second derivative spectrum of the PCL/CAM blend shows a new intermediate band located between those corresponding to free C=O groups of PCL and the hydrogen bonded C=O groups of CAM, that can be attributed to C=O groups of PCL, hydrogen bonded to hydroxyl groups of CAM. After quenching to room temperature, the locations obtained for the two PCL bands using second derivative spectroscopy are respectively 1735 and 1709 cm^{-1}. The red shift obtained for the hydrogen bonded C=O groups of PCL is therefore 24 cm^{-1}. The analysis of the C=O stretching band confirms the occurrence of C=O···H-O hydrogen bonding between PCL and CAM.

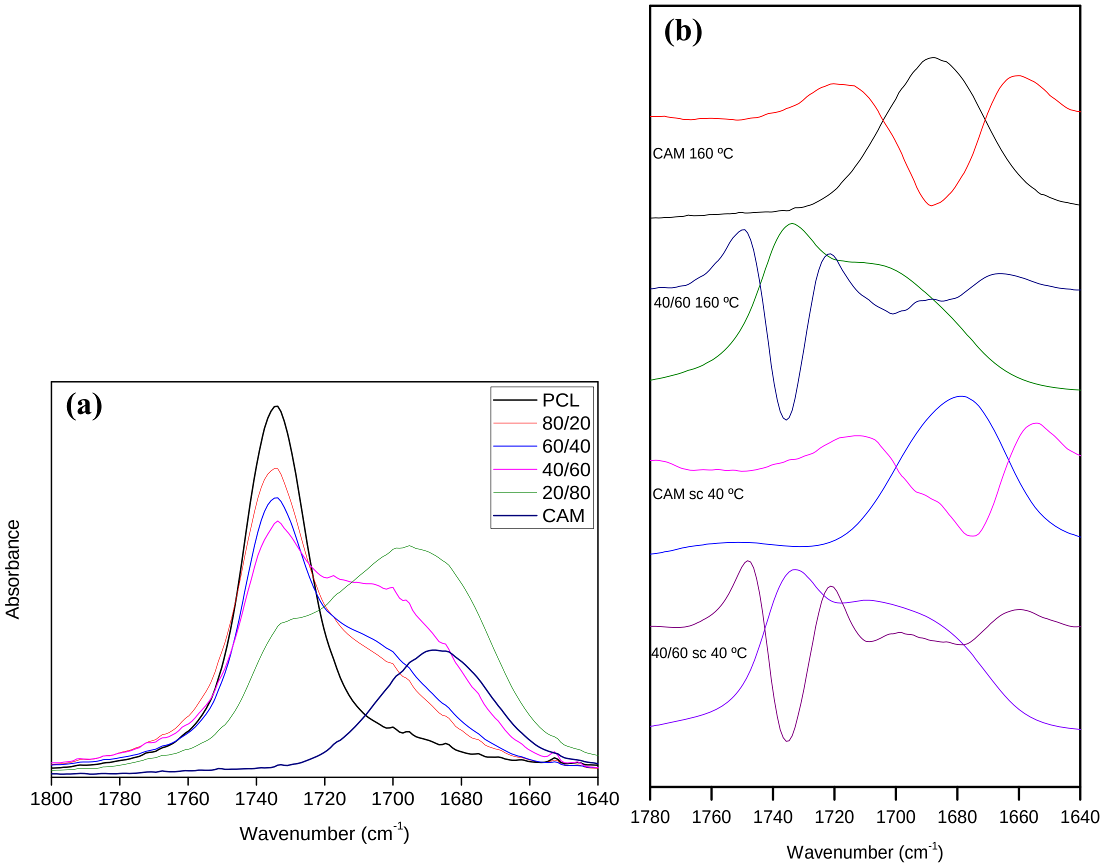

Figure 2.2.7. (a) Carbonyl stretching region for the PCL and PCL/CAM blends at 160 ºC. (b) Spectra and Norris second derivatives for CAM and for the PCL/CAM 40/60 blend in both molten (160 ºC) and supercooled samples (40 ºC).

Crystallization Behavior Based on the X-ray Diffraction Analysis

The XRD patterns of PCL, CAM and their blends are shown in Figure 2.2.8. CAM exhibits a characteristic peak at 2θ = 13º, as well as several strong peaks at 16º, 18º, 19º and 20º. As the polymer content in the blend increases, the intensity of the crystalline peaks decreases while their width increases. The width of X-ray diffraction peaks is related to the size of the crystallites, and peak widening is usually a consequence of smaller, more imperfect crystals [23]. The PCL/CAM 90/10 blend still shows tiny CAM peaks, while in the PCL/CAM 95/5 blend crystallization of CAM is completely suppressed. Hence, completely amorphous CAM (as required in amorphous solid dispersions, ASDs) can only be obtained when the CAM content is below 10 wt.%.

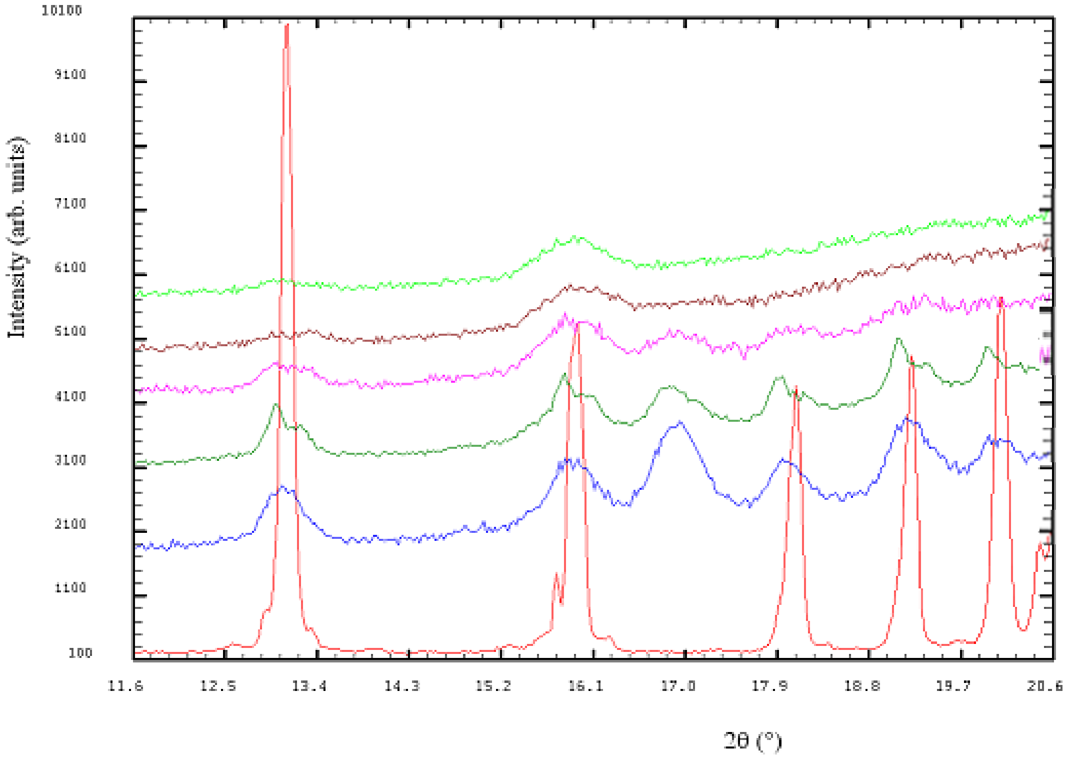

Figure 2.2.8. XRD patterns of: (a) pure PCL, (b) PCL/CAM 95/5, (c) PCL/CAM 90/10, (d) PCL/CAM 85/15, (e) PCL/CAM 80/20, and (f) pure CAM.

AFM Analysis

AFM topographic images of thin films (800 nm) of pure PCL, show the characteristic spherulitic morphology of semicrystalline polymers (Figure 2.2.9a). In the melt, PCL and CAM form a single phase, however, crystallization of PCL upon cooling creates a CAM enriched amorphous phase that is displaced by the growing crystalline phase to the interlamellar region and to the spherulitic grain boundaries [24]. As the CAM content in the blend increases, spherulitic boundaries become less defined, and the crystalline phase shows a looser, less compact morphology. The PCL/CAM 40/60 blend (Figure 2.2.9d) is a clear example of this behavior. In the PCL/CAM 20/80 blend (Figure 2.2.9e) crystallization of PCL is completely suppressed. Finally, Figure 2.2.9f shows the morphology observed in an immiscible PCL/drug blend (with erythromycin), characterized by straight interspherulitic boundaries similar to those observed in pure PCL samples.

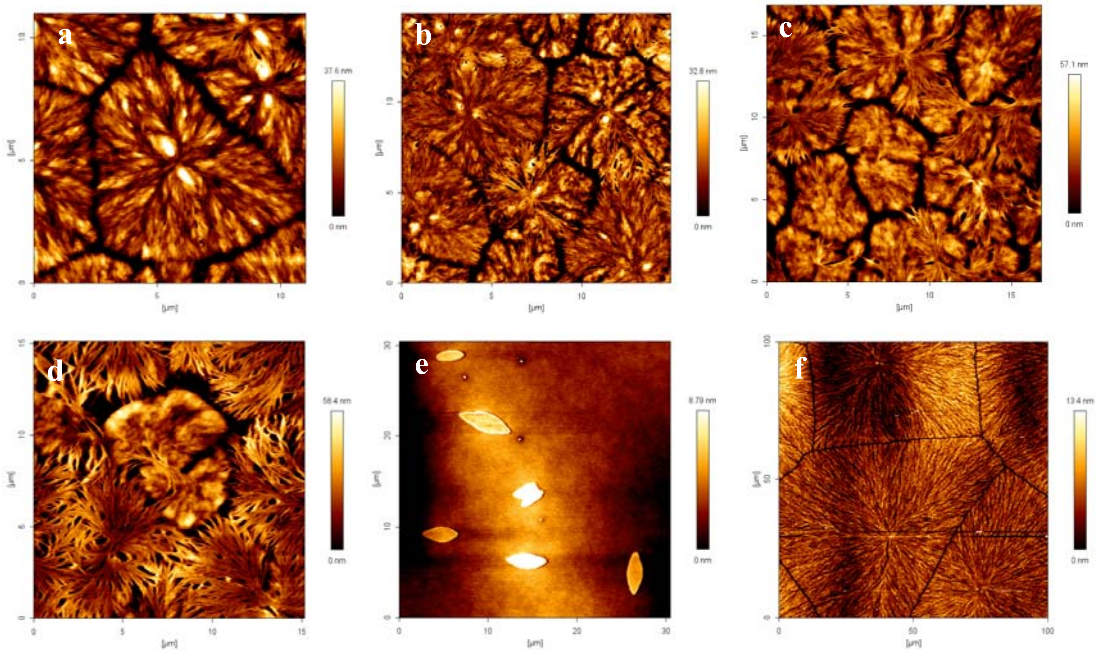

Figure 2.2.9. AFM topographic images: (a) pure PCL; (b) PCL/CAM 80/20, (c) PCL/CAM 60/40, (d) PCL/CAM 40/60, (e) PCL/CAM 20/80, and (f) PCL/Erythromycin 50/50 (immiscible). Films thicknesses were about 800 nm.

2.2.3.2. Drug Release Behavior

Figure 2.2.10 shows the in vitro drug release experiments performed for PCL/CAM 40/60, 80/20 and 95/5 blends for 7 hours (since the whole antibiotic was released within that time). Considering the release profiles of chloramphenicol coupled with the XRD results, two different release behaviors can be distinguished: one for PCL/CAM 40/60 and 80/20 blends, where part of the antibiotic is crystalline; and another one for PCL/CAM 95/5 blend, where the drug is in amorphous form. In the latter case, there is an initial burst in which 39 wt.% of the drug is released during the first 10 minutes, whereas for the other two compositions only 5 wt.% is released in the same period of time.

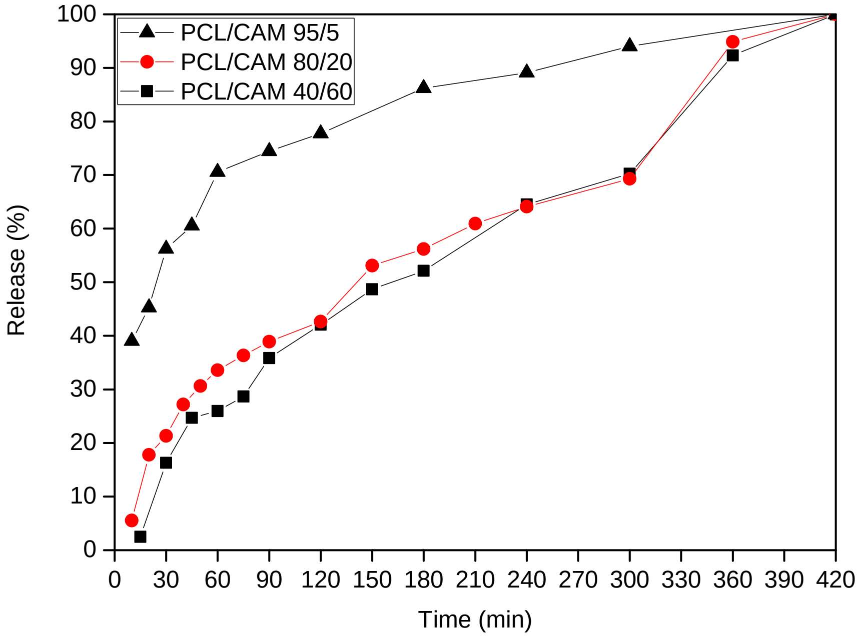

Figure 2.2.10. Drug release profile of PCL/CAM 40/60, 80/20 and 95/5 samples of 1 cm^2 with a thickness of 100 µm obtained by solvent casting, immersed into 100 mL of PBS (pH 7.4) at 37 ºC for 7 hours.

The release process starts with the penetration of the buffered solution into the polymeric matrix leading to its swelling. Consequently, the free volume of the polymeric chains increases and the polymeric network becomes looser, leading to the diffusion of the amorphous chloramphenicol through the PCL matrix into the outer solution [25]. The release data has been fitted to different kinetic equations used to study the mechanism of drug release. Regression coefficients are shown in Table 4. PCL/CAM 95/5 system follows a first order kinetics, thus, the release depends on drug concentration. There is an initial burst, because the drug is in amorphous form and then, it is released in a controlled way. Therefore, it can be a good choice in applications where it is necessary to attain rapidly the effective therapeutic concentration and to maintain it for some hours.

On the other hand, the release from PCL/CAM 80/20 and 40/60 systems fits to zero order kinetics, where the release occurs at a constant rate, independent of the drug concentration used to prepare the blend. In the zero order kinetics, the CAM crystallites act as drug reservoirs that, after the initial burst, maintain the concentration of amorphous drug dissolved in the polymeric matrix in nearly steady conditions. This release mechanism is useful for sustained drug delivery systems.

Table 2.2.4. Fitting of the release data to the mathematical models for drug release kinetics. R^2 is the correlation coefficient.

PCL/CAM	Zero order	First order	Higuchi
95/5	$R^2 = 0.804$	$R^2 = 0.976$	$R^2 = 0.931$
80/20	$R^2 = 0.972$	$R^2 = 0.797$	$R^2 = 0.961$
40/60	$R^2 = 0.982$	$R^2 = 0.87$	$R^2 = 0.971$

2.2.3.3. Bacterial inhibition assay

The agar diffusion test was carried out on PCL/CAM 80/20 and 50/50 blends, which are characterized by a constant release rate according to the preceding section. Inhibition zones were observed when the released solutions containing CAM were placed on plates with a layer of *E. Coli* (see Fig. 2.2.11 and Table 2.2.5). PCL was used as negative control, and inhibition zones could not be detected from its leachates (Fig. 2.2.11a). A CAM solution of concentration 1 mg/mL (the solubility of CAM in water at 25 ºC is 2.5 mg/mL [26]) was used as positive control, resulting in inhibition zones of average radius of 0.8 cm (Fig. 2.2.11b). In case of the PCL/CAM blends, the concentration of CAM in the leachate at different times was calculated from the kinetic models obtained in the preceding section. In all cases, the entire drug was released from the polymer after 24 h, as confirmed also by ATR spectroscopy of the final films. After 24 h, the concentration of CAM in the leachate was 0.7 mg/mL for the PCL/CAM 80/20 sample, and 1.1 mg/mL for the PCL/CAM 50/50 blend. Overall, the inhibition radii are proportional to the concentration of CAM in the solutions, indicating that CAM can be released in a controlled way from its blends with PCL, without losing antibacterial activity. Moreover, it is also known that amorphous forms possess a higher apparent solubility in comparison to their crystalline counterparts [27,28], and blending with PCL could be an interesting strategy to obtain therapeutical concentrations above the solubility limit of the drug.

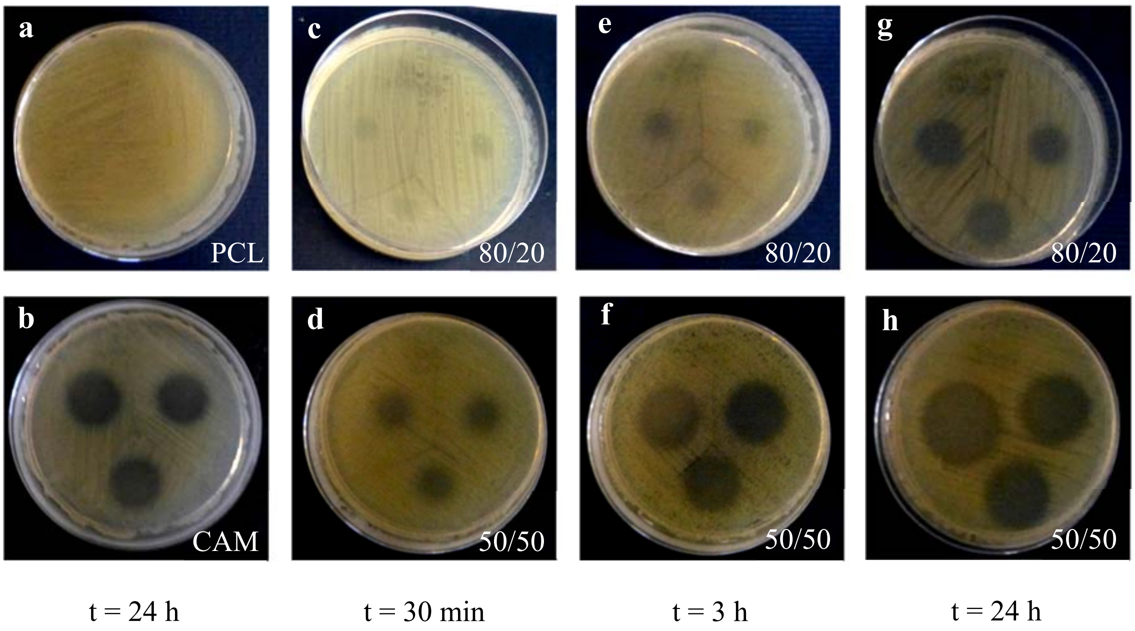

Figure 2.2.11. Images of inhibition zones created after pouring on LB agar plates with *E. Coli* 5 μl drops of the leachates obtained from (a) PCL after 24 h, (b) chloramphenicol solution of 1 mg/mL, (c) PCL/CAM 80/20 after 30 min, (d) PCL/CAM 50/50 after 30 min, (e) PCL/CAM 80/20 after 3 h, (f) PCL/CAM 50/50 after 3 h, (g) PCL/CAM 80/20 after 24 h, and (h) PCL/CAM 50/50 after 24 h.

Table 2.2.5. Average radius of the inhibition zones measured after fixed intervals, and the amount of drug released at each time.

Radius (cm)	30 min	3 h	24 h
CAM	0.8	0.8	0.8
PCL/CAM 80/20	0.4	0.5	0.8
PCL/CAM 50/50	0.5	1	1.3
% Drug released	20 %	60 %	100 %

2.2.4. Conclusions

Miscibility has been confirmed in the PCL/CAM system according to the intermediate glass transition temperature criterion. The analysis of the melting point depressions using the expression of Flory indicates negative interaction parameters for both PCL-rich and CAM-rich blends.

The analysis by FTIR spectroscopy of the PCL/CAM blends shows new bands in the C=O stretching region attributable to C=O···H-O interactions between the carbonyl groups of PCL and the hydroxyl groups of CAM. In addition, the OH stretching band of molten CAM is observed to shift to higher wavenumbers. These changes suggest the formation of new C=O···H-O interactions between PCL and CAM, mainly at the expense of the O-H···O-H interactions present in pure CAM, since reducing the number of hydroxyl-hydroxyl interactions reduces their degree of cooperativity and shifts the band to higher wavenumbers.

The analysis of the spherulitic morphology of the blends by AFM shows that the addition of CAM to PCL results in less defined spherulites, showing a laxer morphology, characteristic of miscible blends. The XRD analysis shows that the maximum CAM content in the blend to achieve an amorphous solid dispersion is about 10 wt.% CAM. Release kinetic analyses show that CAM can be completely released from the PCL/CAM films in about 7 hours in aqueous media. First order kinetics are observed for the samples containing CAM in amorphous form, and zero order kinetics for samples containing crystalline CAM. Finally, the agar diffusion test against *E. Coli* (a gram-negative bacteria associated with biofilm formation on medical devices) shows that CAM can be released in a controlled way from its blends with PCL without losing antibacterial activity.

References

[1] Y. Kawabata, K. Wada, M. Nakatani, S. Yamada, S. Onoue, “Formulation design for poorly water-soluble drugs based on biopharmaceutics”, *Int. J. Pharm.*, 2011, **420**, 1-10.

[2] N. Shah, H. Sandhu, D.S. Choi, H. Chokshi, A. Malick, “Amorphous Solid Dispersions. Theory and Practice”*, New York: Springer*, 2014.

[3] M. Labet, W. Thielemans, “Synthesis of polycaprolactone: a review”, *Chem. Soc. Rev.*, 2009, **38**, 3484–3504.

[4] S. Kalita, B. Devi, R. Kandimalla, K.K. Sharma, A. Sharma, K. Kalita, A.C. Kataki, J. Kotoky, “Chloramphenicol encapsulated in poly-e-caprolactone-pluronic composite: nanoparticles for treatment of MRSA-infected burn wounds”, *Int. J. Nanomedicine*, 2015, **10**, 2971-2984.

[5] K.H. Norris, P.C. Williams, “Optimization of Mathematical Treatments of Raw Near-Infrared Signal in the Measurement of Protein in Hard Red Spring Wheat. I. Influence of Particle Size”, *Cereal Chem.*, 1984, **61(2)**, 158–165.

[6] J.L. Hutter, J. Bechhoefer, “Calibration of atomic-force microscope tips”, Rev. *Sci. Instrum.*, 1993, **64(7)**, 1868-1873.

[7] J.S. Boateng, K.H. Matthews, A.D. Auffret, M.J. Humphrey, H.N. Stevens, G.M. Eccleston, “In vitro drug release studies of polymeric freeze-dried wafers and solvent-cast films using paracetamol as a model soluble drug”, *Int. J. Pharm.*, 2009, **378**, 66-72.

[8] T. Higuchi, “Mechanism of sustained-action medication. Theoretical analysis of rate of release of solid drug dispersed in solid matrices”, *J. Pharm. Sci.*, 1963, **52(12)**, 1145-1149.

[9] S. Khan, H. Batchelor, P. Hanson, I.Y. Saleem, Y. Perrie, A.R. Mohammed, “Dissolution rate enhancement, in vitro evaluation and investigation of drug release

kinetics of chloramphenicol and sulphamethoxazole solid dispersions", *Drug Develop. Ind. Pharm.*, 2013, **39(5)**, 704-715.

[10] N. Hernandez-Montero, E. Meaurio, K. Elmiloudi, J.R. Sarasua, "Novel miscible blends of poly(p-dioxanone) with poly(vinyl phenol)", *Eur. Polym. J.*, 2012, **48**, 1455–1465.

[11] A. Lejardi, J.R. Sarasua, A. Etxeberria, E. Meaurio, "Miscible Blends of Poly(ethylene oxide) with Brush Copolymers of Poly(vinyl alcohol)-graft-poly(L-lactide)", *J. Polym. Sci. B*, 2016, **54**, 1217–1226.

[12] E. Meaurio, E. Zuza, J.R. Sarasua, "Miscibility and specific interactions in blends of poly(L-lactide) with poly(vinylphenol)", *Macromolecules*, 2005, **38(4)**, 1207-1215.

[13] T.G. Fox, "Influence of diluent and of copolymer composition on the glass temperature of a polymer system", *Bull. Am. Phys. Soc.*, 1956, **1**, 123-132.

[14] J. Kerc, S. Srcic, "Thermal analysis of glassy pharmaceuticals", Thermochim*. Acta*, 1995, **248**, 81-95.

[15] E. Meaurio, N. Hernandez-Montero, E. Zuza, J.R. Sarasua, "Miscible blends based on biodegradable polymers", *Characterization of Polymer Blends: Miscibility, Morphology and Interfaces, 1, S. Thomas, Y. Grohens and P. Jyotishkuma, Edits., Weinheim, Wiley*, 2015, 7–92.

[16] P.J. Flory, "Principles of Polymer Chemistry", *New York: Cornell University Press*, 1953.

[17] L.M. Robenson, "Polymer Blends. A comprehensive review", *Hanser*, 2007.

[18] M. M. Knopp, L. Tajber, Y. Tian, N. E. Olesen, D. S. Jones, A. Kozyra, K. Löbmann, K. Paluch, C. M. Brennan, R. Holm, A. M. Healy, G. P. Andrews, T. Rades, "Comparative Study of Different Methods for the Prediction of Drug−Polymer Solubility", *Mol. Pharm.*, 2015, **12**, 3408−3419.

[19] D. Rohindra, "Miscibility determination in poly(e-caprolactone)/poly(vinil formal) blend by equilibrium melting temperature and spherulite morphology", *J. Macromol. Sci. B*, 2009, **48**, 1103-1113.

[20] M. Al-Hussein, G. Strobl, "The Melting Line, the Crystallization Line, and the Equilibrium Melting Temperature of Isotactic Polystyrene", Macromolecules, 2002, **35**, 1672–1676.

[21] L. Mandelkern, *Crystallization of Polymers, 2 ed., 1, New York: Cambridge University Press*, 2002.

[22] D. Sajan, G.D. Sockalingum, M. Manfait, I. Hubert Joe, V.S. Jayakumar, "NIR-FT Raman, FT-IR and surface-enhanced Raman scattering spectra, with theoretical simulations on chloramphenicol", *J. Raman Spectrosc.*, 2008, **39**, 1772-1783.

[23] J. Jingou, H. Shilei, L. Weiqi, W. Danjun, W. Tengfei, X. Yi, "Preparation, characterization of hydrophilic and hydrophobic drug in combine loaded chitosan/cyclodextrin nanoparticles and in vitro release study", *Colloids Surf. B*, **201(83)**, 103–107.

[24] C. Hou, T. Yang, X. Sun, Z. Ren, H. Li, S. Yan, "Branched crystalline patterns of poly(e-caprolactone) and poly(4-hydroxystyrene) blends thin films", *J. Phys. Chem. B*, 2016, **120**, 222-230.

[25] J. Siepmann, N.A. Peppas, "Modeling of drug release from delivery systems based on hydroxypropyl methylcellulose (HPMC)", *Adv. Drug Deliv. Rev.*, 2001, **48**, 139-157.

[26] D. Szulczewski, F. Eng, "Chloramphenicol", *Analytical Profiles of Drug Substances, K. Florey, Ed., Academic Press*, 1975, 47-90.

[27] S.B. Teja, S.P. Patil, G. Shete, S. Patel, A.K. Bansal, "Drug-excipient behavior in polymeric amorphous solid dispersions", *J. Excipients Food Chem.*, 2013, **4(3)**, 70-94.

[28] B.C. Hancock, M. Parks, "What is the true solubility advantage for amorphous pharmaceuticals?", *Pharm. Res.*, 2000, **17(4)**, 397-404.

Chapter 3

Miscibility, Interactions and Drug Release Kinetics Investigation in Poly(ε-caprolactone)/Quercetin Blends

Summary

Miscibility and specific interactions between poly(ε-caprolactone) (PCL) and Quercetin (Q) are investigated for the purpose of obtaining a miscible polymer/drug system to cope with the high crystallinity and low bioavailability of the flavonoid. PCL/Q blends were prepared using different methods for the fabrication of various drug release platforms: solvent casting for micrometric films, spin coating for nanometric films, and electrospinning for mats composed of micro and nanofibers. The miscibility and interactions were analyzed by means of DSC, ATR-FTIR and AFM. A single intermediate glass transition temperature (T_g) confirms the miscibility in PCL-rich blends. Through the study of carbonyl and hydroxyl stretching regions of the infrared spectra for PCL/Q blends, hydrogen bonding interactions have been found (-C=O···H-O-). Then, morphologies of thin films obtained by spin coating have been studied through atomic force microscopy, in order to analyze how specific interactions, as well as the spinning speed affect the shape of PCL crystals. Finally, drug release kinetics for different PCL/Q systems have been studied in PBS buffer solution at 37 ºC under inert atmosphere in order to displace oxygen and to avoid the oxidation of quercetin. In contrast to the micrometric PCL/Q films, where part of the quercetin remains within the polymeric matrix, in films 1,000 times thinner the whole drug is released by diffusion, and the release mechanism is different depending on the composition, and hence, on the interactions established. When comparing the drug release from films to scaffolds with the same composition and thickness, the difference is originated by the pore size: larger pores contribute to the release, due to the superficial area to volume relationship. The PCL/Q system is found to allow the design of versatile drug eluting devices.

3.1. Introduction

Onions, tea, strawberries, apples, grapes, parsley, and many spices are just a few natural foods rich in flavonoids. Flavonoids are a group of polyphenolic compounds synthesized by plants, which have inhibitory activity against organisms that cause plant diseases. They have recently gained interest, owing to their potential health benefits arising from their antioxidant activity. It has been studied that the functional hydroxyl groups found in flavonoids have the ability to scavenge free radicals, as well as to induce human protective enzyme systems. Numerous investigations have suggested protective effects of flavonoids against many infectious and degenerative illnesses such as cardiovascular diseases, and other age-related disorders [1].

Quercetin (Q) is a flavonoid present in fruits and vegetables, and it was selected due to its anti-oxidant and anti-inflammatory properties. As a drawback, it easily oxidizes in aqueous aerobic environments such as body fluids, and it is poorly absorbed in the gastrointestinal tract [2]. Quercetin is especially crystalline, meaning that the energy needed to break the intermolecular interactions within its natural crystalline network is high enough that water will not effectively dissolve it. Furthermore, the bioavailability of quercetin through oral dose has been reported to be around 2% [3].

A good strategy to overcome shortcomings associated with the quercetin (poor solubility, physiochemical instability, reduced bioavailability and short half-life) is the formulation of amorphous solid dispersions (ASDs). In ASDs, polymer chains act as crystallization inhibitor preserving the drug in amorphous form. Although the amorphous form is actually less stable than the crystalline one, it can be stabilized to some extent by weak physical interactions with the polymeric matrix (see Fig. 3.1). Drugs in the amorphous state have a better solubility in aqueous environment, and can subsequently be absorbed by the body in sufficient quantity to have therapeutic effect [4]. Polyesters are a good choice to formulate ASDs with hydroxyl-bearing drugs because they possess ester groups that are able to establish C=O···O-H hydrogen bonding interactions with the drug and stabilize it in the amorphous form [5]. Poly(ε-caprolactone) (PCL) is one of the most promising biodegradable polyesters which is widely used for biomedical applications. Its degradation can last from several months to years, which make it suitable for long-term biomedical applications [6].

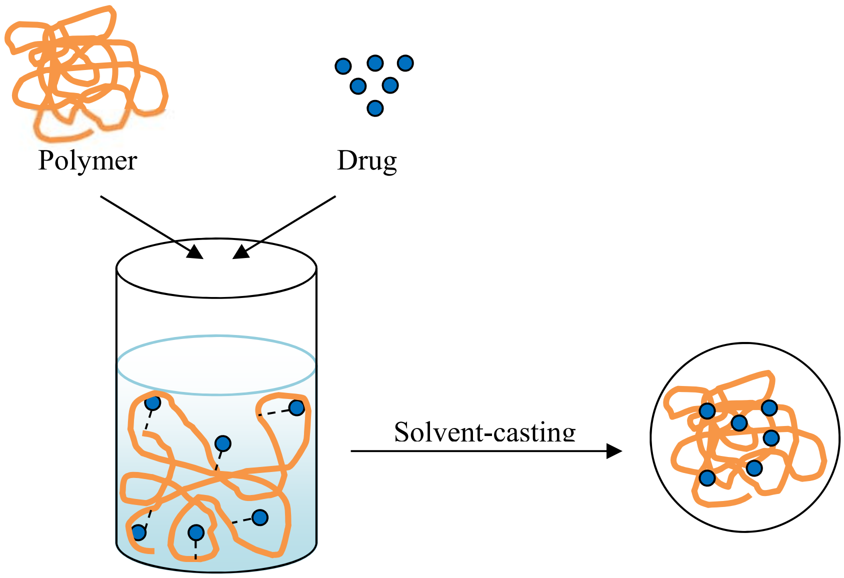

Figure 3.1. Amorphous solid dispersion (ASD).

Miscible polymer-flavonoid systems where interactions are formed between the two species would allow the formation of ASDs, preventing the crystallization of the flavonoid [7]. Considering the chemical structures of the two species under study (see Fig. 3.2), hydrogen bonding between the hydroxyl groups of quercetin and the carbonyl groups of PCL can be expected, and those interactions should overcome the strong autoassociation interactions occurring between the quercetin molecules in the crystalline phase. Thus, throughout this chapter, miscibility and interactions of PCL/Q blends, as well as release kinetics of quercetin from different polymeric platforms will be investigated. The combination of the unique properties of antioxidant quercetin molecules with the versatility of a biopolymer such as the PCL, can lead to a sustained activity of the flavonoid against several diseases from medical devices with different designs.

The miscibility of the PCL/Q blends was studied through the criterion of the single intermediate glass transition temperature (T_g), and the specific interactions between the two species were established using ATR-FTIR spectroscopy. It should be noted that the quercetin is unstable when exposed to UV-irradiation, electrochemical oxidation, enzyme catalyzed oxidation, but also to atmospheric or aqueous oxygen. The oxidative degradation reduces the pharmacological efficiency of this antioxidant and makes analytical determination more difficult [8]. Since the quercetin is a molecule that oxidizes rapidly in aqueous aerobic environments, we removed the oxygen of the PBS buffer solution used to investigate the release mechanism of this flavonoid by recirculating nitrogen.

Then, quartz crystal microbalance with dissipation monitoring (QCM-D) was used to study the release in thin films (~ 200 nm) through the analysis of the increase in the frequency related to the mass loss, as well as to compare the release behavior with films 1,000 times thicker studied by means of UV-Vis spectroscopy. Moreover, just like Vashisth et al. [9] reported using PLGA-PCL nanofibers, we were also able to encapsulate quercetin in PCL fibers to study the effect of the 3D structure on the release. For this aim, three different platforms with 10% quercetin content were evaluated by means of UV-Vis absorption spectroscopy: a film and two electrospun mats, one of them formed by nanofibers and the other composed by a heterogeneous distribution of micro- and nanofibers. The results obtained by these techniques show that different platforms can be obtained for a controlled release of the quercetin from the PCL/Q blends suitable for different applications.

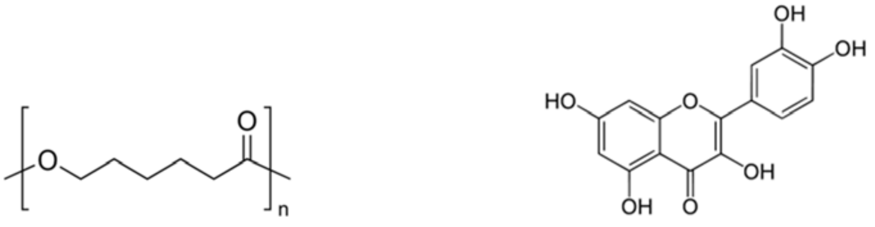

Poly(ε-caprolactone)　　Quercetin

Figure 3.2. Chemical structures of PCL and Quercetin.

3.2. Experimental Section

3.2.1. Starting Materials

Polycaprolactone (PURASORB® PC12 trade name) with an average molecular weight (M_W) of $1.3 \cdot 10^5$ g mol^{-1} and $M_W/M_n = 1.76$ (as determined by GPC) was obtained from Purac Biochem (The Netherlands). Quercetin (purity ≥ 95 %), formic acid, and phosphate buffered saline (PBS) 1 M, pH 7.4, were supplied by Aldrich Chemical Corp. (Spain). Tetrahydrofuran (THF) and 2.2.2-trifluoroethanol (TFE) were purchased from Labkem.

3.2.2. Blend Preparation

Films

Films 200 µm thick were prepared by casting from 2 wt.% tetrahydrofuran (THF) solutions at room temperature into 40 mm diameter dishes. Nanometric films were obtained by spin coating onto glass substrates from 10 mg/mL solutions using a spin-coater (Schaefer Tech) operating at 1000 rpm for films 800 nm thick, and at 3600 rpm onto QCM sensors for 200 nm thick films. With the intention of making a correlation between film thickness and spinning speed, drops of PCL solution were deposited during 60 s on the glass substrates after setting the spin coating machine to a specific speed: 500, 1000, 2000 and 3600 rpm. Then, the thickness of the films obtained at different speeds was assessed removing part of the material with acetone and quantifying the step by means of AFM (see Fig. 3.3a). The correlation between film thickness and spinning speed, as well as the spherulitic morphology for thin films of different dimensions, are shown in the Figure 3.3b.

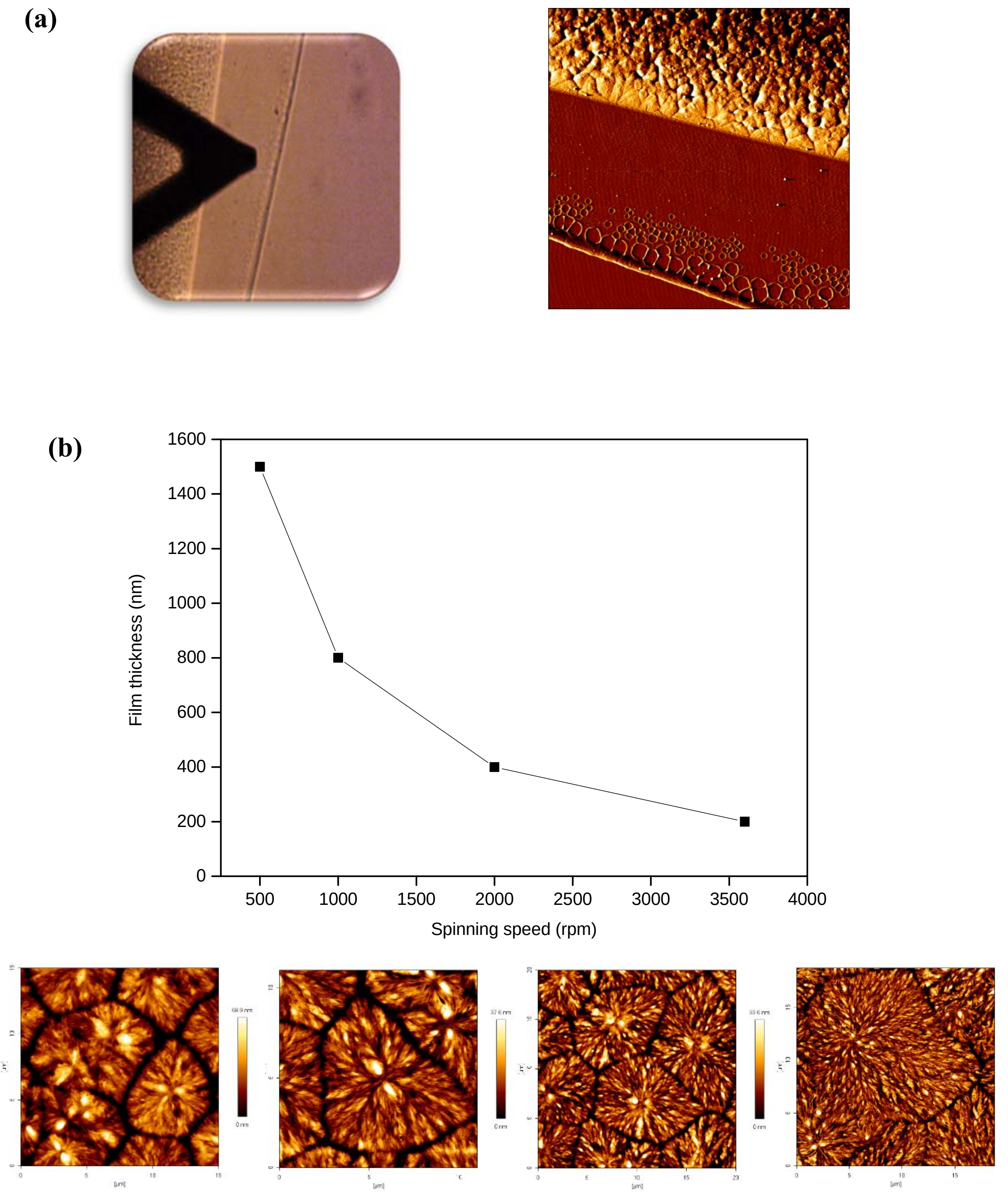

500 rpm → 1500 nm 1000 rpm → 800 nm 2000 rpm → 400 nm 3600 rpm → 200 nm

Figure 3.3. (a) Step used to measure the thickness of the films obtained by spin coating. (b) Correlation between film thickness and spinning speed from 10 mg/mL PCL solutions, and AFM images of PCL thin films of different thicknesses**.**

Scaffolds

For the production of the porous scaffolds, PCL/Q (10 % of quercetin) solutions were prepared using 2.2.2-trifluoroethanol (TFE) and a mixture of TFE and formic acid (FA), added to increase the conductivity. In the first case, 4.0 g of PCL and 0.444 g of quercetin were mixed in 15 mL of TFE. In the other solution, 4.5 g of PCL and 0.5 g of quercetin were dissolved in 11 mL of TFE and 4 mL of FA. The mixtures were subsequently vortexed to ensure proper mixing. Afterwards, electrospinning was performed at room temperature (21±2ºC) with controlled humidity (~ 40 %) in a Nanospinner Ne-200 (Inovenso) system. The tunable high-voltage power supply was connected to the tip of the needle (positive lead) and attached to the collector (negative lead) with an alligator clip. The needle-to-collector distance was 20 cm and the polymer solutions were ejected using a syringe pump at an adjusted flow rate. Polymer mats were spun directly onto a plate-shaped collector for 1 hour to achieve rectangular samples with a thickness of approximately 125 μm. Steady conditions were achieved at a flow rate of 0.5 mL/h and 17.5 Kv of voltage for the TFE solution, while a flow rate of 1.0 mL/h and 19.9 Kv of voltage were used when formic acid was added.

3.2.3. Field Emission Scanning Electron Microscopy (FE-SEM)

The electrospun mats were examined by means of Field Emission Scanning Electron Microscopy (FE-SEM). The PCL-Quercetin scaffolds were sputter-coated with a thin layer of gold (~ 15 nm) in an Emitech K550X and observed in a Hitachi SEM (Hitachi S-4800N). The voltage used was 10.0 kV and the working distance was 7.0-9.0 mm with a magnification of 1000x, 5000x and 20000x. In order to assess the average diameter, over 100 individual fibers were measured by Image J software using SEM images from at least five different sections of each sample.

3.2.5. Differential Scanning Calorimetry (DSC)

Thermal analyses were conducted on a Modulated DSC Q200 from TA Instruments. All scans were carried out in hermetic aluminum pans under a nitrogen atmosphere for sample weights between 5 and 10 mg. For the purpose of studying glass transition temperatures, two consecutive scans were performed from -80 ºC to 340 ºC with a scan rate of 20 ºC/min, ensuring complete melting of the sample. Firstly, it was performed an isotherm at a temperature of 110 ºC during 30 min to eliminate the water contained in the quercetin. Glass transition temperatures (T_g) were measured in the second scan as midpoint of the specific heat increment.

3.2.6. Attenuated Total Reflection Fourier Transform Infrared Spectroscopy (ATR-FTIR)

ATR-FTIR spectra of the PCL/Q films were recorded on a Nicolet AVATAR 370 Fourier transform infrared spectrophotometer with a PIKE MIRacle ATR accessory containing diamond crystal. Spectra were taken with a resolution of 4 cm^{-1} and were averaged over 32 scans in the 4000-525 cm^{-1} range.

3.2.7. Atomic Force Spectroscopy (AFM)

An AFM instrument Nanowizard I (JPK Instruments, Germany) was operated in air, using contact imaging mode at constant loading forces and rates. Cantilevers were calibrated before each experiment by means of thermal tune method (Hutter and Bechhoefer, 1993). Silicon-nitride probes (DNP-10, Bruker, USA) with a nominal spring constant of 0.12 N/m were used in the experiments. All images were processed by JPK data analysis software.

3.2.8. In Vitro Release Studies and Release Kinetics

Release kinetics of quercetin was examined from different types of platforms: micrometric films obtained by solvent-casting, nanometric films obtained by spin coating, and scaffolds obtained by electrospinning. The release behaviour was studied considering four mathematical models [10, 11, 12]:

4. Zero order: $C_t/C_\infty = k_0 t$ (1)
5. First order: $\ln(1 - C_t/C_\infty) = -k_1 t$ (2)
6. Higuchi: $C_t/C_\infty = k_h t^{1/2}$ (3)
7. Korsmeyer-Peppas: : $C_t/C_\infty = kt^n$ (4)

C_t is the cumulative amount of drug released at time t, C_∞ represents the starting amount of drug, n is the release exponent; and k_0, k_1, k_h and k are constants.

Micrometric Films (UV-Vis)

UV–Vis absorption spectra were recorded over wavelengths ranging from 190 to 500 nm using a Perkin Elmer Lambda 265 UV-Visible spectrophotometer. In advance of the drug release experiments, two standard curves with known concentrations of quercetin were built. On the one hand, quercetin dissolved in tetrahydrofuran with a λ_{max} at 370 nm was used to measure the initial and the final content of quercetin encapsulated in the PCL fibers. On the other hand, a second calibration curve was prepared measuring the absorbance of the quercetin in PBS buffer solution under nitrogen atmosphere at the 375 nm wavelength. Drug release experiments were carried out at concentrations lower than 25 ppm because at higher concentrations the flavonoid was partially insoluble [13].

Then, 1 cm^2 square PCL/Q films 200 μm thick obtained by solvent casting, as well as scaffolds 125 μm thick, were immersed in 100 mL of 0.1 M nitrogen-treated PBS at 37 ºC (pH 7.4). As explained before, with the aim of avoiding the oxidation of the quercetin, the oxygen of the PBS was previously removed through nitrogen recirculation. At fixed time intervals, samples of 2 mL were taken and replaced with fresh nitrogen-treated PBS at 37 ºC. Quercetin concentration in solution was determined by UV spectroscopy at a wavelength of 375 nm (attributed to the B-ring catechol structure), using the corresponding calibration curve.

Nanometric films (QCM-D)

Even though being UV-Vis spectroscopy the general way to monitor the release mechanism, here, quartz crystal microbalance with dissipation monitoring (QCM-D) experiments were performed in a Q-Sense E4 instrument (Q-Sense, Biolin Scientific AB) to measure the quercetin release from the nanometric films due to its high sensitivity, durability and linear response to the amount of mass adsorbed on electrodes [14]. Prior to their use in the experiments, QSX303 Silicon coated quartz sensors (Q-Sense, Biolin Scientific AB) were sonicated in ethanol for 20 min, dried under N_2 stream, and treated with UV/Ozone for 30 min. Then, the sensors were spin coated pouring a single drop of PCL/Q solution of 10 mg/mL before mounted into the QCM-D chamber. Experiments were performed at 37 °C and the volume of nitrogen-treated PBS contained in each chamber was 300 μL. Real time variations of frequency (Δf) and dissipation (ΔD) parameters were observed at several overtones (n = 3, 5, 7,. . .,13) throughout the QCM-D experiment. Each point of ΔD/Δf plot represents a dissipation and frequency data at a certain time, which provides a more detailed view on the viscoelastic evolution of films per mass unit (Δm) change. Hence, we used the Sauerbrey equation ($\Delta m = -k\Delta f$) for correlating changes in the oscillation frequency of a quartz crystal with the mass deposited on it. The analysis of the mass loss during the experiment enables the study of quercetin release kinetics from PCL nanometric films. As the polymer did not degrade during the experiment, the mass loss is only attributable to the release of quercetin.

3.3. Results and discussion

3.3.1. DSC Analysis

Miscible polymer-drug systems show a single glass transition temperature (T_g) intermediate between those of the pure components [15, 16, 17] that usually follow the Fox equation [18]:

$$\frac{1}{T_{gb}} = \frac{w_1}{T_{g1}} + \frac{w_2}{T_{g2}} \tag{6}$$

where w_1 and w_2 are the weight fractions of components 1 and 2 respectively, T_{g1} and T_{g2} are glass transitions of pure components, and T_{gb} is the glass transition of the blend (temperatures in Kelvin).

As can be seen in Figure 3.4, pure PCL is a semicrystalline polymer displaying a glass transition temperature located at about -60 ºC and a melting endotherm at about 65 ºC. In contrast, quercetin is a crystalline flavonoid with a melting endotherm located at about 327 ºC. Figure 3.4a shows first DSC traces obtained for the pure components and for different PCL/Q blends. It was observed that the addition of 20 wt.% of quercetin lowers the melting temperature of PCL by 10 ºC, suggesting miscibility. However, due to the strong autoassociation of the flavonoid, Quercetin is able to crystallize at compositions above 40 wt.%. It can form crystals, as reflected by the two melting endotherms corresponding to the pure components of the blends (see Fig. 3.4a).

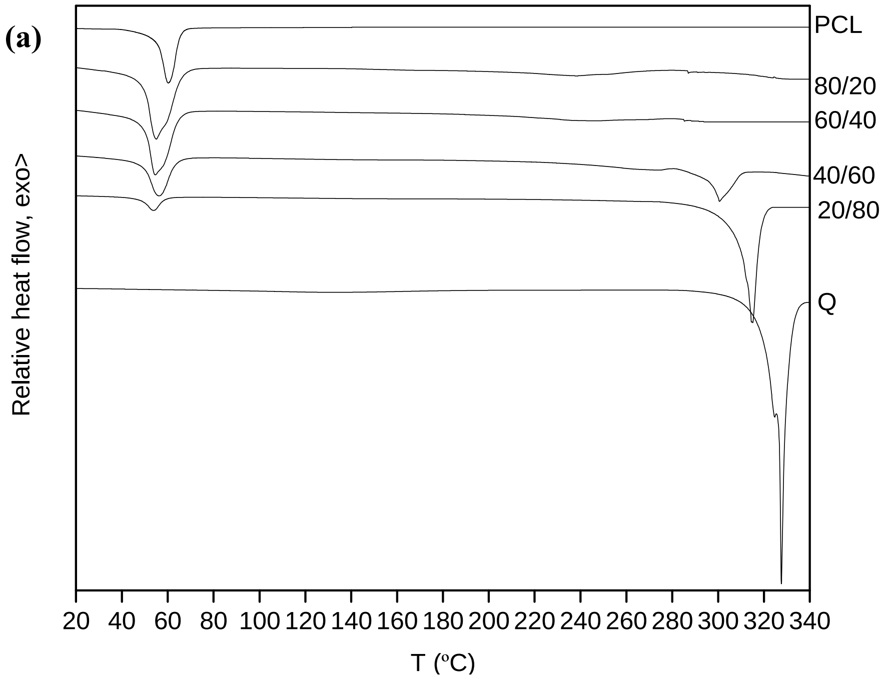

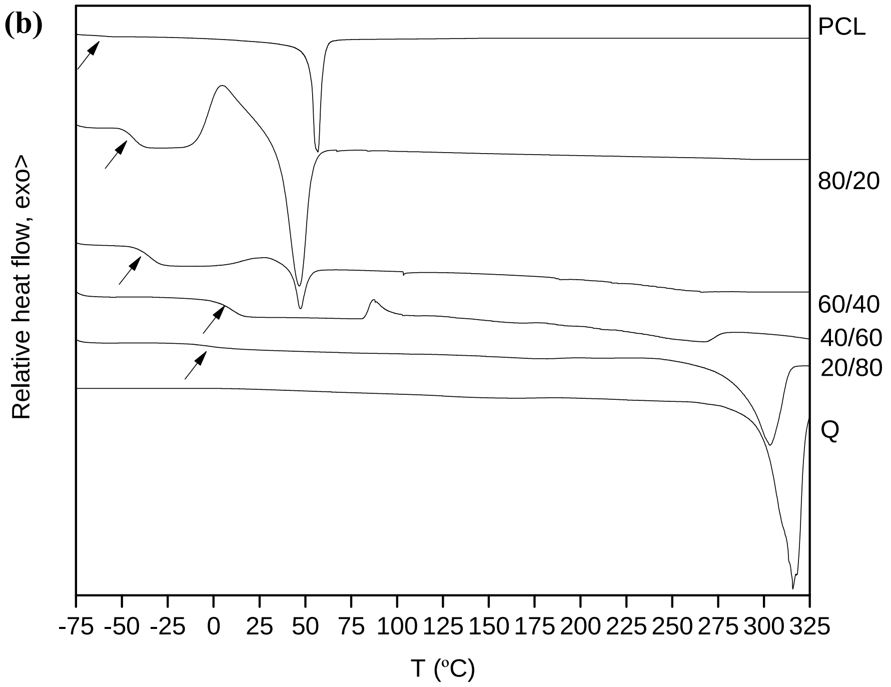

Figure 3.4. (a) First and (b) second scan DSC curves for PCL, Quercetin and PCL/Q blends.

Since Quercetin does not show a glass transition temperature jump, it can be estimated using the empirical Beaman-Boyer rule $T_g/T_m = 2/3$ at about 127 ºC [19]. Consequently, for miscibility to occur, T_g of the blends should shift from the location corresponding to the pure polymer (-60 ºC) to the approximate vitrification temperature of the quercetin (127 ºC) as the content of the flavonoid increases. Traces taken after cooling from the melt (Fig. 3.4b) show how the glass transition temperature shifts. Nonetheless, with the addition of more than 40 wt.% flavonoid, crystalline quercetin is formed and the Tg of the blend stops its continuous increase (see Tab. 3.1).

Table 3.1. Thermal properties of PCL/Q blends in the second scan**.**

PCL/Q	T_g experimental ºC	T_g (calculated, Fox) ºC	T_m PCL ºC	ΔH_mPCL J/g	T_m Q ºC	ΔH_m Q J/g
PCL	-60	-	57.2	66.4	-	-
80/20	-43.8	-38	47.4	41.7	-	-
60/40	-34.9	-10.9	46.7	8.1	-	-
40/60	9.9	23.1	-	-	265.7	16.6
20/80	-0.5	67.4	-	-	303.3	70.3
Q	-	127.3	-	-	315.7	128.4

3.3.3. ATR-FTIR Analysis

Specific interactions present in PCL/Q blends can be investigated by infrared spectroscopy. The chemical structures of the studied species support the possibility of hydrogen bonding between the hydroxyl groups of quercetin and the carbonyl groups of PCL [20]. Prior to performing the spectra of the PCL/Q samples with the ATR-FTIR, they were melted at a temperature of 330 ºC for 5 min, and subsequently allowed to cool to room temperature.

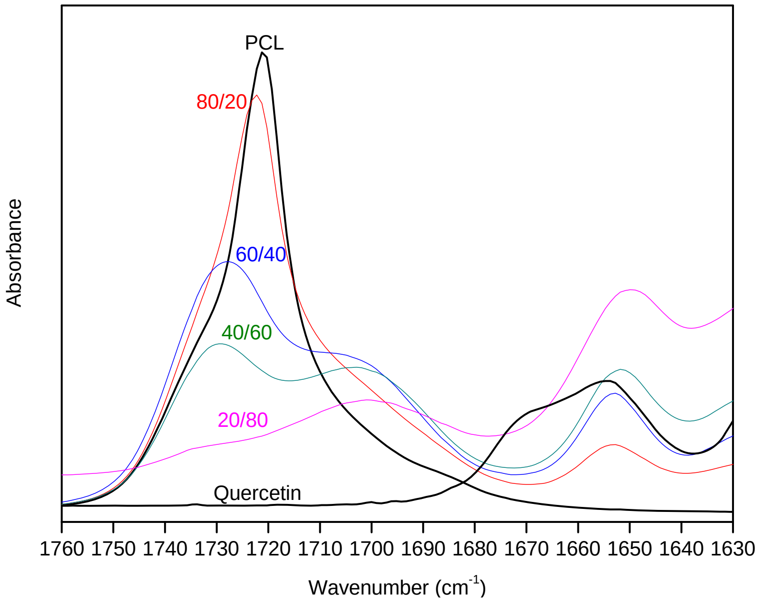

Figure 3.5. Carbonyl stretching region for pure PCL, Quercetin and PCL/Q blends of different compositions.

Fig. 3.5 shows the carbonyl stretching region of PCL, quercetin and PCL/Q blends of different compositions. The spectrum of pure PCL shows a peak at 1721 cm^{-1} representing the crystalline part and a slight shoulder at 1735 cm^{-1} attributable to the amorphous part [21]. Upon blending with quercetin, a new band appears at 1700 cm^{-1} in the intermediate compositions attributable to hydrogen bonded C=O groups in PCL, whereas the band at 1730 cm^{-1} corresponds to amorphous self-associated PCL [22,23]. Pure quercetin has a peak at 1655 cm^{-1} corresponding to the valence vibration band of the carbonyl group in the flavones, influenced by the formation of intramolecular hydrogen bond [24]. That band shifts slightly to 1650 cm^{-1} in the intermediate compositions, indicating that the carbonyl group remains hydrogen bonded in the amorphous phase [25].

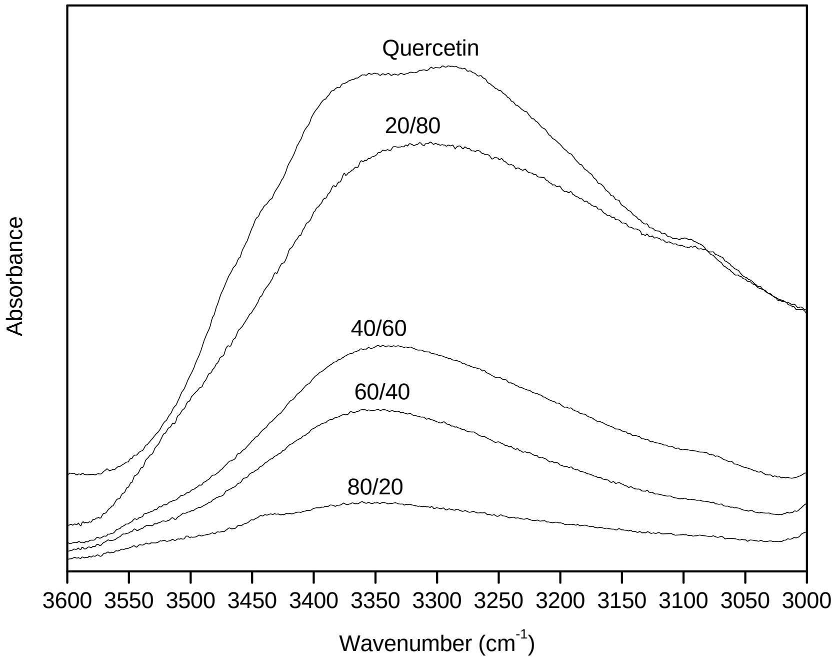

Figure 3.6. Hydroxyl stretching region for pure Quercetin and PCL/Q blends of different compositions.

Figure 3.6 shows the ATR-FTIR spectra of the hydroxyl stretching region for the PCL/Q blends. The spectrum of pure Quercetin shows a complex, broad band with at least two discernable components located at about 3280 and 3350 cm^{-1}. These locations can be attributed to the O-H stretching of hydroxyl groups participating in cooperative hydrogen bonds of different strength. The strength of a cooperative hydrogen bond depends on its hydrogen bonding environment in the hydrogen bonding chains/network formed in the crystalline structure, which is different for the different hydroxyl groups depending on the crystalline structure. Upon addition of PCL, the band at 3280 cm^{-1} loses intensity and only a broad band located at about 3350 cm^{-1} can be observed in the PCL rich blends. Hence, the spectral changes in the OH region confirm the role of the hydrogen bonding interactions, suggesting that the strongest cooperative interactions occurring in pure crystalline Quercetin are replaced by weaker (but still cooperative) hydrogen bonding interactions in the blends. The shift of the OH stretching band to higher wavenumbers is typical when O-H··O-H interactions are replaced by -C=O···H-O- ones [26]. The latter act as terminal groups that disrupt the O-H···O-H···O-H cooperative chains, reducing hence the cooperativity of the hydrogen bonding interactions.

3.3.4. AFM Analysis

The images of PCL/Q blends shown in Figure 3.7 reveal the influence of intermolecular interactions in the chain organizing process of a semicrystalline polymer. In a miscible polymer-drug system, the mobility of polymer chains during the crystal formation is hindered due to the weak physical bonds developed between the two species, originating a decrease in the growt.h rate of crystals. In other words, there is no enough time for the arrangement of the polymeric chains, due to a lower chain mobility [27, 28]. In AFM topographic images of PCL thin films (800 nm), it is observed the characteristic spherulitic morphology of semicrystalline polymers (Figure 3.7a). However, as the flavonoid content in the blend increases, spherulitic boundaries become round and the crystalline phase shows a less compact morphology (Fig. 3.7b and 3.7c).

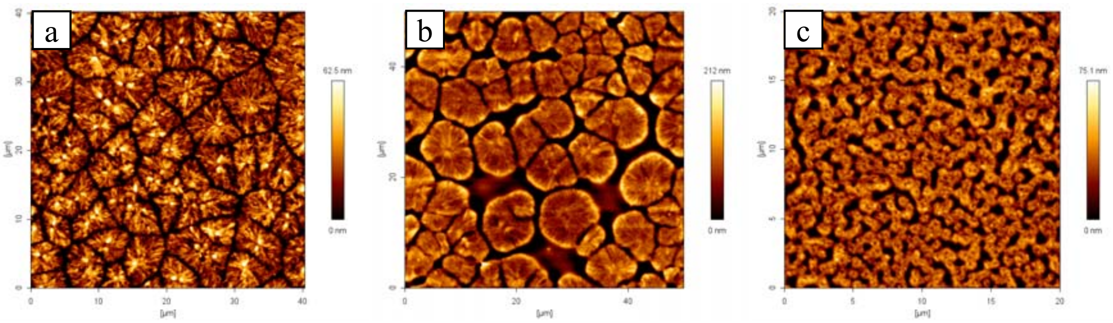

Figure 3.7. AFM topographic images: (a) PCL, (b) PCL/Q 80/20, and (c) PCL/Q 60/40. Films thicknesses were about 800 nm.

3.3.5. Drug Release Behavior

Effect of the Film Thickness on the Quercetin Release

In vitro release experiments were performed for 200 µm and 200 nm thick PCL/Q 80/20 and 60/40 films, since the lack of a melting point in the DSC thermogram (see Fig. 3.4) suggests that the quercetin is in amorphous form, and as a result, ready to release from the PCL. As mentioned in other chapters, the first step of the release is the penetration of the buffered solution into the polymeric matrix, leading to its swelling. As a result, the polymeric network becomes wider, and the amorphous quercetin dissolved in the polymer matrix diffuses throughout it to reach the outer solution [29]. In the case of the micrometric films, the experiment was carried out for 6 h, considering that no more quercetin is released after that time. As can be seen in Figure 3.8a, the 70 wt..% of flavonoid is released from the PCL/Q 80/20 blend after 2.5 hours, whereas only the 20 wt..% from the 60/40 blend at the end of the experiment.

Then, the kinetic studies of nanometric PCL/Q 80/20 and 60/40 samples (200 nm) were investigated by QCM-D measurements, until no changes in the frequency were detected and the whole quercetin was released (30 h). In order to ensure the steadiness in the signal, the experiment was performed during 3 days. Quercetin release profiles from PCL/Q blends are shown in Figure 3.8b. As can be seen, the release behavior is completely different depending on thickness and composition. While in the PCL 80/20 nanometric blend took 25 h to release 70 wt.% Quercetin, in the micrometric counterpart the same percentage was released in only 1.5 h. On the contrary, 35 wt.% Quercetin was released in 2 hours from the nanometric 60/40 blend, while only 20 wt.% was released from the micrometric system after that same time.

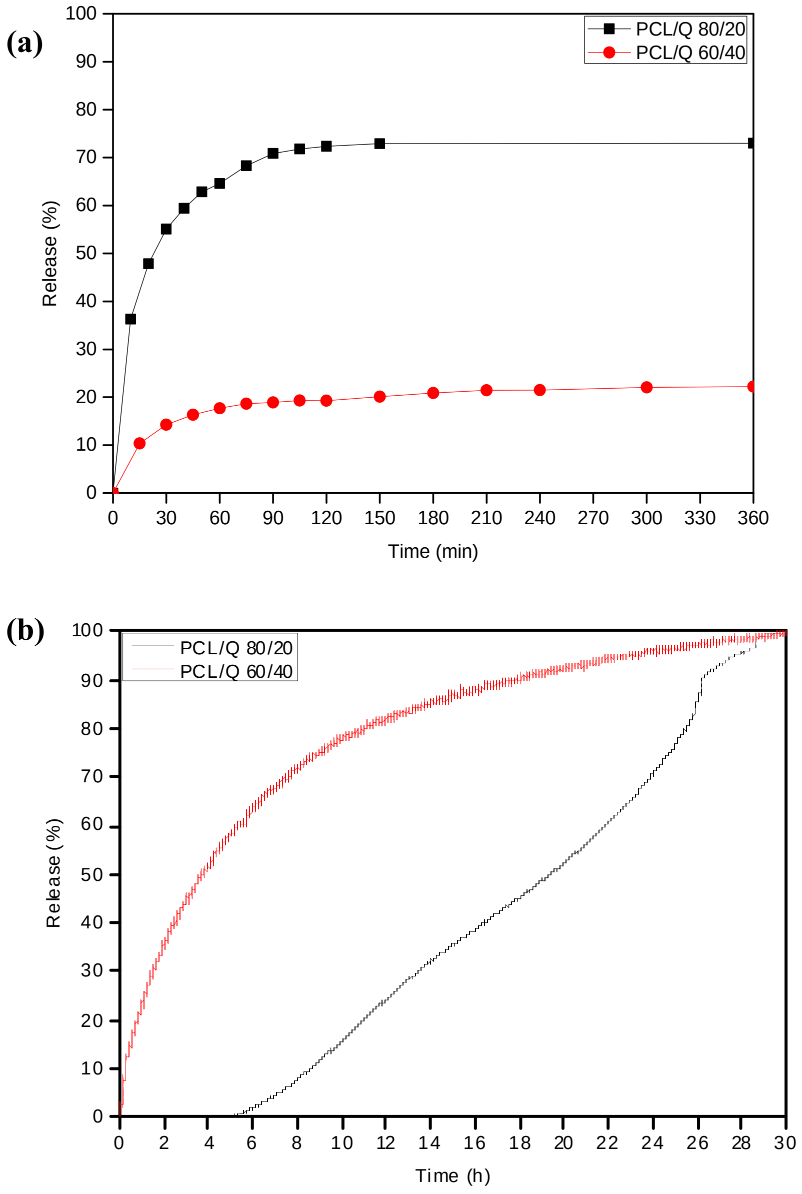

Figure 3.8. (a) Drug release profile of PCL/Q 80/20 and 60/40 samples with a thickness of 200 μm obtained by solvent casting, immersed into 100 mL of nitrogen-treated PBS (pH 7.4) at 37ºC during 6 hours. (b) Drug release profile of PCL/Q 80/20 and 60/40 samples with a volume of PBS of 300 μL at 37 ºC during 30 hours.

Release data obtained from the films at different scales has been fitted to kinetic equations to study the mechanism of flavonoid release, and regression coefficients are shown in Table 3.2.

Table 3.2. Fitting of the release data to the mathematical models for drug release kinetics. R^2 is the correlation coefficient.

Film thickness	**PCL/Q**	**Zero order**	**First order**	**Higuchi**	**Korsmeyer-Peppas**
200 μm	80/20	$R^2 = 0.759$	$R^2 = 0.845$	$R^2 = 0.887$	$R^2 = 0.946$
	60/40	$R^2 = 0.669$	$R^2 = 0.688$	$R^2 = 0.822$	$R^2 = 0.897$
200 nm	80/20	$R^2 = 0.995$	$R^2 = 0.987$	$R^2 = 0.992$	$R^2 = 0.888$
	40/60	$R^2 = 0.888$	$R^2 = 0.991$	$R^2 = 0.979$	$R^2 = 0.970$

In accordance with the results obtained, PCL/Q blends with a thickness of 200 μm follow the Korsmeyer-Peppas kinetic model, and the release is governed by a Fickian diffusion mechanism. In contrast, the release model in nanometric films differs depending on the composition. The release from PCL/Q 80/20 blend fits to zero order kinetics, where it occurs at a constant rate and is controlled the by the relaxation of polymeric chains. Zero order or constant rate release of drug is desirable in order to minimize swings in drug concentration in the blood, allowing a stable effect. Thus, this release mechanism is useful for sustained drug delivery systems. Conversely, PCL/Q 60/40 nanometric system follows a first order kinetic model. Hence, there is an initial burst (the 50 % is released within the first 4 hours), because the drug is in amorphous form since the beginning and then, the quercetin is released in a controlled way. Therefore, it can be a good choice in applications where it is necessary to attain rapidly the effective therapeutic concentration, and then a maintained dose of the desired drug is required.

Effect of the 3D Structure on the Quercetin Release

Apart from building scaffolds for tissue engineering, drug delivery is one of the most promising applications of electrospun fibers due to their large specific surface area, resulting in high loading capacity. Other appealing features for electrospinning in this field include high encapsulation efficiency, the possibility of simultaneous delivery of diverse therapies, ease of operation, as well as cost-effectiveness [30-32]. From the first study made by Kenawi et al. using nanofibers as drug delivery systems [33], different controlled drug release profiles, such as immediate, smooth, pulsatile, delayed, and biphasic releases, have been successfully developed [34, 35].

In this section, the burst release of quercetin was studied in three different PCL platforms with similar thickness (~ 125 µm) having a flavonoid content of ~ 10 % by weight: a film and two mats made by electrospinning. It is well known that the structural properties (surface area to volume ratio and porosity, along with the thickness) of the release platform, affect the release behavior of the drug [36]. Therefore, tunable release profiles can be achieved by altering the 3D physical morphology of the polyester-quercetin composites.

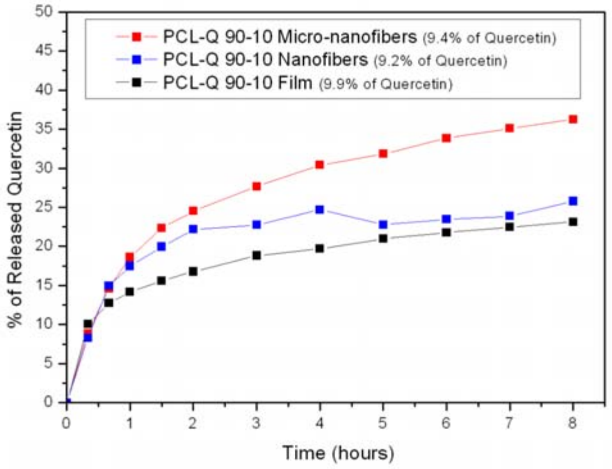

Figure 3.9. Quercetin release profiles of PCL/Q 90/10 samples of different structures with a thickness of 125 µm, immersed into 100 mL of nitrogen treated-PBS at 37 ºC for 8 h.

During the period of study (8 hours) poly(ε-caprolactone) did not degrade [37] and thus, the measured drug can only be attributed to quercetin diffused from both the matrix and the porous structures. As shown in Figure 3.9, different release profiles were obtained depending on the type of platform, concluding that the release rate of quercetin decreased with the size of the pores (Micro-nanofibers mat > Nanofibers mat > Film). This means that bigger pores implies faster release, which could be explained by the greater interactions between the eluting medium and the material. The non-porous film displayed lower water uptake capacity and in the first 2 hours, the release only reached a 16.8% with a final percentage of 23.1 % at the end of the study. The film surface lost its crystalline structure during the time submerged in PBS buffer solution and, thanks to the drug diffusion as well as the erosion caused by the surrounding medium, some micropores started to appear (see Figure 3.10). In contrast, the electrospun scaffolds maintained its fibrous structure throughout the entire experiment. Although both systems had similar porosities (~ 75%), the scale of their pores affected the ability of water to penetrate, as well as the release.

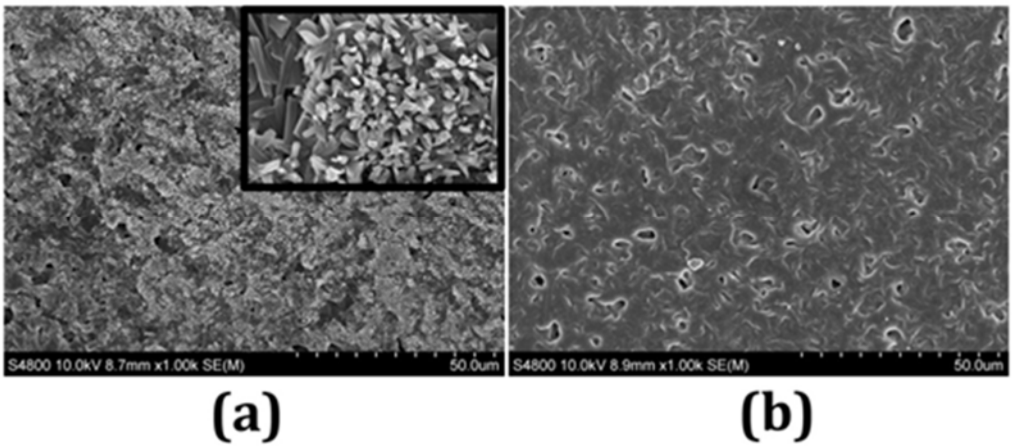
S4800 10.0kV 8.7mm x1.00k SE(M)
50.0um
S4800 10.0kV 8.9mm x1.00k SE(M)
50.0um
(a)
(b)

Figure 3.10. FE-SEM images of PCL/Q 90/10 film (a) before, and (b) after 8 hours of in vitro quercetin release**.**

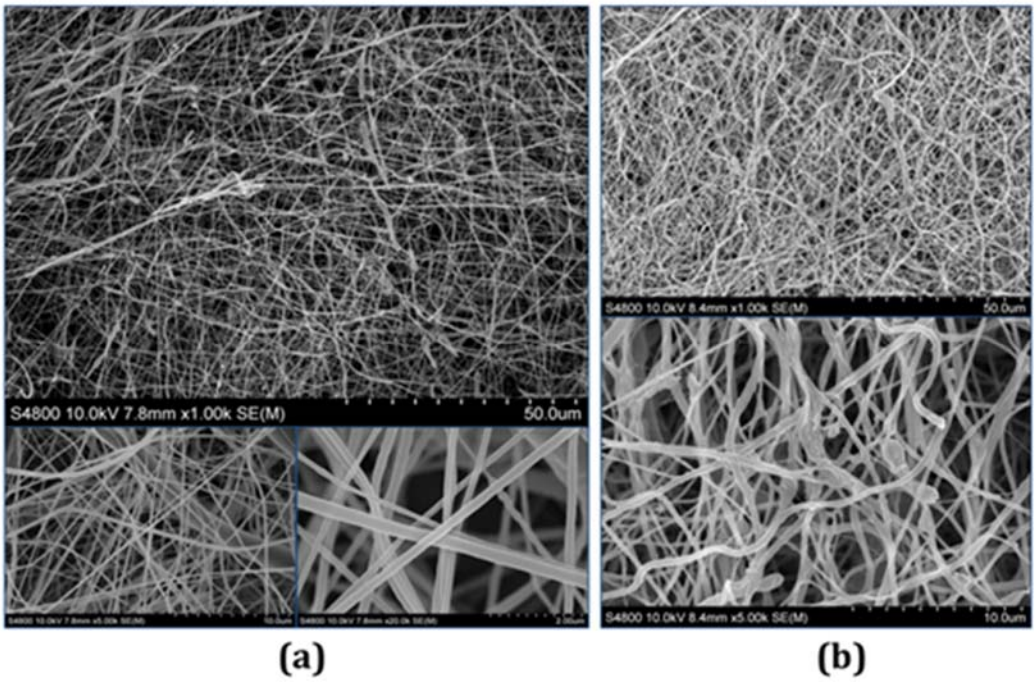
S4800 10.0kV 7.8mm x1.00k SE(M)
50.0um
S4800 10.0kV 8.4mm x1.00k SE(M)
50.0um
S4800 10.0kV 8.4mm x5.00k SE(M)
10.0um
(a)
(b)

Figure 3.11. FE-SEM images of PCL/Q 90/10 nanofibers scaffold (a) before, and (b) after 8 hours of in vitro quercetin release.

The nanofibers mat, fabricated using a TFE-FA solvent mix, presented a fiber average diameter of 193 nm and after 8 hours of release, in which 25.8 % of quercetin was released, showed slight symptoms of deterioration (see Figure 3.11b). After 2 hours of experiment, while the nanofibers mat showed an accumulated quercetin content in the media of 22.2 %, the heterogeneous mico-nano scaffold had already release the 24.5%. The latter structure, as can be seen in Figure 3.12a, exhibited initially three types of fiber morphologies leading to higher pore sizes: nanofibers of around 200 nm of diameter, microfibers of ~ 1 µm diameter and some fibers of large dimensions (4 µm of diameter) which had dilatations of almost 10 µm. These balloon-like fibers might be attributed to encapsulated microparticles that did not dissolve in TFE (formic acid in addition to increase the conductivity reducing the nanofiber diameter, also enhanced the solubility of quercetin). Nevertheless, at the end of the study, these arrangements almost disappeared and only the nanofibers along with some microfibers remained (see Figure 11b). At that moment, a 36.3% of quercetin was released, the maximum peak registered during the entire study.

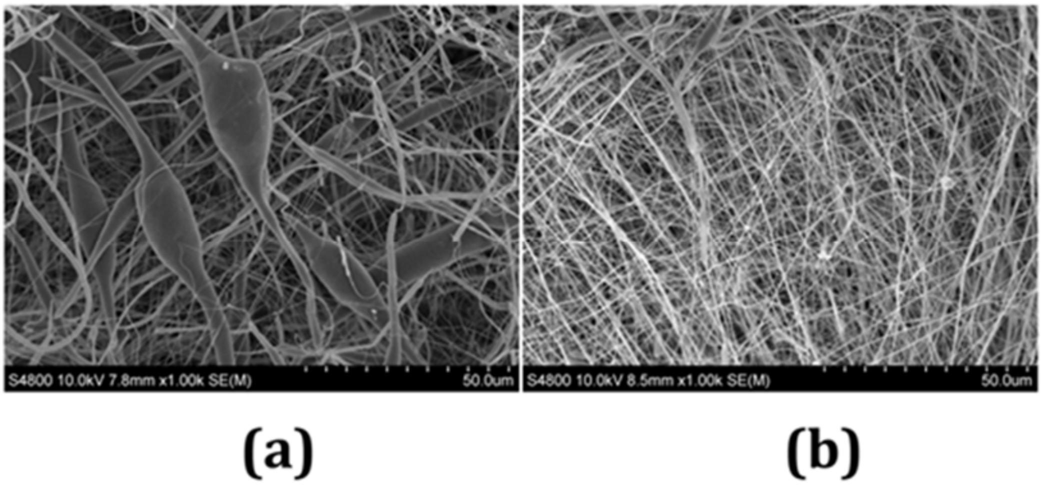
S4800 10.0kV 7.8mm x1.00k SE(M)
50.0um
S4800 10.0kV 8.5mm x1.00k SE(M)
50.0um
(a)
(b)

Figure 3.12. FE-SEM images of PCL/Q 90/10 micro-nanofibers scaffold (a) before, and (b) after 8 hours of in vitro quercetin release.

3.4. Conclusions

Miscibility has been confirmed in the PCL/Q system through a glass transition temperature intermediate between those of the pure components. Nevertheless, when the composition of quercetin in the blend exceeds 40 wt.%, crystallization cannot be suppressed, and the ASD turns to a biphasic system. In the PCL/Q blends, -C=O···H-O- specific interactions were found by means of ATR-FTIR, supported by the analysis of the spherulitic morphology by AFM.

In vitro drug release experiments showed that in PCL/Q 80/20 system quercetin is released by diffusion from micrometric film faster than from its nanometric version. On the contrary, for PCL/Q 60/40 blend, the release is faster from nanometric films. It should be mentioned that the crystallinity of the PCL changes depending on the film thickness: when it is a thin film on a substrate the molecular mobility is restricted, the growt.h of crystals is slower with less nuclei density, and therefore, crystals grow to bigger size (see Figure 3.3b as an illustration of how the crystals are bigger as the film is thinner). The crystallinity of the nanometric PCL/Q 80/20 system is high enough to block the release of the quercetin, delaying the release for 5 hours. Conversely, in nanometric PCL/Q 60/40 sample, the specific interactions between the two species allow the quercetin to be in amorphous form, thus, there is an initial burst where around the 35 % of the drug is release in the first couple of hours.

Through the analysis of drug release mechanism observed for PCL/Q system in the form of film or fiber mat, it was concluded that not only the thickness influences the release, but also the size of the pores. Therefore, there is a greater release in mats composed by micro-nanofibers caused by larger pores when comparing to the release from films with the same composition and thickness. Depending on the application, as well as on the release rate needed, it can be chosen between micro- or nanometric films, or scaffolds.

Over the last few years, scientists have turned to various flavonoids to explain some of the health benefits of a diet rich in fruits and vegetables. However, flavonoids have a very low bioavailability due to its minimum absorption when ingested. That being said, the mixture of quercetin with a biopolymer increases quercetin stability, leading to a sustained activity of the flavonoid. Taking everything into consideration, it is clear that these compounds coming from food deserve further research considering their capabilities of curing diseases.

References

[1] S. Kumar, A.K. Pandey, “Chemistry and Biological Activities of Flavonoids, “An Overview”, *The Scientific World Journal,* 2013.

[2] F. Puoci, C. Morelli, G. Cirillo, M. Curcio, O.I. Parisi, P. Maris, D. Sisci, N. Picci, “Anticancer activity of a quercetin tin-based polymer towards HeLa cancer cells”, *Anticancer Research*, 2012, **32**, 2843-2848.

[3] V. Natarajan, N. Krithica, B. Madhan, P.K. Sehgal, “Formulation and evaluation of quercetin polycaprolactone microspheres for the treatment of rheumatoid arthritis”, *Journal of Pharmaceutical Sciences*, 2011, **100(1)**, 195-205.

[4] B. Hancock, M. Parks, “What is the True Solubility Advantage for Amorphous Pharmaceuticals?”, *Pharm Res*, 2000, **17(4)**, 397-404.

[5] E. Sanchez-Rexach, I. Martínez de Arenaza, J.R. Sarasua, E. Meaurio, “Antimicrobial poly(e-caprolactone)/thymol blends, Phase behavior, interactions and drug release kinetics”, *European Polymer Journal*, 2016, **83**, 288–299.

[6] M. Labet, W. Thielemans,”Synthesis of polycaprolactone, a review”, *Chem. Soc. Rev.*, 2009, **38**, 3484–3504.

[7] N. Shah, H. Sandhu, D.S. Choi, H. Chokshi, A.W. Malick, “Amorphous Solid Dispersions. Theory and Practice”, *Advances in Delivery Science and Technology*, 2014.

[8] M. Bancirova, “Changes of quercetin absorption spectra in dependence on solvent”, *Chemistry Journal*, 2015, **1**, 31-34.

[9] P. Vashisth, R.P. Singh, V.Pruthi, “A controlled release system for quercetin from biodegradable poly(lactide-co-glycolide)-polycaprolactone nanofibers and its in vitro antitumor activity”, *Journal of Bioactive and Compatible Polymers*, 2016, **31**, 260-272.

[10] J.S. Boateng, K.H. Matthews, A.D. Auffret, M.J. Humphrey, H.N. Stevens, G.M. Eccleston, “In vitro drug release studies of polymeric freeze-dried wafers and solvent-

cast films using paracetamol as a model soluble drug", *International Journal of Pharmaceutics*, 2009, **378**, 66-72.

[11] S. Khan, H. Batchelor, P. Hanson, I.Y. Saleem, Y. Perrie, A.R. Mohammed, "Dissolution rate enhancement, in vitro evaluation and investigation of drug release kinetics of chloramphenicol and sulphamethoxazole solid dispersions", *Drug Development and Industrial Pharmacy*, 2013, **39(5)**, 704-715.

[12] T. Higuchi, "Mechanism of sustained-action medication. Theoretical analysis of rate of release of solid drug dispersed in solid matrices", *Journal of Pharmaceutical Sciences*, 1963, **52(12)**, 1145-1149.

[13] A. Seidell, "Solubilities of Organic Compounds", *New York, Publisher, D. Van Norstrand Company*, 1941, **2**.

[14] G. Celik, A.U. Oksuz, "Controlled Release of Ibuprofen from Electrospun Biocompatible Nanofibers with In Situ QCM Measurements", *Journal of Macromolecular Science Part A*, 2015, **52**, 76–83

[15] E. Meaurio, E. Zuza, J.R. Sarasua, "Miscibility and specific interactions in blends of poly(L-lactide) with poly(vinylphenol)", *Macromolecules*, 2005, **38(4)**, 1207-1215.

[16] N. Hernandez-Montero, E. Meaurio, K. Elmiloudi, J.R. Sarasua, "Novel miscible blends of poly(p-dioxanone) with poly(vinyl phenol)", *Eur. Polym. J.*, 2012, **48**, 1455–1465.

[17] A. Lejardi, J.R. Sarasua, A. Etxeberria, E. Meaurio, "Miscible Blends of Poly(ethylene oxide) with Brush Copolymers of Poly(vinyl alcohol)-graft-poly(L-lactide)", *J. Polym. Sci. B*, 2016, **54**, 1217–1226.

[18] T. G. Fox, *Bulletin of the American Physical Society*, 1956, **123**.

[19] R. Nair, N. Nyamweya, S. Gönen, L.J. Martínez-Miranda, S.W. Hoag, "Influence of various drugs on the glass transition temperature of poly(vinylpyrrolidone), a thermodynamic and spectroscopic investigation", *Int. J. Pharm.*, 2001, **225**, 83-96.

[20] S.W. Kuo, C.F. Huang, F.C. Chang, "Study of hydrogen-bonding strength in poly(ε-caprolactone) blends by DSC and FTIR", *Journal of Polymer Science*, 2001, **39**, 1348-1359.

[21] K. Phillipson, J.N. Hay, M.J. Jenkins, "Thermal analysis FTIR spectroscopy of poly(ε-caprolactone), *Thermochimica Acta*, 2014, **595**,74-82.

[22] E.J. Moskala, D.F. Varnell, M.M. Coleman, "Concerning the miscibility of poly(vinyl phenol) blends – FTi.r. study", *Polyme*r, 1985, **26(2)**, 228-234.

[23] J. Wang, M. K. Cheung, Y. Mi, "Miscibility and morphology in crystalline/amorphous blends of poly(caprolactone)/poly(4-vinylphenol) as studied by DSC, FTIR, and 13C solid state NMR", *Polymer*, 2002, **43**,1357-1364.

[24] G. Socrates, "Infrared and Raman Characteristic Group Frequencies, Tables and Charts, 3 ed.", *Chichester, John Wiley and Sons*, 2001.

[25] M. Heneczkowski, M. Kopacz, D. Nowak, A. Kuzniar, "Infrared Spectrum Analysis of Some Flavonoids", *Acta Poloniae Pharmaceutica*, 2001, **58(6)**, 415-420.

[26] D. Li, J. Brisson, "Hydrogen bonds in poly(methyl methacrylate)-poly(4-vinyl phenol) blends", *Polyme*r, 1998, **39**, 793-800.

[27] A. Mamun, C.G. Bazuin, R.E. Prud'homme, "Morphologies of various polycaprolactone/polymer blends in ultrathin film", *Macromolecules*, 2015, **48**, 1412-1417.

[28] C. Hou, T. Yang, X. Sun, Z. Ren, H. Li, S. Yan, "Branched crystalline patterns of poly(e-caprolactone) and poly(4-hydroxystyrene) blends thin films", *J. Phys. Chem. B*, 2016, **120**, 222-230.

[29] J. Siepmann, N.A. Peppas, "Modeling of drug release from delivery systems based on hydroxypropyl methylcellulose (HPMC)" *Adv. Drug Delivery Reviews*, 2001, **48**, 139-157.

[30] X. Hu, S. Liu, G. Zhou, Y. Huang, Z. Xie, X. Jing, "Electrospinning of polymeric nanofibers for drug delivery applications", *Journal of Controlled Release*, 2014, **185**, 12-21.

[31] B. Wang, Y. Wang, T. Yin, Q. Yu, "Applications of electrospinning technique in drug delivery", *Chemical Engineering Communications*, 2010, **197**, 1315–1338.

[32] S. Chakraborty, I.C. Liao, A. Adler, K.W. Leong, "Electrohydrodynamics, a facile technique to fabricate drug delivery systems", *Advanced Drug Delivery Reviews*, 2009, **61**, 1043–1054.

[33] E.R Kenawy, G.L Bowlin, K. Mansfield, J. Layman, D.G. Simpson, E.H. Sanders, G.E. Wnek, "Release of tetracycline hydrochloride from electrospun poly(ethylene-covinylacetate), poly(lactic acid), and a blend", *Journal of Controlled Release*, 2002, **81**, 57–64.

[34] M. Prabaharan, R. Jayakumar, S.V. Nair, "Electrospun nanofibrous scaffolds—current status and prospects in drug delivery", *Advanced Polymer Science*, 2012, **246**, 241–262.

[35] Y.Z. Zhang, C.T. Lim, S. Ramakrishna, Z.M. Huang, "Recent development of polymer nanofibers for biomedical and biotechnological applications", *Journals of Materials Science, Materials in Medicine*, 2005, **16**, 933–946.

[36] A. Laha, S. Yadav, S. Majumdar, C.S. Sharma, "In-vitro release study of hydrophobic drug using electrospun cross-linked gelatin nanofibers", *Biochemical Engineering Journal*, 2016, **105**, 481-488.

[37] J. Fernández, A. Etxeberria, J.R. Sarasua, "In vitro degradation studies and mechanical behavior of poly (ε-caprolactone-co-δ-valerolactone) and poly(e-

caprolactone-co-L-lactide) with random and semi-alternating chain microstructures", *European Polymer Journal*, 2015, **71**, 585-595.

Chapter 4

Antifouling Poly(ε-caprolactone) Surfaces for Medical Devices

Summary

The insertion of a medical device into the organism supports the growt.h of an aggregate of bacteria on its surface termed biofilm, with the ability to resist antimicrobial treatments. Thus, implant-associated infections cannot be treated in an effective way with antibiotics, and in the majority of cases, the only way to get rid of the infection is to remove the implant. This event poses a public health problem, being crucial to find new strategies to face this serious issue. The first stage in the biofilm formation is the adhesion of some biomolecules contained in bacterial cells to the surface of the medical device. Consequently, a good approach is to prevent that adhesion with a coating that avoids bacterial attachment on surfaces, i.e., an antifouling coating. In this work, that coating is based on a fluorinated tripeptide with non-sticky feature whose adsorption is enabled by a DOPA linker. The surface selected is the poly(ε-caprolactone) (PCL), since this biopolymer is suitable for making biodegradable medical devices

4.1. Introduction

Invasive medical devices are widely used for diagnostic and therapeutic purposes in most medical specialties. Infectious risk is one of the most frequent complications related to the use of medical devices such as orthopedic or cardiac prostheses, and vascular or urinary catheters [1]. Bacteria colonize the surface of the foreign material forming a well-defined network called biofilm, which is extremely resistant to antibiotics [2]. Hence, the replacement of the contaminated device is often the only way to treat the infection. It is a proven fact that medical device-related infections are a public health concern and an economic burden.

Biofilm formation is an important strategy of bacteria to survive in adverse environmental conditions. This process consists of different stages: reversible attachment, irreversible attachment, microcolony formation, maturation and dispersion [1]. Therefore, when a medical device is contaminated with bacteria, the microorganisms must adhere to the implant enough time so that the settlement is irreversible to form the biofilm [3]. Once adhered, microorganisms duplicate and develop as microcolonies over the entire surface.

That being said, a promising strategy for avoiding infections on implants is the development of antifouling surfaces that prevent the initial bacterial adhesion [4].

The aim of this work is to combine the versatility of an elastomeric biodegradable material with a new antifouling coating that will reduce the attachment of bacteria on the surface. The main advantage of using biodegradable medical devices is that they do not need to be removed after finishing their service, as they can be absorbed or excreted by the body. In this way, the tissue surrounding can return to its original state, and a follow-up surgery is avoided. Consequently, the combination of a biodegradable polymer with an antifouling coating will be a great advance in materials for making medical devices that prevent infections.

Poly(ε-caprolactone) (PCL) is a semicrystalline polyester widely used in biomedical applications due to its biodegradability, biocompatibility, and good mechanical properties. Its degradation can last from several months to years, making it suitable for long-term biomedical applications [5]. In turn, the antifouling compound under study consists on a low-molecular weight tripeptide, which design allows its spontaneous adsorption onto any kind of substrate, as well as the creation of surfaces with anti-adhesive properties [6]. Due to the insertion of the amino acid 3,4-dihydroxyl-L-phenylalanine (DOPA), a key compound in the formation of mussel adhesive proteins, the peptide has the ability to attach to different surfaces [7]. In addition, the fluorine atom on each of the benzene rings provides the antifouling character to the peptide (see Fig.4.1).

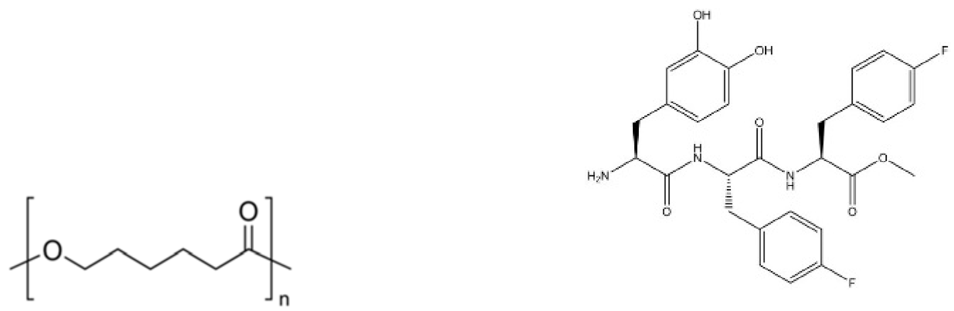

Poly(ε-caprolactone) (PCL)

Antifouling peptide (P)

Figure 4.1. Chemical structures of PCL and Peptide.

Taking everything into consideration, the coating of PCL with a new rationally designed antifouling peptide would lead to the development of innovative antifouling materials for medical applications.

4.2. Results and discussion

4.2.1. Coating of PCL films with antifouling peptide

PCL films with a thickness of 100 μm were obtained by casting from tetrahydrofuran (THF) solutions at room temperature. Then, square samples of PCL (1 cm^2) were dipped into peptide aqueous alkaline solutions at different concentrations (0.1 mg/mL, 0.2 mg/mL, 0.5 mg/mL, 1 mg/mL, 2 mg/mL, and 4 mg/mL) for 2 hours (see Fig.4.2). It should be noted that when the solution reached a pH around 8.5, the initially transparent solution changes to a suspension composed by floating white aggregates. Afterwards, the coated films were rinsed extensively with distilled water and dried into a vacuum oven. Catechol group of the peptide enables its immobilization on PCL surface by a simple dipping process under alkaline conditions [8].

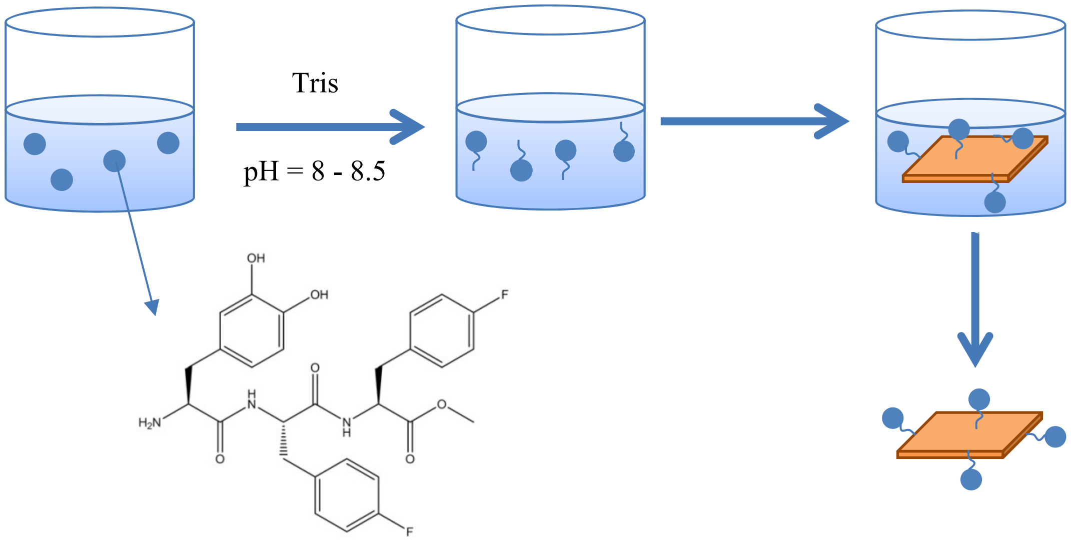

Figure 4.2. Schematic illustration of the dip coating process of PCL films in the peptide solution.

4.2.2. Surface characterization

Transmission Electron Microscopy (TEM) images were recorded to analyze the coverage of the peptide onto the polymeric surface. As it can be seen, the peptide has a tendency to form aggregates rather than a homogeneous coating on the substrate (see Fig. 4.3).

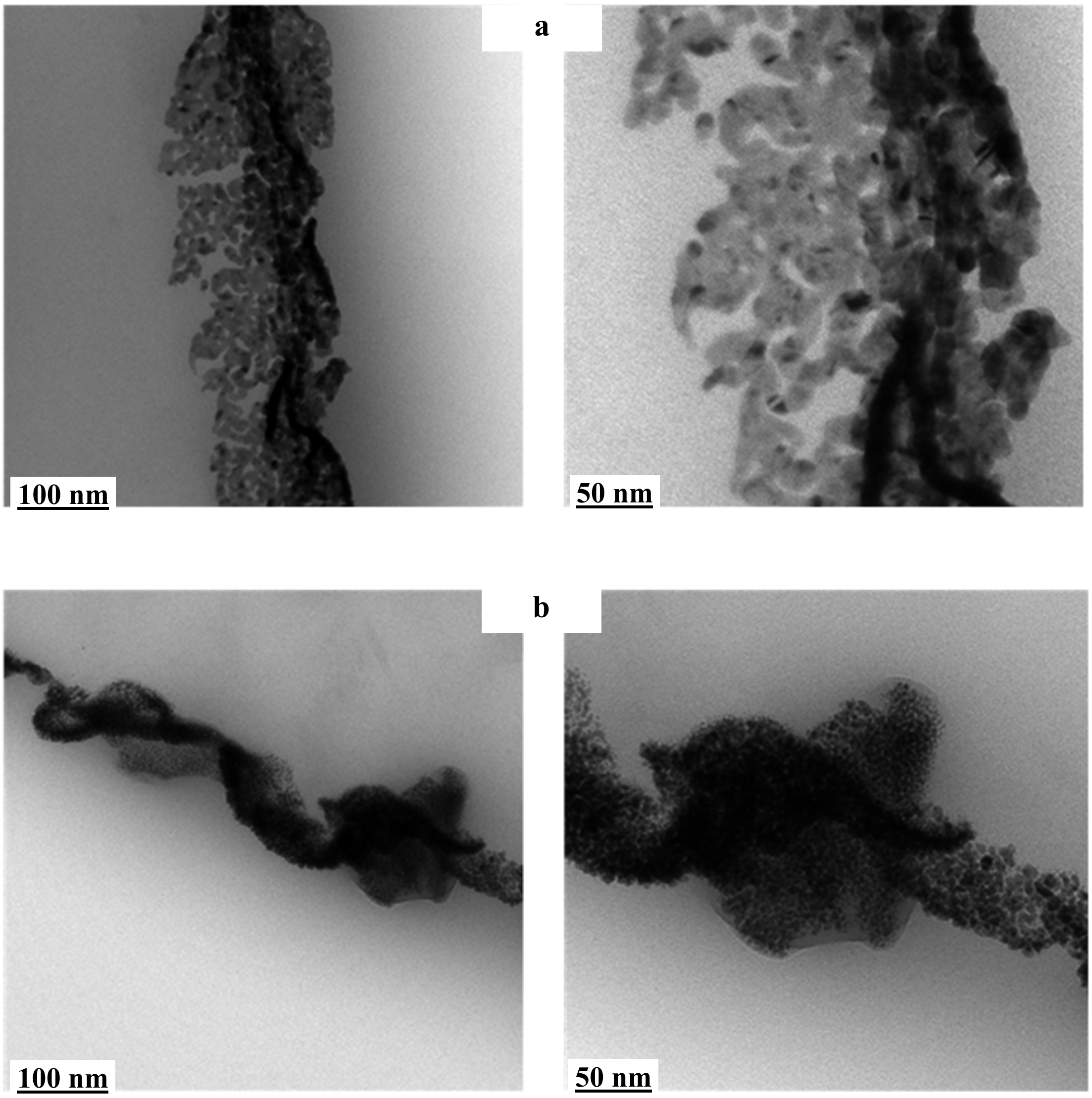

Figure 4.3. TEM images of the peptide on PCL films: (a) PCL coated with a peptide solution of 0.1 mg/mL, and (b) with a peptide concentration of 0.2 mg/mL.

In order to assess the coating, different samples were analyzed using X-ray photoelectron spectroscopy (XPS). This technique revealed the presence of nitrogen and fluorine atoms of the peptide on PCL surfaces (see Fig. 4.4 and Table 4.1).

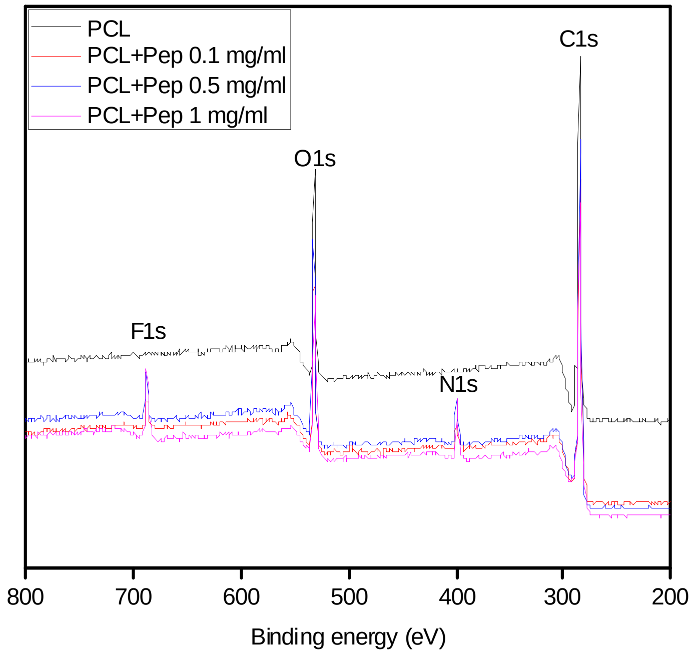

Figure 4.4. XPS spectra of bare PCL (black), PCL coated with a peptide solution of 0.1 mg/mL (red), 0.5 mg/mL (blue), and 1 mg/mL (pink).

Table 4.1. Surface elemental composition of PCL films coated with different concentrations of the peptide determined by XPS, and the nitrogen/fluorine atomic ratio (N/F).

PCL+Pep	**0 mg/mL**	**0.1 mg/mL**	**0.5 mg/mL**	**1 mg/mL**
% C	81.894	77.088	73.843	71.492
% O	14.421	17.547	17.857	16.954
% N	-	2.951	4.101	6.299
% F	-	1.662	2.580	4.228
N/F	**-**	**1.776**	**1.589**	**1.490**

The atomic percentage of N and F became higher as the concentration of peptide increased. Moreover, N/F ratio was very close to the theoretical value according to the structure of the peptide (3N/2F = 1.5).

In addition, samples were analyzed using Attenuated Total Reflectance Fourier Transform Infrared (ATR-FTIR) spectroscopy. For the purpose of studying the peptide deposition on polymeric films, the analysis of the spectra was focused in regions between 3200-3400 cm-1 and 1500-1700 cm-1 where PCL does not show any band [9].

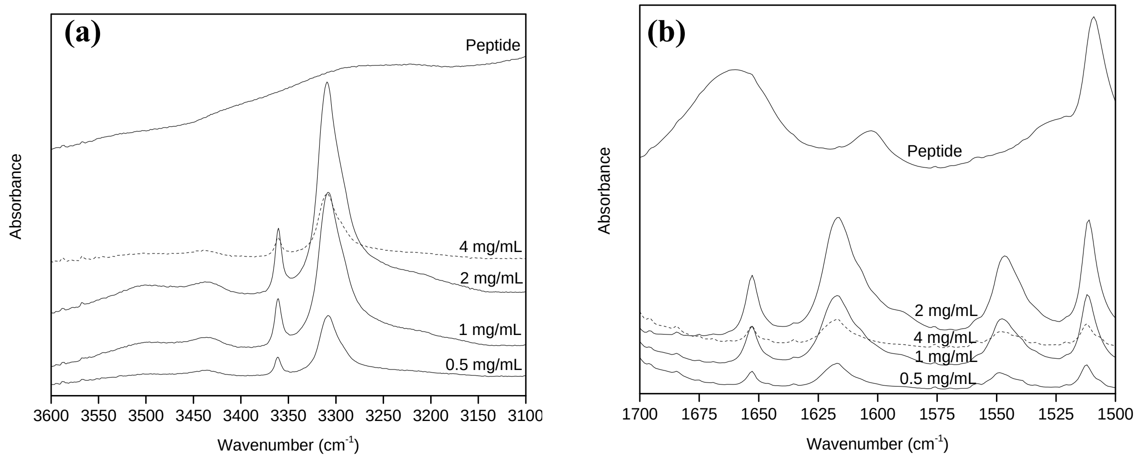

Figure 4.5. ATR-FTIR spectra of bare peptide, PCL coated with a peptide solution of 0.5 mg/mL, 1 mg/mL, 2 mg/mL, and 4 mg/mL. (a) N-H stretching region, and (b) amide I and aromatic rings zone**.**

After coating, new bands appeared at 3361 and 3308 cm^{-1} (see Fig. 4.5a) that can be assigned to the N-H stretching vibrations of the peptide, indicative of the presence of itself on the polymer. In the 1500-1700 cm^{-1} region, the bands at 1653 and 1618 cm^{-1} indicates α-helix and β-sheet structures of the amide I in the peptide, whereas the bands at 1548 and 1512 cm^{-1} represent the aromatic rings (Fig. 4.5b) [10]. After the analysis of the bands obtained in Figure 4, it was concluded that the optimal concentration of peptide solution for PCL coating was 2 mg/mL.

As mentioned above, the bacterial adhesion on a surface is a key factor in biofilm formation. Hence, hydrophobic surfaces can reduce the contact with bacteria, limiting the bacterial attachment which forms the biofilm [11]. A surface is considered hydrophobic with a contact angle greater than 90º, whereas below 90º a surface is hydrophilic. With the aim of studying the hydrophobicity in the samples, contact angle measurements were performed onto surfaces of bare PCL and PCL coated into different peptide solutions (0.5 mg/mL, 1 mg/mL and 2 mg/mL), using a Drop Shape Analyzer. It was concluded that modified substrates exhibited a slight increase in the contact angle, and therefore, a slight increase in hydrophobicity as the peptide concentration increased (see Fig. 4.6). The addition of fluorine atoms contained in the antifouling coating restricted the contact between the surface and water. Thus, the less contact results in a lower chance of bacteria to attach to the polymer [11].

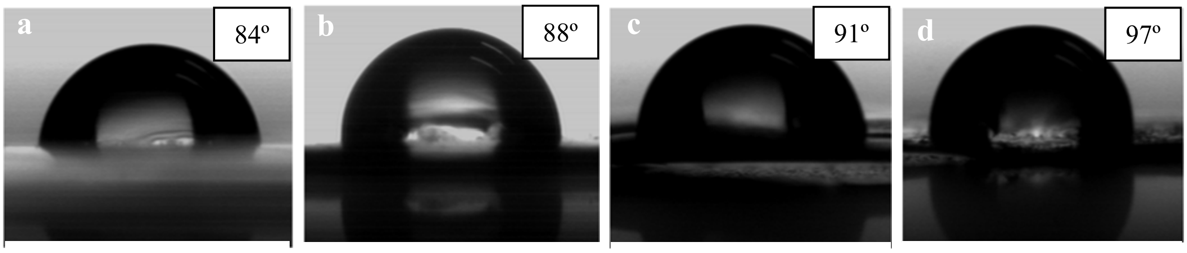

PCL film 0.5 mg/mL peptide solution 1 mg/mL peptide solution 2 mg/mL peptide solution

Figure 4.6. Contact angle measurements of PCL, and superficially modified PCL surfaces after dip coating in different peptide solutions: (a) PCL, (b) PCL coated with a peptide solution of 0.5 mg/mL, (c) 1 mg/mL, and (d) 2 mg/mL.

Finally, in order to study the stability of the coating within a biological media, samples of PCL coated with the peptide at a concentration of 2 mg/mL were immersed into 100 mL of 0.1 M PBS medium (pH 7.4) at 37 ºC for 24 h. ATR-FTIR spectra were compared before and after the experiment. As long as the characteristic bands (1512, 1548, 1618, 1653, 3308 and 3361 cm^{-1}) remained the same after one day under physiological conditions, it was proven that the coating is stable (see Fig. 4.7).

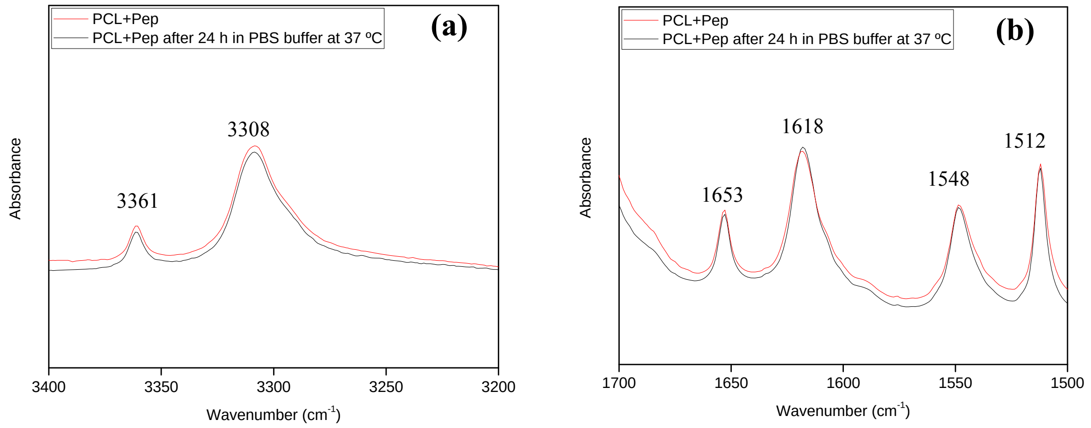

Figure 4.7. ATR-FTIR spectra of PCL film coated with a peptide solution of 2 mg/mL before immersing the film into 100 mL of PBS buffer at 37 ºC (red), and after 24 h into the buffer solution and dried into a vacuum oven (black). (a) N-H stretching region, and (b) amide I and aromatic rings zone.

4.2.3 Biofilm Formation on PCL Surfaces Coated with Antifouling Peptide

Considering 2 mg/mL the optimal peptide concentration for coating PCL surfaces, bare and peptide-coated PCL films (PCL+P) were incubated overnight at 37 ºC in inoculums of *Escherichia coli*, in order to assess the bacterial attachment. Then, bacteria formed during the incubation were removed from the surfaces, diluted and cultured on LB agar plates. After the incubation of the plates, the number of colonies formed was counted (Fig. 4.8). Data were analyzed using the one-way ANOVA method ($p < 0.05$), and it was concluded that the means among samples of PCL and PCL+P are significantly different. That being said, it was observed a reduction of 23 % in the amount of colonies formed on the surface when compared with bare PCL.

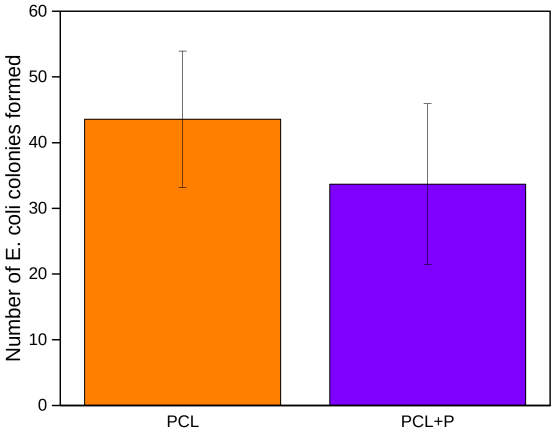

Figure 4.8. Number of *E. coli* colonies grown on bare and peptide-coated PCL surfaces.

4.3. Conclusions

Bacterial adhesion to surfaces and subsequent biofilm formation are a leading cause of chronic infections. In this work, films of PCL were superficially modified with a synthetic tripeptide that interferes with the first step of biofilm formation. The coating occurs spontaneously, since the antifouling peptide contains an amino acid group DOPA that acts as glue. This is a much simpler strategy compared to other surface coupling methods, which require extensive surface modifications and complex reaction steps. In this context, peptide-coated surfaces were characterized by means of TEM, XPS, ATR-FTIR and Contact Angle, and it was found that the coating is not homogenous, that the maximum values of coating were obtained when the PCL films were immersed in 2 mg/mL peptide aqueous alkaline dispersion, as well as that it can be obtained hydrophobic surfaces. Furthermore, it was concluded that the coating remain stable in human body conditions. Eventually, it was determined that the PCL coated with the peptide achieve a reduction of 23 % in the amount of *E. coli* colonies formed. Taking everything into consideration, with this work we would be able to provide an additional advantage to a biomaterial such as the PCL.

References

[1] S.L. Percival, L. Suleman, C. Vuotto, G. Donelli, "Healthcare-associated infections, medical devices and biofilms: risk, tolerance and control", *Journal of Medical Microbiology*, 2015, **64**, 323–334.

[2] E. Sanchez-Rexach, E. Meaurio, J.R. Sarasua, "Recent developments in drug eluting devices with tailored interfacial properties", *Adv. Colloid Interface Sci.*, 2017, **249**, 181-191.

[3] H. Gu, D. Ren, "Materials and surface engineering to control bacterial adhesion and biofilm formation: a review of recent advances", *Front. Chem. Sci. Eng.*, 2014, **8(1)**, 20-33.

[4] S. Nir, M. Reches, "Bio-inspired antifouling approaches: the quest towards non-toxic and non-biocidal materials", *Current Opinion in Biotechnology*, 2016, **39**, 48-55.

[5] M. Labet, W. Thielemans,"Synthesis of polycaprolactone: a review", *Chem. Soc. Rev.*, 2009, **38**, 3484–3504.

[6] S. Maity, S. Nir, T. Zada, M. Reches, "Self-assembly of a tripeptide into a functional coating that resists fouling", *Chem. Commun.*, 2014, **50**, 11154-11157.

[7] E. Ko, K. Yang, J. Shin, S.W. Cho, "Polydopamine-assisted osteoinductive peptide immobilization of polymer scaffolds for enhanced bone regeneration by human adipose-derived stem cells", *Biomacromolecules*, 2013, **14**, 3202-3213.

[8] S. Kumar, M. Perikamana, J. Lee, Y.B. Lee, Y.M. Shin, E.J. Lee, A.G. Mikos, H. Shin, "Materials from mussel-inspired chemistry for cell and tissue engineering applications", *Biomacromolecules*, 2015, **16**, 2541-2555.

[9] K. Phillipson, J.N. Hay, M.J. Jenkins, "Thermal analysis FTIR spectroscopy of poly(ε-caprolactone)", *Thermochimica Acta*, 2014, **595**, 74-82.

[10] G. Socrates, "Infrared and Raman Characteristic Group Frequencies: Tables and Charts", 3 ed., *Chichester: John Wiley & Sons*, 2001.

[11] C.R. Crick, S. Ismail, J. Pratten, I.P. Parkin, "An investigation into bacterial attachment to an elastomeric superhydrophobic surface prepared via aerosol assisted deposition", *Thin Solid Films*, 2011, **519(11)**, 3722-3727.

General Conclusions

In the current PhD thesis an exhaustive study of the phase behavior, miscibility, interactions, drug release kinetics, as well as antibacterial activity of systems composed of poly(ε-caprolactone) with a bioactive molecule has been carried out. These properties of a material must be elucidated in order to design a drug eluting device for a specific application. The main conclusions derived from the research work are highlighted below:

- The miscibility in a polymer-drug system can be established through the analysis of the glass transition temperature. In cases where the analysis is not conclusive (for example when the T_gs of the polymer and the drug are very close), the analysis can be complemented by studying the depression of the melting points of the pure species. In addition, this analysis gives information about the strength of the interactions through the interaction parameter χ, present in the Flory-Huggings theory.

- FTIR spectroscopy is a valuable tool to support the miscibility behavior of the polymer/drug systems and to analyze the specific interactions responsible for miscibility. In the systems investigates in this thesis, hydrogen bonding interactions have been confirmed between the carbonyl groups (-C=O) of PCL and the hydroxyl groups (-OH) present in the different drugs investigated: thymol, chloramphenicol, and quercetin.

- Miscibility affects strongly the spherulitic morphology of PCL. AFM can be used to evaluate the changes in morphology upon blending, which usually result in less compact spherulites in which the amorphous material is pushed to the interspherulitic regions.

- Drug eluting devices provide greater therapeutic efficacy than conventional ones, reducing the side effects associated with excessive dosages. In vitro drug release analyses performed during the study indicate that the bioactive agent is released by diffusion through the swelled polymeric matrix once it is in amorphous form.

Likewise, the results revealed that the release is determined by the composition, as well as by the interactions established in the blends. The release behavior of the systems studied is presented below:

- PCL/THY – THY presents a slow release, since only the 23 % is released in a week, hence, it can be used to build antimicrobial devices for long lasting action.
- PCL/CAM – The release of the antibiotic depends on the composition. When there is less than 10 wt.% of CAM in the blend, it is in amorphous forms and, after an initial burst, the drug is released at a constant rate. Therefore, it can be a good choice in applications where it is necessary to attain rapidly the effective therapeutic concentration and to maintain it for some hours.
- PCL/Q – The release kinetics have been investigated for samples of different thicknesses. Quercetin is released by diffusion from the surface of the films upon PBS penetration, thus, in nanometric films the whole drug is released, since the distance to reach the drug is small. Conversely, part of the quercetin remains inside the polymeric matrix in the micrometric films, due to the inability of PBS to reach the inner flavonoid. When comparing films and scaffolds with the same composition (PCL/Q 90/10), the larger pores of mats composed by micro and nanofibers, enable a faster release, since the surface area to volume ratio is bigger.

- The agar diffusion test against *E. coli* shows that the chloramphenicol can be released in a controlled way without losing antibacterial activity.

- Finally, with the aim of preventing the formation of bacterial colonies on implants, the PCL was successfully coated with a synthetic tripeptide that interferes with the first step of biofouling, due to a DOPA linker.

Appendix

A1. List of Figures

Figure I. Different systems of the body. 32

Figure II. Smart coating of an orthopedic device. 35

Figure III. Use of TNTs for developing drug-releasing implants. 36

Figure IV. Tracheal stents, and airway bypass stent for emphysema treatment. 38

Figure V. Esophageal stent for strictures caused by malignant tumors. 40

Figure VI. Catheterized urinary bladder, ureteral stent to treat the obstruction of a stone, and impregnation of a urinary stent with antimicrobials. 41

Figure VII. Nanoporous anodic alumina coating for drug-release, drug loading of the micro-pits of a microporous surface followed by a top-coating with a biodegradable polymeric layer, and drug eluting balloon. 44

Figure VIII. Controlled release of dexamethasone (an anti-inflammatory drug) from PLGA nanofibers, coated with poly(3,4-ethylenedioxythiophene) (PEDOT) conducting polymer, and local chemotherapeutic agent Gliadel® Wafer. 47

Figure IX. Hydrocolloid wound dressing, and AFAR™ hydrogel wound dressing. 49

Figure X. Implants developed by Microchips Biotech, Inc. 51

Figure 1.1. Schematic illustration of the chemical structures of PCL and Thymol 73

Figure 1.2. First scan DSC curves for PCL, thymol and PCL/THY blends. 79

Figure 1.3. Analysis of the melting temperature of THY for the PCL/THY system. 82

Figure 1.4. Melting endotherms obtained by DSC (5 ºC/min) for the PCL/THY 90/10 system crystallized at different temperatures.. 85

Figure 1.5. Hoffman-Weeks extrapolations for PCL, PCL/THY 95/5, PCL/THY 90/10 and PCL/THY 80/20. 86

Figure 1.6. Analysis of the equilibrium melting temperature of PCL for the PCL/THY system. 88

Figure 1.7. Carbonyl stretching region for pure PCL and PCL/THY blends of different composition. 89

Figure 1.8. Hydroxyl stretching region for pure Thymol and PCL/THY blends of different compositions. 90

Figure 1.9. Dependence of the fraction of free C=O groups with composition. 92

Figure 1.10. Drug release profile for a PCL/THY 70/30 sample (1 cm^2 x 2 mm) obtained by melt mixing and immersed into 100 mL of PBS at 37 ºC during 10 days. 93

Figure 2.1.1. Chemical structure of CAM. 108

Figure 2.1.2. First scan DSC traces for PCL, CAM and PCL/CAM blends. 112

Figure 2.1.3. Conformers proposed by Chatterjee and Acharya, and molecular models showing the hydrogen bonding patterns in the resulting crystalline structures. 115

Figure 2.1.4. Hydroxyl stretching region for pure crystalline CAM, and molten CAM at 160 ºC. 116

Figure 2.1.5. Carbonyl stretching region of CAM and second derivatives ('') of: crystalline CAM at 40 ºC, molten CAM at 160 ºC, supercooled CAM at 40 ºC, CAM in acetonitrile solution (1 wt.%), and computed spectrum of CAM in acetonitrile solution at the B3LYP-D3/def2-TZVP(-f) level of theory. 119

Figure 2.1.6. The seven rotatable bonds in chloramphenicol. 121

Figure 2.1.7. Equilibrium geometries for conformers I (left) and II (right) in acetonitrile at the B3LYP-D3/DZP level of theory. 124

Figure 2.1 8. Relaxed PES scans around ϕ5 (HCCO dihedral) of CAM in vacuum and in acetonitrile solution together with the distances between the two chlorine atoms and the aromatic ring for the structures obtained in vacuum. Computations at the B3LYP-D3/def2-TZVP(-f) level of theory. 127

Figure 2.2.1. A comparison of conventional drug delivery profile vs. a controlled drug release profile. 142

Figure 2.2.2. Chemical structures of PCL and CAM. 143

Figure 2.2.3. DSC traces for PCL, CAM and PCL/CAM blends. First scan, and second scan traces. 148

Figure 2.2.4. Analysis of the melting temperature of CAM in the presence of PCL, and plot used to calculate the interaction parameter for the PCL/CAM system. 152

Figure 2.2.5. Hoffman-Weeks extrapolations for PCL, PCL/CAM 90/10, PCL/CAM 85/15, and PCL/CAM 80/20. 153

Figure 2.2.6. X-H stretching region for the PCL/CAM system at 160 ºC. 155

Figure 2.2.7. Carbonyl stretching region for the PCL and PCL/CAM blends at 160 ºC. Spectra and Norris second derivatives for CAM and for the PCL/CAM 40/60 blend in both molten (160 ºC) and supercooled samples (40 ºC). 156

Figure 2.2.8. XRD patterns of: pure PCL, PCL/CAM 95/5, PCL/CAM 90/10, PCL/CAM 85/15, PCL/CAM 80/20, and pure CAM. 157

Figure 2.2.9. AFM topographic images: pure PCL, PCL/CAM 80/20, PCL/CAM 60/40, PCL/CAM 40/60, PCL/CAM 20/80, and PCL/Erythromycin 50/50 (immiscible)...... 158

Figure 2.2.10. Drug release profile of PCL/CAM 40/60, 80/20 and 95/5 samples of 1 cm^2 with a thickness of 100 μm obtained by solvent casting, immersed into 100 mL of PBS (pH 7.4) at 37 ºC for 7 hours. 159

Figure 2.2.11. Images of inhibition zones created after pouring on LB agar plates with *E. Coli* 5 μl drops of the leachates obtained from PCL after 24 h, chloramphenicol solution of 1 mg/mL, PCL/CAM 80/20 after 30 min, PCL/CAM 50/50 after 30 min, PCL/CAM 80/20 after 3 h, PCL/CAM 50/50 after 3 h, PCL/CAM 80/20 after 24 h, and PCL/CAM 50/50 after 24 h. 162

Figure 3.1. Amorphous solid dispersion (ASD). 173

Figure 3.2. Chemical structures of PCL and Quercetin. 174

Figure 3.3. Step used to measure the thickness of the films obtained by spin coating, and correlation between film thickness and spinning speed from 10 mg/mL PCL solutions, and AFM images of PCL thin films of different thicknesses. 176

Figure 3.4. First and second scan DSC curves for PCL, Quercetin and PCL/Q blends. 182

Figure 3.5. Carbonyl stretching region for pure PCL, Quercetin and PCL/Q blends of different compositions. 183

Figure 3.6. Hydroxyl stretching region for pure Quercetin and PCL/Q blends of different compositions. 184

Figure 3.7. AFM topographic images: PCL, PCL/Q 80/20, and PCL/Q 60/40 186

Figure 3.8. Drug release profile of PCL/Q 80/20 and 60/40 samples with a thickness of 200 μm obtained by solvent casting, immersed into 100 mL of nitrogen-treated PBS (pH 7.4) at 37ºC during 6 hours, and drug release profile of PCL/Q 80/20 and 60/40 samples of 200 nm with a volume of PBS of 300 μL at 37 ºC during 30 hours. 187

Figure 3.9. Quercetin release profiles of PCL/Q 90/10 samples of different structures with a thickness of 125 μm, immersed into 100 mL of nitrogen treated-PBS at 37 ºC for 8 h. 189

Figure 3.10. FE-SEM images of PCL/Q 90/10 film before, and after 8 hours of in vitro quercetin release. 190

Figure 3.11. FE-SEM images of PCL/Q 90/10 nanofibers scaffold before, and after 8 hours of in vitro quercetin release. 191

Figure 3.12. FE-SEM images of PCL/Q 90/10 micro-nanofibers scaffold before, and after 8 hours of in vitro quercetin release. 192

Figure 4.1. Chemical structures of PCL and Peptide........ 204

Figure 4.2. Schematic illustration of the dip coating process of PCL films in the peptide solution. 205

Figure 4.3. TEM images of the peptide on PCL films: PCL coated with a peptide solution of 0.1 mg/mL, and with a peptide concentration of 0.2 mg/mL. 206

Figure 4.4. XPS spectra of bare PCL, PCL coated with a peptide solution of 0.1 mg/mL, 0.5 mg/mL, and 1 mg/mL. 207

Figure 4.5. ATR-FTIR spectra of bare peptide, PCL coated with a peptide solution of 0.5 mg/mL, 1 mg/mL, 2 mg/mL, and 4 mg/mL. N-H stretching region, and amide I and aromatic rings zone........ 208

Figure 4.6. Contact angle measurements of PCL, and superficially modified PCL surfaces after dip coating in different peptide solutions: PCL, PCL coated with a peptide solution of 0.5 mg/mL, 1 mg/mL, and 2 mg/mL. 209

Figure 4.7. ATR-FTIR spectra of PCL film coated with a peptide solution of 2 mg/mL before immersing the film into 100 mL of PBS buffer at 37 ºC, and after 24 h into the buffer solution and dried into a vacuum oven. N-H stretching region, and amide I and aromatic rings zone. 210

Figure 4.8. Number of *E. coli* colonies grown on bare and peptide-coated PCL surfaces. 211

A2. List of Tables

Table I. Polymers used for producing drug eluting devices. 31

Table II. Commercial PMMA bone cements and beads loaded with antibiotics. 33

Table III. Commercial drug eluting devices for breathing system. 39

Table IV. Commercial drug eluting coronary stents. 45

Table V. Commercial drug eluting devices for brain disorders. 48

Table VI. Commercial drug eluting wound dressings. 50

Table 1. Miscibility prediction of the different polymer-drug systems. 68

Table 1.1. Melting temperature of THY in blends with PCL. 81

Table 1.2. Equilibrium melting points (T_{me}) obtained from the H-W extrapolations in Fig. 1.5. 87

Table 1.3. Curve fitting results for the PCL/THY system. 92

Table 1.4. Fitting of the release data to the mathematical models for drug release kinetics. R^2 is the correlation coefficient, n is the release exponent, and k_I and k_{II} indicate the contribution to Fickian and relaxation mechanisms respectively. 94

Table 2.1.1. Dihedrals proposed by Höltje for the two most stable conformers of CAM in solution, and dihedrals corresponding to the crystalline conformers proposed by Chatterjee and Acharya. 121

Table 2.1.2. Dihedral angles and electronic energies for the first six conformers of CAM in acetonitrile solution optimized at the B3LYP-D3/DZP level of theory. 123

Table 2.1.3. Optimized geometries for conformers I and II in vacuum and acetonitrile at the MP2/def2-TZVP(-f) level of theory. Dipole moments and electronic energies have been obtained from single point computations at the MP2/def2-TZVPP level. Free energies and relative populations (N_I/N) also consider the harmonic vibrational analysis at the B3LYP-D3/def2-TZVP(-f) level of theory. 125

Table 2.2.1. Thermal properties of PCL/CAM blends in the second scan. 149

Table 2.2.2. Melting temperature of CAM in CAM-rich PCL/CAM blends. 151

Table 2.2.3. Equilibrium melting temperatures (T_{me}) obtained from the H-W extrapolations. 153

Table 2.2.4. Fitting of the release data to the mathematical models for drug release kinetics. R^2 is the correlation coefficient. 160

Table 2.2.5. Average radius of the inhibition zones measured after fixed intervals, and the amount of drug released at each time. 162

Table 3.1. Thermal properties of PCL/Q blends in the second scan........................... 183

Table 3.2. Fitting of the release data to the mathematical models for drug release kinetics. R^2 is the correlation coefficient... 188

Table 4.1. Surface elemental composition of PCL films coated with different concentrations of the peptide determined by XPS, and the nitrogen/fluorine atomic ratio (N/F). 207

A3. Symbols and Abbreviations

ΔG	free energy
ΔH_m	melting enthalpy
ΔT	supercooling
ΔS	entropy
$\Delta \nu$	frequency shift
ε_0	permittivity in vacuum
ε_r	relative permittivity
ϕ	volume fraction
ρ	density
χ	interaction parameter
μ	dipole moment
A	absorbance
B	interaction energy density
C_α	alpha carbon
C_t	cumulative drug released at time t
C_∞	starting amount of drug
k	Boltzmann constant
l_c	lamellar thickness
m	degree of polymerization

M_n	number average molecular weight
M_w	weight average molecular weight
N_A	Avogadro number
R	universal gas constant
T_c	crystallization temperature
T_g	glass transition temperature
T_m	melting temperature
T_m^0	equilibrium melting temperature
V	volume
wt..%	weight percent
ACN	acetonitrile
AFM	atomic force microscopy
ANOVA	analysis of variance
ASD	amorphous solid dispersion
ATR	attenuated total reflectance
CAM	chloramphenicol
CNF	carbon nanofibers
CNT	carbon nanotubes
DES	drug eluting stent

DNA	deoxyribonucleic acid
DOPA	3,4-dihydroxyl-L-phenylalanine
DSC	differential scanning calorimetry
E.coli	Escherichia coli
EML	list of essential medicines
FA	formic acid
FTIR	Fourier transform infrared spectroscopy
HB	hydrogen bonding
LB	Luria Bertani
NMR	nuclear magnetic resonance
NP	nanoparticles
PBS	phosphate buffered saline
PES	potential energy surfaces
PCL	poly(ε-caprolactone)
PDLLA	poly(D,L-lactide)
PLLA	poly(L-lactide)
QCM-D	quartz crystal microbalance-dissipation
QM	quantum mechanical
SCRF	self-consistent reaction field
SEM	scanning electron microscope

TEM	transmission electron microscopy
TFE	2,2,2-trifluoroethanol
THF	tetrahydrofuran
THY	thymol
TNT	tunneling nanotubes
UV	ultraviolet
WHO	world health organization
XPS	X-ray photoelectron spectroscopy
XRD	X-ray diffraction

A4. List of Publications and Congresses

As a result of this work, a peer-reviewed paper and a review have been published in international indexed scientific journals, and two more papers have been submitted:

- E. Sanchez-Rexach, I. Martínez de Arenaza, J.R. Sarasua, E. Meaurio, "Antimicrobial Poly(ε-caprolactone)/Thymol blends: phase behavior, interactions and drug release kinetics", *European Polymer Journal*, 2016, **83**, 288–299.

- E. Sanchez-Rexach, E. Meaurio, J.R. Sarasua, "Recent developments in drug eluting devices with tailored interfacial properties", *Adv. Colloid Interface Sci.*, 2017, **249**, 181-191.

- E. Sanchez-Rexach, E. Meaurio, J. Iturri, J.L. Toca-Herrera, S. Nir, M. Reches, J.R. Sarasua, "Miscibility, interactions and antimicrobial activity of Poly(ε-caprolactone)/Chloramphenicol blends", *European Polymer Journal*, Submitted.

- E. Meaurio, E. Sanchez-Rexach, A. Butron, J.R. Sarasua, "The Conformation of Chloramphenicol in the ordered and disordered phases", *Journal of Antibiotics*, Submitted.

The results of this research have been also presented in national and international congresses as oral communication or posters. The presenting author of each work is underlined below:

- E. Sanchez-Rexach, I. Martínez de Arenaza, E. Meaurio, J.R. Sarasua, "Interaction and miscibility of biodegradable polymers with biologically active molecules", 27th European Conference on Biomaterials, 2015, Cracow (Poland).

- E. Sanchez-Rexach, I. Martínez de Arenaza, E. Meaurio, J.R. Sarasua, "Biopolimeroak eta molekula biologikoki aktiboak: interakzioak, nahaskortasuna eta askatze zinetikak", Materialen Zientzia eta Teknologia III. Kongresua, 2016, Markina-Xemein (Spain).

- E. Sanchez-Rexach, J. Iturri, J.L. Toca-Herrera, Emilio Meaurio, J.R. Sarasua, "Miscibility in antimicrobial Poly(e-caprolactone) blends: the cases of Chloramphenicol, Erythromycin and Quercetin", 28th European Conference on Biomaterials, 2017, Athens (Greece).

- E. Sanchez-Rexach, E. Meaurio, J.R. Sarasua, "Polímeros biodegradables con moléculas biológicamente activas para la prevención de infecciones en dispositivos biomédicos", CASEIB XXXV, 2017, Bilbao (Spain).

A5. Curriculum Vitae

Full name: Eva Gloria Sánchez Rexach

NIF: 72736389-Q

Date of Birth: 05/08/1980

Gender: F

Contact information: Department of Mining-Metallurgy and Materials Science, School of Engineering, University of the Basque Country, UPV/EHU, Alameda Urquijo s/n, 48010 Bilbao (Spain)

Email: evagloria.sanchez@ehu.eus

Research interests

Biodegradable polymers, characterization techniques, polymer-drug blends, drug release kinetics, antibacterial activity, and drug eluting medical devices.

Graduate Studies

Master in Engineering of Advanced Materials: 2013-2015 (E.T.S.I. Bilbao)

Industrial Organization Engineering: 2003-2007 (E.U.I. Vitoria-Gasteiz)

Industrial Chemistry Engineering: 2000-2003 (E.U.I. Vitoria-Gasteiz)

Languages

Basque: Euskarazko Gaitasun Agiria

English: C1 (Common European Framework of Reference)

German: A2 (Common European Framework of Reference)

Fellowships and Professional Experience

Research fellowship to carry out a PhD thesis in the University of the Basque Country since April 2015

Supply Quality Assurance A-350: 2011-2013 (Aernnova)

Office Worker: 2010-2011 (Basque Government)

Quality Engineer: 2007-2009 (Aernnova Aerostructures)

Organization Technician: 2006 (Michelin)

Publications

- E. Sanchez-Rexach, E. Meaurio, J. Iturri, J.L. Toca-Herrera, S. Nir, M. Reches, J.R. Sarasua, "Miscibility, interactions and antimicrobial activity of Poly(ε-caprolactone)/Chloramphenicol blends", *European Polymer Journal*, Submitted.
- E. Meaurio, E. Sanchez-Rexach, A. Butron, J.R. Sarasua, "The Conformation of Chloramphenicol in the ordered and disordered phases", *Journal of Antibiotics*, Submitted.
- E. Meaurio, E. Sanchez-Rexach, E. Zuza, A. Lejardi, A.P. Sanchez-Camargo, J.R. Sarasua, "Predicting miscibility in polymer blends using the Bagley plot: Blends with poly(ethylene oxide)", *Polymer*, 2017, **113**, 295-309.
- E. Sanchez-Rexach, E. Meaurio, J.R. Sarasua, "Recent developments in drug eluting devices with tailored interfacial properties", *Adv. Colloid Interface Sci.*, 2017, **249**, 181-191.
- E. Sanchez-Rexach, I. Martínez de Arenaza, J.R. Sarasua, E. Meaurio, "Antimicrobial Poly(ε-caprolactone)/Thymol blends: Phase behavior, interactions and drug release kinetics", *European Polymer Journal*, 2016, **83**, 288–299.

Contributions to congresses

- E. Sanchez-Rexach, E. Meaurio, J.R. Sarasua, "Polímeros biodegradables con moléculas biológicamente activas para la prevención de infecciones en dispositivos biomédicos", XXXV Congreso Anual de la Sociedad Española de Ingeniería Biomédica, Bilbao (Spain), ISBN: 978-84-9082-797-0,139-142.
- E. Sanchez-Rexach, J. Iturri, J.L. Toca-Herrera, E. Meaurio, J.R. Sarasua, "Miscibility in antimicrobial Poly(ε-caprolactone) blends: the cases of Chloramphenicol, Erythromycin and Quercetin", 28th European Conference on Biomaterials, 2017, Athens (Greece), 603.
- E. Sanchez-Rexach, I. Martínez de Arenaza, E. Meaurio, J.R. Sarasua, "Biopolimeroak eta molekula biologikoki aktiboak: interakzioak, nahaskortasuna eta askatze zinetikak", Materialen Zientzia eta Teknologia III. Kongresua, 2016, Markina-Xemein (Spain).
- E. Sanchez-Rexach, I. Martínez de Arenaza, E. Meaurio, J.R. Sarasua, "Interaction and miscibility of biodegradable polymers with biologically active molecules", 27th European Conference on Biomaterials, 2015, Cracow (Poland), 346.

Stays in I+D international centers

- The Hebrew University of Jerusalem, Institute of Chemistry, Jerusalem (Israel): May-June 2017.
- University of Natural Resources and Life Sciences (BOKU), Department of Nanobiotechnology, Vienna (Austria): September-December 2016.